**Paulo David Rodrigues Santos**

# Passivação com hidrogénio de centros de recombinação em silício: cálculos usando a teoria do funcional da densidade.

# Hydrogen passivation of recombination centers in silicon: density functional theory calculations.

**Universidade de Aveiro** Departamento de Física
**2019**

**Paulo David Rodrigues Santos**

# Passivação com hidrogénio de centros de recombinação em silício: cálculos usando a teoria do funcional da densidade.

# Hydrogen passivation of recombination centers in silicon: density functional theory calculations.

Dissertação apresentada à Universidade de Aveiro para cumprimento dos requisitos necessários à obtenção do grau de Doutor em Engenharia Física, realizada sob a orientação científica do Doutor José Pedro de Abreu Coutinho, Investigador Principal do Departamento de Física da Universidade de Aveiro.

Apoio financeiro da FCT e do FSE no âmbito do III Quadro Comunitário de Apoio.

Aos meus pais

**o júri / the jury**

presidente / president

Professora Doutora Maria Herminia Deulonder Correia Amado Laurel
Professora Catedrática do Departamento de Línguas e Culturas da Universidade de Aveiro

vogais / examiners committee

Doutor João Manuel de Almeida Serra
Professor Catedrático da Faculdade de Ciências da Universidade de Lisboa

Doutor José Luis Júlio Martins
Professor Catedrático do Instituto Superior Técnico da Universidade de Lisboa

Professor Doutor Vitor José Babau Torres
Professor Catedrático do Departamento de Física da Universidade de Aveiro

Doutor Ricardo Pedro Lopes Martins de Mendes Ribeiro
Professor Auxiliar com Agregação do Departamento de Física da Universidade do Minho

Professor Doutor Manuel António dos Santos Barroso
Professor Auxiliar do Departamento de Física da Universidade de Aveiro

Doutor José Pedro de Abreu Coutinho
Equiparado a Investigador Principal, Departamento de Física da Universidade de Aveiro

**agradecimentos** /
**acknowledgements**

First of all, I would like to thank my parents, to whom I dedicate this thesis, for the support they have provided me. Secondly, I would like to express my sincere gratitude to my advisor Dr. José Coutinho for his constant availability, patience, helpful advice and knowledge sharing. I also thank our colleagues from the Photon Science Institute at the University of Manchester for the collaborative work and experimental input that was vital to the writing of this thesis. A special thanks is due to Dr. Apostolos Marinopoulos for the help provided and for his contribution to some of the results presented here. Last, but not the least, I would like to show my appreciation to all my colleagues and friends at University of Aveiro, particularly Alexandre Carvalho, Daniel Gouveia and Sara Silva for all the fun moments throughout the years.

**Palavras Chave** Silício, Passivação, Metais de Transição, Hidrogénio

**Resumo**

A evolução do mercado de células solares tem motivado avanços significativos na busca de materiais mais baratos e eficientes. O silício cristalino é um dos materiais mais dominantes para aplicações fotovoltaicas (PV), com uma das melhores relações custo-eficiência disponíveis. No entanto, há espaço para melhorias com a eliminação ou passivação de muitos defeitos capazes de capturar portadores de carga positivos e negativos (lacunas e eletrões), seguindo-se a sua recombinação. Impurezas como os metais de transição são alguns dos centros de recombinação mais eficazes que contribuem drasticamente para a perda da eficiência das células solares. Enquanto alguns deles podem ser levados a formar precipitados nos limites de grão dos cristais, abrindo assim alguns caminhos "livres de impurezas", outros, devido à sua baixa difusividade, permanecem isolados ou na forma de pequenos agregados. A passivação com hidrogénio é considerada uma solução importante para mitigar a atividade elétrica associada a esses defeitos. O objetivo principal desta tese é o estudo da interação do hidrogénio com múltiplos defeitos que têm a sua origem tanto em impurezas de metais de transição como em outras impurezas comuns em silício para aplicações fotovoltaicas através de cálculos de primeiros princípios baseados na teoria do funcional da densidade. Estes cálculos foram realizados com a aplicação da aproximação do gradiente generalizado (GGA) para os potenciais de correlação e troca utilizando super-células de silício de 216 ou 512 átomos. Os assuntos aqui abordados podem-se dividir em três partes: O cálculo da estrutura electrónica de impurezas de metais de transição isoladas em silício (capítulo 3), a interação entre o hidrogénio e essas impurezas (capítulos 4 e 5) e a interação entre hidrogénio e defeitos que têm a sua origem em impurezas comuns tais como o carbono e o oxigénio. Os resultados principais obtidos nesta tese podem ser resumidos do seguinte modo: De acordo com os modelos existentes e os resultados experimentais disponíveis, metais de transição dos grupos IV, V e VI são estáveis em posições intersticiais com simetria tetraédrica, produzindo atividade electrónica significativa, com múltiplos níveis dadores profundos e, em alguns casos, níveis aceitadores; a eficácia da passivação por hidrogénio da atividade electrónica produzida por impurezas de metais de transição é limitada pelo tipo de dopagem do material: enquanto que em silício tipo n a formação de complexos de metal-hidrogénio é possível, no caso de silício tipo p isto não se observa devido à repulsão eletrostática a longa distância entre o hidrogénio e as impurezas metálicas, uma vez que, para este tipo de dopagem, em equilíbrio termodinâmico, ambos se encontram no estado de carga positivo. Estes complexos de metal-hidrogénio apresentam significativamente menos atividade electrónica do que metais isolados, e, em alguns casos, existe uma passivação completa do defeito; a interação entre o hidrogénio e impurezas tipicamente inertes como o carbono e oxigénio resulta na formação de um defeito com múltiplas configurações estáveis e que é capaz de funcionar como um centro de captura tanto para eletrões como lacunas, resultando na sua recombinação.

**Keywords** Silicon, Passivation, Transition Metals, Hydrogen

**Abstract**

The evolution of the solar cell market has motivated significant advances in the search of cheaper and more efficient materials. Crystalline silicon is one of the most dominant materials for photovoltaic (PV) applications, with one of the best cost-efficiency relations available. However, there is room for improvement with the elimination or passivation of many defects that can trap positive and negative charge carriers (holes and electrons) followed by their recombination. Transition metal (TM) impurities are among the most dangerous recombination centers contributing severely to the loss of the efficiency of the solar cells. While some of them can be driven to form large precipitates in the grain boundaries of the crystals, opening some "impurity-free"paths, others, due to their low diffusivity, will stay isolated or in the form of small aggregates. Hydrogen passivation is considered to be an important solution for the mitigation of the electrical activity associated to these defects. The main goal of this thesis is to study the interaction between hydrogen and several defects originating either from transition metals or other common impurities in solar silicon by means of first-principles calculations based on the density functional theory. These calculations were done with the application of the generalized gradient approximation (GGA) for the exchange and correlation potentials, employing 216 and 512-Si supercells. The issues addressed here can be divided in three parts: the calculation of the electronic structure of isolated transition metal impurities in silicon (chapter 3), the interaction between hydrogen and these metallic impurities (chapters 4 and 5), and the interaction between hydrogen and defects originating from common impurities such as Carbon and Oxygen (chapter 6). The main results of this thesis can be summarized as follows: (i) in agreement with previous models and with the available experimental data, slow-diffusing transition metals from groups IV, V and VI are stable at the tetrahedral interstitial sites, producing significant electronic activity, with multiple deep donor levels, and, in some cases, acceptor levels; (ii) the effectiveness of hydrogen passivation of the electronic activity arising from transition metal impurities is limited by the doping type of the material: while in n-type silicon the formation of metallic-hydrogen complexes is likely, in p-type this is not possible to observe due the long range electrostatic repulsion between positively charged hydrogen and metallic impurities; (iii) these metallic-hydrogen complexes display appreciably less electronic activity than the isolated metallic impurities and, in some cases, full passivation is achieved; (iv) the interaction between hydrogen and typically inert impurities such as carbon and oxygen leads to the formation of a defect with multiple stable configurations that can work both as an electron or a hole trap, leading to the recombination.

# Contents

# List of Publications

**Previous work:**


1. L. I. Murin, E. A. Tolkacheva, V. P. Markevich, A. R. Peaker, B. Hamilton, E. Monakhov, B. G. Svensson, J. L. Lindström, P. Santos, J. Coutinho, and A. Carvalho, *The oxygen dimer in Si: Its relationship to the light-induced degradation of Si solar cells?,* Applied Physics Letters, **98,** 182101 (2011); doi: 10.1063/1.3584138.

2. A. Carvalho, P. Santos, J. Coutinho, R. Jones, M. J. Rayson, and P. R. Briddon, *Light induced degradation in B doped Cz-Si solar cells,* Physica Status Solidi A **209**, 1894–1897 (2012); doi: 10.1002/pssa.201200196

3. P. Santos, J. Coutinho, M. J. Rayson, and P. R. Briddon, Electrical activity of multivacancy defects in silicon, Physica Status Solidi C, 2000–2004 (2012); doi: 10.1002/pssc.201200063


**During thesis period:**


4. P. Santos, J. Coutinho, V. J. B. Torres, M. J. Rayson, and P. R. Briddon, *Hydrogen passivation of titanium impurities in silicon: Effect of doping conditions*, Applied Physics Letters **105**, 032108 (2014); doi: 10.1063/1.4891575

5. A. G. Marinopoulos, P. Santos, and J. Coutinho, *DFT+U study of electrical levels and migration barriers of early 3d and 4d transition metals in silicon*, Physical Review B **92**, 075124 (2015); doi: 10.1103/PhysRevB.92.075124

6. A. G. Marinopoulos, P. Santos, and J. Coutinho, *Electrical Levels and Diffusion Barriers of Early 3d and 4d Transition Metals in Silicon*, Solid State Phenomena, Vol. 242, pp. 264-270, (2016); doi: 10.4028/www.scientific.net/SSP.242.264

7. M. Vaqueiro-Contreras, V. P. Markevich, M. P. Halsall, A. R. Peaker, P. Santos, J. Coutinho, S. Öberg, L. I. Murin, R. Falster, J. Binns, E. V. Monakhov, and B. G. Svensson, *Powerful recombination centers resulting from reactions of hydrogen with carbon–oxygen defects in n-type Czochralski-grown silicon.* Physica Status Solidi RRL, **11**: 1700133 (2017); doi: 10.1002/pssr.201700133

8. P. Santos, J. Coutinho, S. Öberg, M. Vaqueiro-Contreras, V. P. Markevich, M. P. Halsall, and A. R. Peaker, *Theory of a carbon-oxygen-hydrogen recombination center in n-type Si,* Physica Status Solidi A, **214**, No. 7, 1700309 (2017); doi: 10.1002/pssa.201700309

9. J. Mullins, S. Leonard, V. P. Markevich. I. D. Hawkins, P. Santos, J. Coutinho, A. G. Marinopoulos, J. D. Murphy, M. P. Halsall, and A. R. Peaker, *Recombination via transition metals in solar silicon: The significance of hydrogen–metal reactions and lattice sites of metal atoms.* Physica Status Solidi A, **214**: 1700304 (2017); doi: 10.1002/pssa.201700304

# Chapter 1

# Introduction

## 1.1 Technological relevance

The establishment of policies supporting renewable energies in many developed countries has had a significant influence in the increasing demand of solar cell technology. In 2017 the worldwide growth in capacity of photovoltaic (PV) installations was larger than any other power generating technology, amounting to a total of more than 400 GW [1]. This demand has also been supported by the improving cost-competitiveness of solar technologies, particularly in the case of silicon (Si)-based solar cell devices. Crystalline and multi-crystalline silicon based solar cells are considered to be the most cost-effective devices among the available PV modules, with a cost reduction rate of about 28.5% for each doubling of the number of silicon PV module installations, leading to an ex-factory gate price below $0.35 USD per watt in mid-2017 [2] (see Fig. 1.1.1). As a consequence of that, silicon wafer based solar cells represent over 95% of the PV market share [3]. This cost reduction has been caused by factors such as: the innovation in cell design, the progress in power management electronics and the use of lower cost materials and production processes [4]. The decrease of material prices has been mostly due to the successive replacement of high-purity single-crystal Czochraslki-grown (Cz-grown) silicon ingots with less pure silicon multi-crystalline blocks produced by the carbothermic reduction of silicates in electric arc furnaces, and typically referred as "upgraded metallurgical silicon" (UGM-Si). The purity level of this material varies from 98.5% to 99.5% [5] and can be upgraded through refining processes to acceptable "solar-grade" levels (above 99.999%) [6]. In terms of energy conversion, this material is significantly less efficient than Cz-grown Si, yet the reduction in the production costs largely compensates this loss [4]. In terms of laboratory efficiency, UGM-Si based solar cells have been improving steadily. In the beginning of this decade, efficiencies such as 17.6% [7] or 15.5% [8] were reported. Last year, a value of 21.1% was achieved [9]. The benchmark values in silicon solar cell technology by November 2017 [10] are $22.3 \pm 0.4\%$ [11] for multi-crystalline Si and $26.7 \pm 0.5\%$ [12] for single-crystal material, which is considerably close to the Shockley-Queisser limit for Si at $\sim 30\,\%$ [13]. These values are a good indicator for the margin of improvement that UGM-Si based cells can have, should the issues behind the formation of charge carrier recombination centers be addressed and solved. These issues are mostly related to surface defects, bulk defects and contaminant related point-defects, all inherent to low-cost/purity production processes. Contaminant related defects are the main focus of the work presented in this thesis, specially in the case of transition metal impurities. Note that these impurities are not only relevant in UGM-Si but also in relatively higher purity materials such as Cz-grown Si.

A standard procedure applied for the performance improvement of solar grade and UGM-Si cells is the so called *gettering* of some types of impurities, forcing them to form precipitates near the grain boundary regions through chemical and/or thermal treatment. This treatment can be complemented with hydrogen (H) passivation, usually provided by a hydrogen-rich silicon nitride layer that is deposited on the $n+$ emitter of the cell, also working as an anti-reflection layer [14, 15]. On annealing, the hydrogen present in SiN is set free, becoming able to diffuse into Si and eventually passivate the electrical activity that has origin on a wide range of defects [16, 17]. Some of the most relevant defects in UGM-Si are related to transition metal (TM) impurities [4]. These metallic impurities present considerable electrical activity, working as recombination centers for charge carriers, which can be extremely harmful to the cell efficiency as can be seen in the data resulting from experiments of the Westinghouse group [18, 19] displayed in Figure 1.1.2. When isolated in the crystalline lattice, some of these TM impurities, such as gold (Au), can trap several hydrogen atoms and form passivated complexes [20, 21]. However, the Au-H bonds are not strong enough to survive sucessive thermal treatments, breaking at temperatures over 200 °C [21]. In the case of iron (Fe), a very

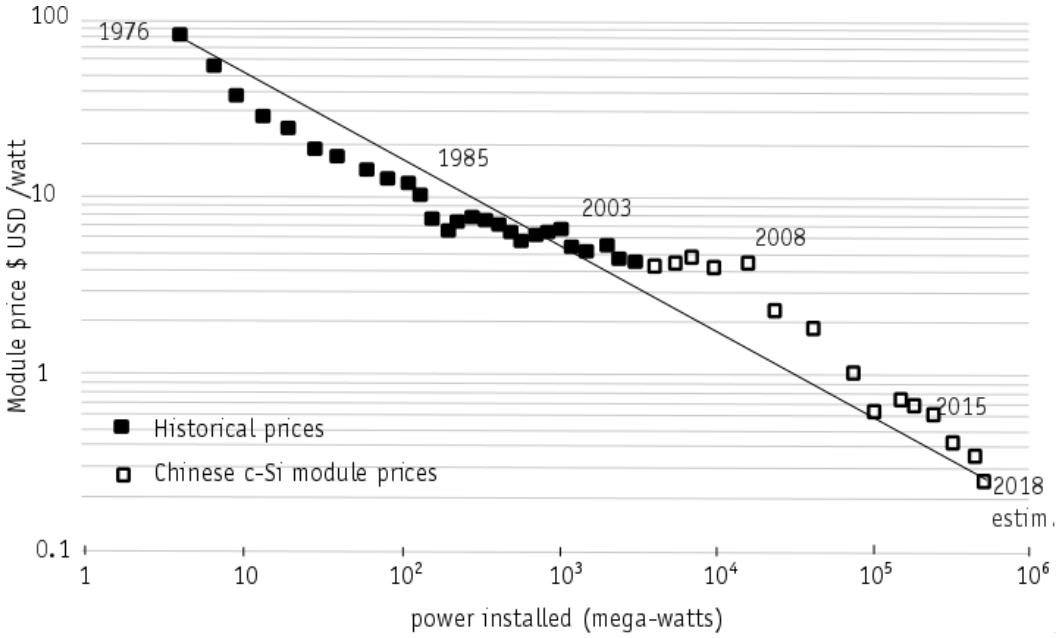


Figure 1.1.1: Learning curve for crystalline silicon-based solar cells. Adapted from Ref. 2 .

common metallic impurity in Cz-Si or UGM-Si, there is evidence for a correlation between the hydrogenation of Si samples and the reduction in concentration of charge carrier traps related to iron interstitial was observed [22]. Transition metals located leftmost in the periodic table, such as titanium (Ti) or vanadium (V), might not be as common as iron, nevertheless, as shown in figure 1.1.2, their effect on the cell efficiency can be quite harmful, even in relatively low concentrations. This is aggravated by the fact that these two impurities, similarly to other early 3d and 4d metals[1], have high diffusion barriers in bulk Si, making them difficult to deal with by means of a gettering treatment [23]. The formation of Ti-H and V-H complexes is supported by both experimental evidence [24, 25] and theoretical calculations [26, 27], with evidence even suggesting the formation of electrically inert metal-hydrogen complexes [24, 28]. The atomic structure and number of hydrogen atoms present in these complexes are still up to discussion. In the following section the physical properties of 3d and 4d transition metal impurities in a silicon crystal environment are discussed, particularly in the case of elements from groups IV to VI and iron. Later on, the existing state-of-the art concerning hydrogen and its interaction with metallic impurities is introduced, in order to lay a foundation for the issues discussed in later chapters.

## 1.2 Transition Metals in silicon

The physical properties of transition metals in silicon have been a subject of research for over seven decades, with multiple reviews over the years [4, 23, 30–32]. In the early 1960s, Ludwig and Woodbury reported [33, 34] spin resonance studies of multiple 3d transition metal impurities such as vanadium, chromium or iron. The results suggest that these impurities can either be found in the substitutional (S) site or in the interstitial site with tetrahedral symmetry (T). Complementarily to these results they presented a qualitative model of the splitting of the 3d orbitals under the perturbation of the crystal field for both S and T sites

[1]Note: the 3d (or, correspondingly, 4d) notation indicates the outer electron configuration of the neutral atom.

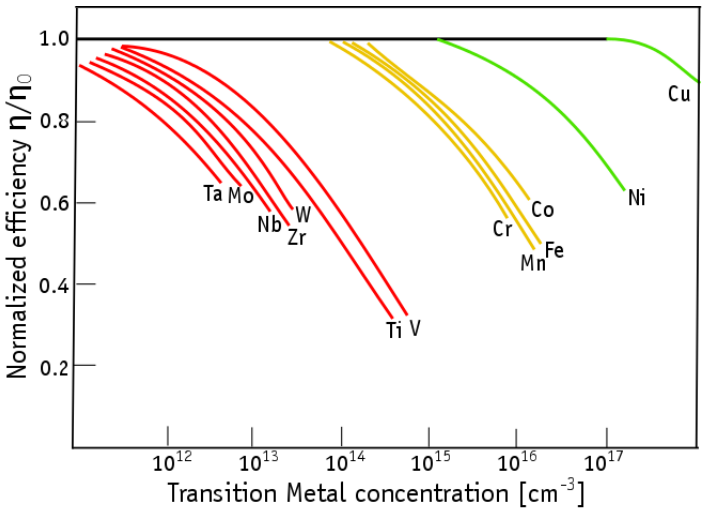


Figure 1.1.2: The effect of metallic contaminants on solar cell efficiency. The impurity concentration is that in the slice prior to cell processing. Data obtained from references [18, 19] and re-plotted by Pizzini *et al.* in [29].

and, from there, predicted the magnetic moment of several TM species in Si and compared to the spin resonance results. In this model, the 3d orbitals are split into a triplet and a doublet states that are filled with electrons according to Hund's rule, leading to maximum spin configurations. In the T site the doublet stands above the triplet while in the S site the order is reversed due to the interaction with the electronic states originating from the silicon vacancy that is filled by the substitutional impurity (see example in figure 1.2.1). In fact, in thermal equilibrium, the majority of the metallic impurities from the 3d row should be found preferentially in the T sites of the lattice when isolated [23, 35, 36]. However, the tendency is that, as the atomic number increases, the formation of substitutional species becomes more likely [23]. More than twenty years after the model proposed by Ludwig and Woodbury, the first *ab-initio* calculations using the local density approximation with the use of Green function methods were employed in the determination of the electronic structure of several 3d transition metal impurities [37–40]. These calculations confirmed most of the predictions made by the models of Ludwig and Woodbury and also allowed for a more quantitative approach to the electronic structure associated to these defects and provided a rough estimate of some of the positions of their donor levels in the silicon gap (typically overestimating the contemporary experimental measurements by $\sim 0.3\,\mathrm{eV}$). For instance, in the case of iron interstitial, De Leo *et al.* [37, 38] obtained an early estimate for a $(0/+)$ donor level at $E_\mathrm{v}{+}0.68\,\mathrm{eV}$, while experimental data available at the time [41, 42] pointed out to a level close to $E_\mathrm{v}{+}0.4\,\mathrm{eV}$. With the application of the same methods, the impurities of the 4d row were predicted to be more stable at substitutional sites than at the tetrahedral interstitial sites [43]. Nevertheless, the existing evidence suggests the opposite [44, 45]. In fact, concerning electrical activity, the 4d and 5d transition-metals typically follow a similar trend to their respective 3d counterpart for the same group of the periodic table [23]: for instance, the species from groups IV and V, titanium/zirconium/hafnium (Ti/Zr/Hf) and vanadium/niobium/tantalum (V/Nb/Ta) present four charge states $(-/0/+/++)$, resulting in three transition levels (acceptor, donor, and double donor). On the other hand, the species from the group VI, chromium/molybdenum/tungsten (Cr/Mo/W) present a single donor level. The same trend follows for other groups in the transition metal region of the periodic table, with a few notable exceptions, such as group VIII, where Rubidium (Rb) and Osmium

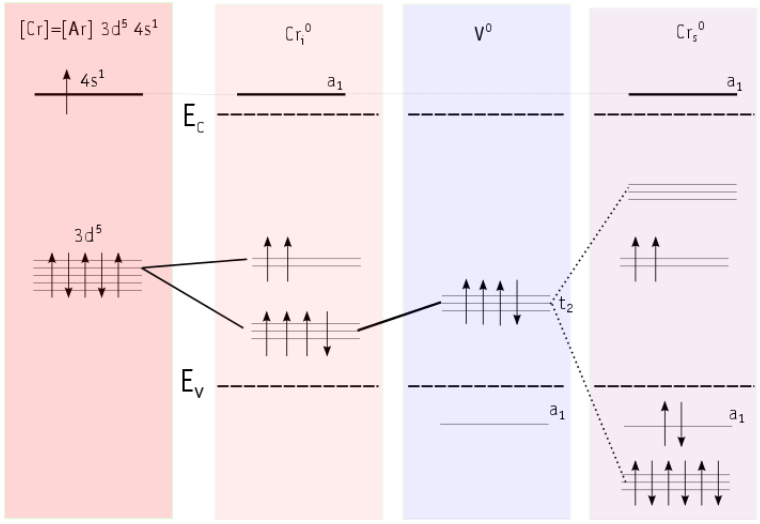


Figure 1.2.1: Splitting of the chromium 3d states under a tetrahedral crystal field in specific sites of the silicon lattice. The first column shows the electronic configuration of isolated Cr; the second column shows the electronic configuration of Cr at the tetrahedral interstitial site; the third column shows the electronic states resulting for a silicon vacancy; the last column displays the result of the interaction between the states of Cr and the Si vacancy, leading the electronic structure of substitutional Cr. The top of the valence band $E_v$ and bottom of the conduction band $E_c$ are represented by horizontal dashed lines.

(Os) present two levels (acceptor and donor) whereas Fe has only one measured donor level. This pattern is supported by the existing deep level transient spectroscopy (DLTS) data produced over the years reporting the electrical levels associated to both 3d and 4d TM impurities including the ones in the scope of this work, i.e. Ti, V, Cr, Zr, Nb, Mo and Fe [18, 25, 41, 42, 44, 46–55]. These levels are presented in table 1.1. More recently, light 3d-row TM impurities in Si have been subjected to the scrutiny of modern density functional theory (DFT) calculations using transferable pseudo-potentials, and including full structural relaxation effects in periodic supercells [27, 36, 56–59]. These calculations confirm the model from Ludwig and Woodbury for the electronic structure of transition metals in silicon and bring an improved numerical accuracy when compared to the results from the early 1980s [37–40, 43].

### 1.2.1 Titanium

Because it is a constituent of modern contact systems [23], and due to its deep electrical activity in silicon, titanium is considered a relevant transition metal contaminant in silicon. Ti is most stable at the tetrahedral interstitial site [60], however, substitutional Ti can be observed at high annealing temperatures (600–900 °C) in the presence of implantation-induced vacancies [59]. As a result of the 3d orbital splitting, the Ti interstitial has a triplet state in the gap, occupied by four electrons. The most stable spin configurations, as predicted by DFT calculations, for the negative, neutral, positive and double positive charge states are 1/2, 1, 3/2 and 1 respectively [58]. DLTS data reported over the years [48, 53, 61] supports the existence of an acceptor level at $E_c-0.09$ eV, a donor level at $E_v+0.87$ eV and a double donor at $E_v+0.26$ eV. More recently, Kolkovsky *et al.* [55, 62] proposed a different assignment: they assign the $E_c-0.09$ eV level (DLTS peak labeled as E40) to the first donor of interstitial Ti and attribute the $E_v + 0.87$ eV transition to a substitutional Ti acceptor level. This assignment

is due to the observed increase of the emission rates of the E40 level when increasing reverse bias. In their interpretation, which takes Poole-Frenkel effects into consideration, this is representative of a donor level. Relatively recent *ab-initio* calculations [58] predict single and double donor levels at $E_v + 0.76$ eV and $E_v + 0.15$ eV, more in agreement with the old view. However, they did not predict any acceptor level. There is a reported experimental value [63] of 1.79 eV for the activation energy for the diffusion of titanium in Si, indicating its low diffusivity under standard conditions.

### 1.2.2 Vanadium

Vanadium contamination is usually correlated with high iron concentrations in the material. This is due to the use of steel-based manufacturing components that include additions of vanadium [23]. The electronic structure of vanadium has been addressed early by means of spin resonance studies in the 1960s [33] and Green function cluster calculations in the 1980s [38]. The splitting of the 3d orbital produces a triplet and a doublet in the gap, although for all the charge states that are known, the doublet was predicted to remain empty due to the magnitude of the splitting. The ground states for interstitial vanadium in Si are ${}^{0}V_i^{-}$, ${}^{1/2}V_i^{0}$, ${}^{1}V_i^{+}$ and ${}^{3/2}V_i^{++}$ [27]. DLTS experiments on silicon samples contaminated with vanadium [25] reported an acceptor level at $E_c - 0.20$ eV, a donor level at $E_v + 0.72$ eV and a double donor at $E_v + 0.34$ eV. The experimental value in the literature for the migration barrier of interstitial V is 1.55 eV [64]. Recently, density functional theory calculations concerning the electronic structure of vanadium in silicon were reported [27]. For the case of vanadium interstitial, the authors obtained the same charge/spin states as the ones predicted by the model of Ludwig and Woodbury. The calculated transition levels are $(++/+)$ at $E_v$+0.40 eV, $(+/0)$ at $E_v$+0.65 eV and $(-/0)$ at $E_c$−0.24 eV, in good agreement with the aforementioned DLTS measurements. In the same publication, the formation of vanadium substitutional upon interaction of vanadium interstitial is also explored. The calculated binding energy of $V_s$, considering that all defects involved are in the neutral charge state, resulting from the reaction between the vanadium interstitial and a silicon vacancy is 3.02 eV. The authors also determined a relatively shallow acceptor level for vanadium substitutional $V_s(-/0) = E_c - 0.91$ eV.

### 1.2.3 Chromium

Similarly to vanadium, chromium produces and triplet and a doublet in the gap, but, in this case, spin resonance measurements [33] give a 5/2 spin value for the $Cr^+$ which indicates that both duplet and triplet are occupied by electrons (5 in total for the positively charged state). Experimental work by Feichtinger and Szaputa [42] only provides evidence for the existence of a single donor level at $E_v$+0.94 eV resulting from EPR with Hall effect measurements. Other experiments [18, 47] report a second donor level in the region of $E_v + 0.11$ to $E_v + 0.31$ eV. It is also possible that these levels are connected to Cr-B complexes since the material was B-doped and chromium interstitials can diffuse, with a barrier of 0.85 eV at room temperature [65], and be captured by a boron substitutional.

### 1.2.4 Iron

Among the metallic impurities addressed in this thesis, iron was the most intensively researched, with several reviews available in the literature [30, 32, 66]. Fe related defects were also studied in the works of Ludwig and Woodbury [33]. With the application of their model

to the EPR data, along with the previously observed donor character of iron impurities [41], they concluded that iron should also be preferably located at interstitial sites. They also assigned the spin configuration S=1 to the neutral iron interstitial species $Fe_i^0$. Electron nuclear double resonance (ENDOR) experiments [67] confirmed the tetrahedral interstitial lattice site for iron impurities. Nevertheless, there is also evidence pointing out to the formation of substitutional iron defects. From the analysis of the angular distribution of $\beta^-$ particles emitted from previously implanted $^{59}$Fe isotopes, Wahl *et al.* [68, 69] observed that, for annealing temperatures between 500 and 700 °C , the majority of the iron is located near the tetrahedral interstitial site. However, for annealing temperatures above 800 °C, the ratio of iron substitutional to interstitial starts to increase. Information concerning the lattice position of iron was also provided by Mössbauer experiments [70–74]. These Experiments consist in the implantation of $^{57}$Mn isotopes that decay into $^{57}$Fe with a half -life of $\tau_{1/2} \sim 90\,s$. The recoil resulting from this decay leads to the formation of a $Fe_i$-vacancy pair. While the isomer shifts $d$ in the range of $d = 0.76$-$0.86\,\mathrm{mm/s}$ associated to iron interstitial were dominant, there was also a set of peaks with isomer shifts $d = -0.08\mathrm{mm/s}$ and $d = 0.03\mathrm{mm/s}$ that were assigned to iron substitutional. Factors like temperature increase and introduction of vacancies were argued to be favorable for the formation of $Fe_s$ [75].

Compared to early 3d metals such as titanium and vanadium, experiments suggest that iron diffuses interstitially with a lower migration barrier. By fitting the existing data at the time for a wide range of temperatures, Weber [35] derived an expression for the diffusivity of iron as $D_{\mathrm{Fe}} = 1.3 \times 10^{-3} \exp(-0.68/k_{\mathrm{B}}T)$, where $k_B$ is the Boltzmann constant in units of eV/K, which implicates a diffusion barrier of 0.68 eV. Concerning electrical activity, it is well established that iron interstitial produces a donor level at $E_{\mathrm{v}} + 0.375\,\mathrm{eV}$ [76]. In the case of iron substitutional, there is no strong evidence pointing out to the existence of electrical activity. However, there is an attempted assignment of a level around $E_{\mathrm{c}} - 0.4\,\mathrm{eV}$ observed in iron-doped, n-type, Floating Zone Si to an acceptor state of $Fe_s$ [77]. This assignment is supported by the first-principles calculations reported by the Estreicher group [56, 78] which predict a deep acceptor level $(-/0)$ for $Fe_s$ at $E_{\mathrm{c}} - 0.41\,\mathrm{eV}$ Calculations from the same group predict a $(0/+)$ transition level associated to $Fe_i$ that perfectly matches the experimental observations.

### 1.2.5 Molybdenum

Concerning molybdenum impurities in silicon, early DLTS studies report a well established donor-like level at $E_{\mathrm{v}} + 0.30$ eV [46, 52]. There are also studies proposing a level [54]($E_{\mathrm{c}} - 0.27$ eV) or even multiple levels [49] ($E_{\mathrm{c}} - 0.34$ and $E_{\mathrm{c}} - 0.27$ eV) in the upper part of the band gap. However, there is no ascribing of these levels to the molybdenum interstitial rather than to any other molybdenum-related defect. The reported experimental value of the migration barrier of Mo in Si is 2.2 eV [79]. Recently, [45] the formation of molybdenum nano-precipitates in samples with typical concentrations of Mo for solar-grade silicon ($[Mo] \sim 10^{13}\mathrm{cm}^{-3}$) with dimensions in the order of $2 - 10\,\mathrm{nm}$, has been observed by means of transmission electron microscopy (TEM). These findings open the possibility for other slow-diffusing metallic impurities to form other nano-precipitates, given that they exist in high enough concentrations in the material.

### 1.2.6 Zirconium and niobium

Zirconium and niobium are not common constituents of manufacturing components for Si-based solar device fabrication, consequently they are not so relevant from the technological

point of view when compared to the previously mentioned transition metals. Nevertheless, from the fundamental point of view, they are needed to establish the trend of the electrical properties of 4d metals up to molybdenum and thus, these two metal impurities are addressed in this thesis as well. Early DLTS [44] measurements on Floating Zone- Zr doped-silicon samples show three levels at $E_c-0.14\,\text{eV}$, $E_v+0.76\,\text{eV}$ and $E_v+0.32\,\text{eV}$ related to Zr; the authors assign these three levels to Zr$(-/0)$, Zr$(0/+)$ and Zr$(+/++)$ transitions, following the same pattern as Ti. In 2001, Quevedo-Lopez and co-workers [80] observed the incorporation of Zr impurities into Si resulting from the deposition of $ZrSi_xO_y$ thin films (4-5 nm thick) over p-type bulk Si substrates, with the purpose of studying the properties of $ZrSi_xO_y$ as a gate dielectric for CMOS technology. The authors determined a diffusion coefficient $D_0 \sim 2\times10^{-15}\,\text{cm}^2\text{s}^{-1}$ at 1050 °C which is relatively low when comparing to other metallic impurities such as Iron ($D_0 \sim 4\times10^{-6}\,\text{cm}^2\text{s}^{-1}$ at 1100 °C [35]) or even Titanium ($D_0 \sim 3.5\times10^{-9}\,\text{cm}^2\text{s}^{-1}$ at 1100 °C [63]). Concerning niobium, early studies performed by means of space charge techniques resulted in three levels reported at $E_c - 0.293\,\text{eV}$, $E_v + 0.583\,\text{eV}$ and $E_v + 0.163\,\text{eV}$ [81]. More recently, these three levels were observed by means of DLTS at $E_c-0.32\,\text{eV}$, $E_v+0.57\,\text{eV}$ and $E_v+0.21\,\text{eV}$ [51].

## 1.3 Hydrogen in Silicon

Hydrogen has been shown to be able to cancel or mitigate the electrical activity associated to defects such as vacancies, shallow donors, metallic and non-metallic impurities or even extended defects, resulting in the overall improvement of the lifetime of charge carriers [16, 17]. In the specific case of solar silicon, hydrogen passivation is particularly effective, given the fact that (i) hydrogen can be easily introduced in the material, usually by depositing a hydrogen-soaked silicon nitride antireflection front coating [14, 15], (ii) atomic H can diffuse quickly through the material, being mobile even below room temperature and (iii) hydrogen binds strongly to silicon radicals and several impurities in Si, with binding energies usually above 1 eV [82]. In this section, the physical properties of hydrogen in silicon are briefly discussed, taking as motivation the application of this knowledge in the study of physical properties of TM-H complexes.

### 1.3.1 Structural properties

Hydrogen in silicon usually presents itself in the single interstitial configuration or in the form of hydrogen pairs [82]. Due to the high mobility of the H interstitial in Si, the measurement of its physical properties is usually done in samples at cryogenic temperatures. This defect has been studied by means of electron paramagnetic resonance (EPR) [83], Infra-Red (IR) absorption spectroscopy [84] and deep level transient spectroscopy (DLTS) [85]. Two different configurations have been observed: the first one consists of a hydrogen interstitial located at the center of an Si-Si bond ($H_{BC}$ configuration) and is the most stable configuration in the positive and neutral charge states. The second defect structure is a hydrogen tetrahedral interstitial ($H_T$ configuration), which is the ground state when the defect is negatively charged. Indirect evidence for these structures comes from muonium (Mu) spin rotation (μSR) studies [86]. Muonium is a pseudo-isotope of hydrogen with an anti-muon nucleus. The Mu ion $\mu^+$, a particle with spin 1/2, has a considerably short lifetime ($2.2\,\mu\text{s}$) ruling out possible interactions with other impurities and allowing the determination of hyperfine structure of muonium centers. Both $Mu_{BC}$ and $Mu_T$ configurations have been observed in the neutral/positively and neutral/negatively charged states, respectively.

In the case of hydrogen pairs there are two dominant structures: The hydrogen molecule, located at a tetrahedral interstitial site, and the $H_2^*$ structure, where one of the hydrogen atoms is located at the Si-Si bond center site while the other one is located close to the nearest tetrahedral site (usually referred as the *anti-bonding* (AB) site since the hydrogen atom stands in the opposite direction of the nearest Si-Si bond). The $H_2$ molecule structure was proposed in the early 1980s [87] and a corresponding stretching mode was observed in Si by Raman spectroscopy in 1998 [88]. Results indicate that the H-H bond is longer and weaker inside bulk Si than it is in free space. On the other hand, the $H_2^*$ does not form spontaneously, but was observed in proton implanted samples by means of Fourier transform infrared (FTIR) spectroscopy [89].

### 1.3.2 Electrical properties

Theoretical calculations predict that, at thermodynamic equilibrium, the single hydrogen interstitial cannot be found in the neutral charge state, regardless of the Fermi level position [82]. In p-type and intrinsic Si the most stable configuration is the $H_{BC}^+$, which acts as a donor, while in n-type Si, $H_T^-$ is energetically favored, acting as an acceptor. This leads to an inverted order of the defect transition levels in the gap, i.e., the acceptor level is below the donor level, and, consequently, the existence of a H(−/+) occupancy level somewhere in the middle of the band gap. Defects with such electronic structure are referred in the literature as negative-*U* centers. Experimental observation of these levels is a tricky task, not only for the reasons mentioned above (hydrogen is a fast diffuser in Si) but also because the neutral configurations are not stable in equilibrium. DLTS data shows a single donor level (0/+) associated to $H_{BC}$ in the range $E_c-0.16$ to $E_c-0.175$ eV [85] corresponding approximately to its ionization energy. Nielsen *et al.* were able to give an estimate of the acceptor level at about $E_c-0.65$ eV[85]. These results led to an estimate of the H(−/+) occupancy level to be located near $E_v-0.4$ eV. The transition associated to the (−/+) occupancy level occurs in 3 steps: (i) negatively charged hydrogen captures a hole $h^+$: $H_T^- + h^+ \longrightarrow H_T^0$, (ii) the metastable neutral hydrogen in the tetrahedral site moves to the bond center site $H_T^0 \longrightarrow H_{BC}^0$ and (iii) $H_{BC}^0$ captures another hole and becomes positively charged: $H_{BC}^0 + h^+ \longrightarrow H_{BC}^+$. The reverse process is achieved with the capture of excess electrons. The $H_T^0 \longrightarrow H_{BC}^0$ and $H_{BC}^0 \longrightarrow H_T^0$ barriers are 0.2 eV (estimated) and 0.295 (observed) respectively [85], indicating that this transition happens well below room temperature. These values also suggest that $H_{BC}^0$ is more stable than $H_T^0$ by about 0.1 eV. The formation energy diagram in Fig.1.1 displays the dependence of the charge state and configurations of atomic hydrogen as a function of the fermi level.

In the case of the hydrogen pairs, electrical levels were neither observed nor predicted theoretically, thus being electrically inert [82].

### 1.3.3 Diffusion and kinetics

As mentioned before, atomic hydrogen is a fast diffuser in Si at relatively low temperatures. It shows a diffusivity of $9.4 \times 10^3 \exp(-\Delta E_{dif}/k_B T)$ $cm^2 s^{-1}$ [82] (intrinsic and p-type material), where $\Delta E_{dif}$ is the diffusion barrier of $H^+$ traveling between BC sites with an experimental value of 0.48 eV. This result confirms several theoretical calculations that set this value in the range between 0.38 and 0.5 eV[90]. The calculated value for the migration barrier $H_T^-$ was calculated to be 0.39 eV. Estimates from both theoretical and experimental data suggest that the migration barrier of $H_T^0$ is substantially smaller, with a calculated value of 0.11 eV [85, 90].

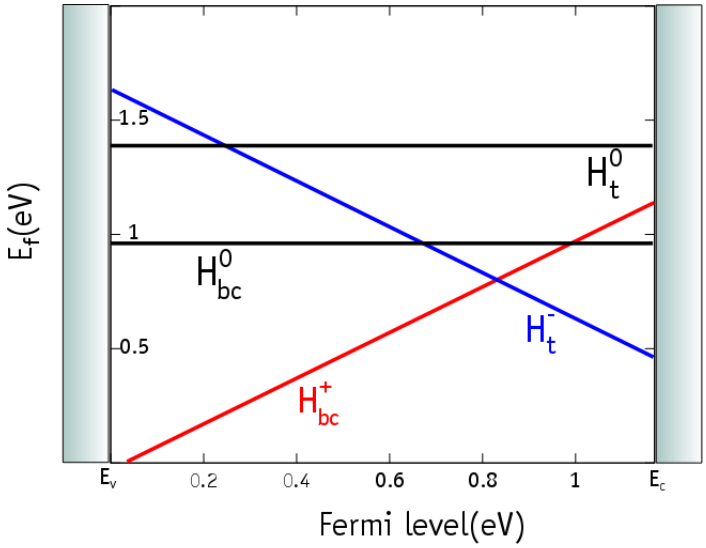


Figure 1.3.1: Formation Energy diagram of atomic hydrogen in silicon bulk. Each segment corresponds to the formation energy of each configuration and charge state as a function of the Fermi level. The intersection between the $H^+_{BC}$ and $H^-_T$ lines defines the occupational $(-/+)$ negative-$U$ level. This diagram was obtained through the method presented in Subsection 2.4.3, using defective 216-Si supercells hosting hydrogen interstitial defects. The values for the electrical levels $H_{BC}(0/+) = E_c - 0.16\,\text{eV}$ and $H_T(0/-) = E_c - 0.65\,\text{eV}$ are taken from the experimental estimates from Ref. [85].

### 1.3.4 Local vibrational modes

The single hydrogen interstitial has several vibrational modes. $H^+_{BC}$ presents an antisymmetric stretch mode at $1998\,\text{cm}^{-1}$ observed experimentally [82]. There are theoretical predictions [90] for a wag mode at $309\,\text{cm}^{-1}$, and for a symmetric stretch of the two Si nearest neighbors, at $397\,\text{cm}^{-1}$. There is also a theoretical antisymmetric stretch mode for $H^0_{BC}$ at $1780\,\text{cm}^{-1}$, as well as a singlet-stretching and a doublet-wag for $H^-_T$ at $528\,\text{cm}^{-1}$ and $514\,\text{cm}^{-1}$ respectively. In the case of the hydrogen molecule there are two Raman peaks corresponding to two distinct rotational-vibrational states of the $H_2$ molecule in the tetrahedral cage at $3618\,\text{cm}^{-1}$ and $3627\,\text{cm}^{-1}$ [91]

## 1.4 Interaction between Hydrogen and Transition Metals

Atomic hydrogen is a very mobile impurity in silicon and is likely to be captured by other impurities and defects, transition metals included. Studies reporting the interaction between hydrogen and transition metal impurities in silicon bulk material date back to 1984, with the observation of a passivation effect of deep levels related to gold, silver (Ag) and iron, caused by the introduction of hydrogen in the samples [92]. Concurrently, Singh and co-workers [93] studied the interaction between hydrogen and several transition metals, including slow diffusing metals such as Ti and V, and fast diffusing metals such as Cr and Au, in p-type and n-type Si samples annealed at 400 K, by means of DLTS. While they could not observe any type of passivation of the deep levels associated to Ti and V, the authors report a decrease in concentration of the levels related to Cr and Au. They also propose that this decrease in concentration of defects related to fast diffusing metal impurities is not due to the formation of Cr-H or Au-H complexes, but rather due to an enhancing effect that hydrogen can have

in the gettering process for these impurities. It was later verified [24] that in the conditions of their experiment (400 K reverse-bias annealing) it was indeed not possible to observe the formation of transition metal-hydrogen complexes. However, under a zero-bias annealing, two new DLTS peaks arise as a result from the introduction of hydrogen, corresponding to a reduction in intensity of peaks associated to transition metals (Ti in this particular case). Concerning the transition metal impurities addressed in this thesis, there is solid evidence for the formation Ti-H [24, 53], V-H [94] Cr-H [94] and Fe-H [95] complexes. There are also two unidentified levels related to a possible molybdenum-hydrogen complex [49, 54]. It is worth mentioning that these observations took place in n-type material, whereas in p-type material, TM-H complexes are typically not observed.

### 1.4.1 Titanium-Hydrogen

Jost and Weber [24] assigned two DLTS bands at $E_c - 0.31\,\text{eV}$ and $E_c - 0.57\,\text{eV}$ to a possible Ti-H complex (or complexes). However, the intensity of those lines could not fully account for the decrease in concentration of the Ti levels relatively to the measurements made prior to the hydrogenation. These results strongly suggest the existence of a fully passive Ti-H complex. The concentration of this passive complex was estimated to exceed the concentrations of the observed levels by an order of magnitude. The authors also found that, after a 3-hour annealing treatment at 400 K, all the Ti-H related levels were annealed out and the original concentration of $Ti_i$ was restored.

More recently, Leonard *et al.* [53] reported the existence of three DLTS bands related to the formation of Ti-$H_n$ complexes. Two of these three bands, labeled as E170 and E270, are consistent with the measurements of Jost and Weber, with measured activation energies of 0.34 eV and 0.56 eV for electron emission to the conduction band bottom. In addition, they detected the existence of a shallow electron trap, labeled as E40', at $E_c - 0.075$ eV. Considering the concentration depth profiles of E40', E170 and E270, the authors argue that each of these levels is related to Ti-H complexes with different number of hydrogen atoms. Their results also support the formation of a fully passivated Ti-H complex. The authors also state that the E170 peak is a superposition of two peaks, E170 and E170'.

On the theoretical side, first principles calculations concerning this subject were recently reported [26]. Two structures that produce electrical levels seemingly consistent with the aforementioned DLTS data were proposed. The first one, labeled as $Ti_i$-H with the hydrogen bound to the titanium interstitial along the [111] (or equivalent) direction in opposition to a first neighboring Si atom. In the second proposed structure, labeled as $Ti_i$-$H_{bc}$, an Si atom neighboring the interstitial Ti is moved along the trigonal axis, while the Ti atom itself moves from the (T) site to increase the overlap with the dislocated Si. The Si dangling bond arising from this configuration is filled up with a hydrogen atom. The first donor levels of these complexes, labeled as $\{Ti_i - H_{ab}\}(0/+)$ and $\{Ti_i - H_{bc}\}(0/+)$ are predicted to be at $E_c - 0.38\,\text{eV}$ and $E_c - 0.57\,\text{eV}$ respectively, close to the levels related to the E170 and E270 DLTS bands (ab and bc indexes stand for interstitial site in oposition to the nearest silicon neighbour and Si-Si bond-center site respectively). The formation of complexes containing multiple hydrogen atoms such as Ti-$H_2$ and Ti-$H_3$ was predicted to be energetically unfavorable relatively to structures such as $Ti_i$ and Ti-H accompanied by a separate $H_2$ molecule. However, this picture does not explain the experimental data in full, since the concentration depth profiles in Ref. 53 strongly suggest that the observed DLTS bands arise from Ti-$H_n$ complexes with different number of hydrogen atoms. The authors from Ref. 26 predict that Ti-$H_4$ is a stable and electrically inactive complex, supporting the hypothesis of the formation of a fully passivated Ti-H complex. These issues are explored in more detail in Chapter 4.

### 1.4.2 Vanadium-Hydrogen

In a study published by Sadoh *et al.* [25] several DLTS peaks associated to V and V-H complexes were reported. Three out of the four detected peaks are simply related to vanadium, whereas the fourth one, which was found near the regions etched with an acid mixture containing HF and $HNO_3$, was assigned to a V-H complex. This peak (labeled as E3) corresponds to a level at $E_c - 0.49$ eV. More recently, Mullins and co-workers [28] also observed this level and assigned it to a donor-like state of V-H. They also observed another DLTS signal (labeled as E5) corresponding to a level at $E_c - 0.18\,\text{eV}$ that is likely to arise from a different V-H complex. After a 30 min. annealing at 200 °C these levels vanish and the initial concentration of vanadium is restored. However, the authors also pointed out that, after annealing the hydrogenated samples at temperatures between 100 °C and 150 °C, the sum of the concentrations of V and V-H related defects was lower, by at most 20%, than the original concentration of V, suggesting the possibility for the formation of fully passivated V-$H_n$ complexes. Concerning first-principles calculations, Backlund [58] *et al.* predicted the formation of a $V_i$-H complex, with a structure similar to $Ti_i$-H, with a binding energy of 1.15 eV, consistent with the aforementioned annealing temperature of 200 °C, and predicted a donor level at $E_v - 0.61\,\text{eV}$ which they assigned to the E3 DLTS signal. They also found an acceptor level associated to the $V_i$- H complex close to the conduction band. However it is pointed out that the prediction of levels close to the bands is always questionable.

### 1.4.3 Chromium-Hydrogen

In a DLTS study published by Sadoh and co-workers [94], four deep levels related to Cr and Cr-H complexes were found at $E_c - 0.22\,\text{eV}$, $E_c - 0.28\,\text{eV}$, $E_c - 0.45\,\text{eV}$ and $E_c - 0.54\,\text{eV}$. While the $E_c - 0.22\,\text{eV}$ level is due to chromium interstitial, the other three levels were only detected in regions near the surface of the samples near the hydrogen source. These levels anneal out at temperatures above 175 °C. Since the characteristics of the thermal stability are different among these three levels, it was proposed that they must be assigned to three different Cr-H complexes.

### 1.4.4 Iron-Hydrogen

It is well established that the introduction of hydrogen in silicon samples containing iron impurities leads to the mitigation of iron-related electrical activity [22, 96]. However, the mechanisms that led to this mitigation effect are still a matter of debate. It was observed by means of thermally stimulated capacitance (TSCAP) [95] and electron spin resonance (ESR) measurements [97] that iron interstitial interacts with hydrogen to form an Fe-H complex. This complex produces an electrical level at $E_v + 0.31\,\text{eV}$ [95], and dissociated after annealing at $\sim 200\,°\text{C}$ [95, 97]. However, the mitigation effect on the iron-interstitial electrical activity persists up to annealing temperatures of 400 °C [22]. The hypotheses proposed in the literature to explain this phenomenon are the following: **I** The introduction of hydrogen provides a diffusion enhancement effect to iron interstitial, which aids the gettering process [22]. **II** Formation of iron substitutional due to high temperature and/or introduction of vacancies due to the hydrogenation methods used [75]. **III** Formation of an unknown, passive Fe-H complex with a higher binding energy [96]. On the theoretical side, Szwaky and co-workers [75] predict a stable $Fe_i$-H complex which suits the electrical level and annealing temperature observed through the previous TSCAP measurements[95]. However, the authors also explored the possibility of formation of $Fe_s$-H complexes. They predicted a stable defect with hydrogen rotating "extremely fast" around the iron substitutional. They also hypothesized that the ESR

observations [97] of a Fe-H complex with tetrahedral symmetry should in fact correspond to their $Fe_s - H$ model, since the structure of the $Fe_i$-H model has trigonal symmetry with iron located at the hexagonal interstitial site. This problem is discussed in detail in Chapter 5.

## 1.5 Objectives and structure of the thesis

The main aim of this thesis is to provide a theoretical assessment of issues related to transition metals and their interaction with hydrogen in bulk Si, and by that way to complement the existing experimental work that has been done on this subject and establish a set of theoretical models that are consistent with the existing evidence. This objective was accomplished with the use of *ab-initio* methods based on Density Functional Theory (DFT) with the application of DFT-based codes, namely `AIMPRO` [98], `VASP` [99–101] and `QUANTUM-ESPRESSO` [102]. Most of the calculations presented on this thesis concern the composition, configuration, electronic structure and migration barriers of the defects under scrutiny. The thesis is structured as follows:

- **Chapter 2** provides an introduction to the density functional theory. The main approximations used in the thesis work are discussed. The methods for the calculation of observables are presented.

- **Chapter 3** is where the electronic structure of 3d and 4d transition metal impurities of groups 4, 5 and 6 is determined. The defects under scrutiny consist of isolated metallic impurities located at (or close to) the interstitial tetrahedral site, which is considered to be the most stable configuration for early transition metals. The use of a "cost-effective" description for the exchange and correlation interactions (see Chapter 2; Section 2.3.1) is discussed. Jahn-Teller distortion effects that arise from the splitting of degenerate orbitals are also taken into account. The main results presented in this chapter are the calculated transition levels and migration barriers of the aforementioned transition metal impurities. The results are compared to the existing experimental data. This chapter is an adaptation of:

  – A. G. Marinopoulos, *P. Santos, J. Coutinho, DFT+U study of electrical levels and migration barriers of early 3d and 4d transition metals in silicon*, Physical Review B, **92**, 075124 (2015)

- **Chapter 4** introduces the discussion of a possible passivation effect of metallic impurities provided by hydrogenation. The metallic impurity discussed here in particular is titanium, the only early transition metal impurity for which the existence of a full passivation effect is supported by both experimental evidence and theoretical calculations. Several stable titanium-hydrogen complexes are presented in this chapter followed by the determination of their electronic structure. The stability of these defects at equilibrium versus the doping level is discussed. This Chapter is an adaptation of:

  – P. Santos, J. Coutinho, V. J. B. Torres, M. J. Rayson, and P. R. Briddon, *Hydrogen passivation of titanium impurities in silicon: Effect of doping conditions*, Applied Physics Letters, **105**, 032108 (2014)

- **Chapter 5** addresses the question of the reduction of concentration of iron interstitials that happens upon hydrogenation of silicon samples followed by an annealing at high temperatures. Following a similar procedure to the previous chapter, the composition, atomic and electronic structure of iron-hydrogen complexes is determined, and

Table 1.1: Experimental observations of the electrical activity and diffusivity of $3d$ and $4d$ transition metals from groups IV, V and VI and iron. Known reports for electrical activity assigned to the respective metal-hydrogen complexes are also included. The values are followed by the respective reference.

| Impurity | Observed Lattice sites | Electrical levels (eV) | Diffusivity at $\sim 1000-1100\,^{\circ}$C ($\mathrm{cm^2 s^{-1}}$) | Electrical levels after hydrogenation (eV) | Notes |
|---|---|---|---|---|---|
| Ti | Interstitial | $E_c$−0.09<br>$E_v$+0.87[48]<br>$E_v$+0.26 | $3.5\times10^{-9}$[63] | $E_c-0.31$<br>$E_c-0.57$[53]<br>$E_c-0.075$ | Multiple Ti-H complexes. Evidence for the formation of a fully passivated Ti-H complex[53] |
| V | Interstitial | $E_c$−0.20<br>$E_v$+0.72[25]<br>$E_v$+0.34 | $2\times10^{-8}$[64] | $E_c-0.49$ [25] | Evidence suggesting the formation of a fully passivated V-H complex |
| Cr | Interstitial | $E_v$+0.94[42] | $2\times10^{-6}$[42] | $E_c-0.28$<br>$E_c-0.45$ [94]<br>$E_c-0.54$ | Multiple Cr-H complexes |
| Zr | Interstitial | $E_c$−0.14<br>$E_v$+0.76[44]<br>$E_v$+0.32 | $2\times10^{-15}$ [80] | | |
| Nb | Interstitial | $E_c$−0.32<br>$E_v$+0.57[51]<br>$E_v$+0.21 | - | | |
| Mo | Interstitial | $E_c$−0.27[49]<br>$E_v$+0.30 [46] | $9\times10^{-10}$[79] | | |
| Fe | Interstitial and Substitutional | $E_v$+0.39[76] ($Fe_i$) | $4\times10^{-6}$[35] | $E_v+0.31$[95] | Hydrogenation leads to decrease in $Fe_i$ concentration[22] |

the stability of these complexes for different doping levels is discussed. The migration barriers of iron-hydrogen interstitial complexes are also determined, in order to discuss a possible diffusion enhancement effect of iron provided by hydrogenation, that has been hypothesized in the literature. This chapter is an adaptation of:

  - P. Santos, J. Coutinho, S. Öberg, *First-principles calculations of iron-hydrogen reactions in silicon*, to be published in Journal of Applied Physics.

- **Chapter 6** focuses on a particular issue that arises from the introduction of hydrogen in silicon material for solar applications, which is the formation of strong recombination centers that result from the interaction of hydrogen with carbon-oxygen complexes. This issue is of particular interest, since these complexes are active recombination centers in n-type material. Given a recent tendency of the industry in moving towards n-type, due to problems related to transition metal impurities (strong recombination centers in p-type) and to boron (light induced degradation), this problem gains particular relevance in the scope of the thesis. In this chapter several stable configurations for the COH complex are presented. Following electronic structure calculations for all of these configurations, a model for the recombination mechanisms is proposed. DLTS measurements are also presented in this chapter, provided by a research group from Manchester, that worked in collaboration with our group on this particular issue. This chapter is an adaptation of:

  - P. Santos, J. Coutinho, S. Öberg, M. Vaqueiro-Contreras, V. P. Markevich, M. P. Halsall, A. R. Peaker, *Theory of a carbon-oxygen-hydrogen recombination center in n-type Si,* Physica Status Solidi A, **214**, No. 7, 1700309 (2017)

- **Chapter 7** provides a summary of the results displayed in the previous chapters and discusses these results in the light of the main scope of this thesis. Concluding remarks and discussion of future work are also part of this final chapter.

# Bibliography


[1] REN21, "Renewables 2018 global status report," Tech. Rep. (Paris: REN21 Secretariat, 2018).

[2] Bloomberg, "New energy outlook 2018," Tech. Rep. (New Energy Finance Bloomberg, 2018).

[3] I. Fraunhofer, "Photovoltaics report," Tech. Rep. (Fraunhofer Institute for Solar Energy Systems, ISE, 2018).

[4] A. R. Peaker, V. P. Markevich, B. Hamilton, G. Parada, A. Dudas, A. Pap, E. Don, B. Lim, J. Schmidt, L. Yu, Y. Yoon, and G. Rozgonyi, physica status solidi (a) **209**, 1884 (2012).

[5] G. Flamant, V. Kurtcuoglu, J. Murray, and A. Steinfeld, Solar Energy Materials and Solar Cells **90**, 2099 (2006).

[6] F. Chigondo, Silicon **10**, 789 (2018).

[7] J. Kraiem, B. Drevet, F. Cocco, N. Enjalbert, S. Dubois, D. Camel, D. Grosset-Bourbange, D. Pelletier, T. Margaria, and R. Einhaus, in *Photovoltaic Specialists Conference (PVSC), 2010 35th IEEE* (2010) pp. 001427–001431.

[8] C. Modanese, M. Di Sabatino, A.-K. Søiland, K. Peter, and L. Arnberg, Progress in Photovoltaics: Research and Applications **19**, 45 (2011).

[9] P. Zheng, F. E. Rougieux, X. Zhang, J. Degoulange, R. Einhaus, P. Rivat, and D. H. Macdonald, IEEE Journal of Photovoltaics **7**, 58 (2017).

[10] M. A. Green, Y. Hishikawa, E. D. Dunlop, D. H. Levi, J. Hohl-Ebinger, and A. W. Ho-Baillie, Progress in Photovoltaics: Research and Applications **26**, 3 (2017).

[11] F. Schindler, B. Michl, P. Krenckel, S. Riepe, J. Benick, R. Müller, A. Richter, S. W. Glunz, and M. C. Schubert, Energy Procedia **124**, 777 (2017), 7th International Conference on Silicon Photovoltaics, SiliconPV 2017, 3-5 April 2017, Freiburg, Germany.

[12] K. Yoshikawa, H. Kawasaki, W. Yoshida, T. Irie, K. Konishi, K. Nakano, T. Uto, D. Adachi, M. Kanematsu, H. Uzu, and K. Yamamoto, Nature Energy **2**, 17032 EP (2017).

[13] W. Shockley and H. J. Queisser, Journal of Applied Physics **32**, 510 (1961).

[14] F. Jiang, M. Stavola, A. Rohatgi, D. Kim, J. Holt, H. Atwater, and J. Kalejs, Applied Physics Letters **83**, 931 (2003).

[15] J. Holt, D. Goodwin, A. Gabor, F. Jiang, M. Stavola, and H. A. Atwater, Thin Solid Films **430**, 37 (2003), proceedings of the Second International Conference on Cat-CVD (Hot Wire CVD) Process.

[16] C. Dube and J. Hanoka, in *Photovoltaic Specialists Conference, 2005. Conference Record of the Thirty-first IEEE* (2005) pp. 883–888.

[17] S. Martinuzzi, I. Périchaud, and F. Warchol, Solar Energy Materials and Solar Cells **80**, 343 (2003).

[18] J. Davis, J.R., A. Rohatgi, R. Hopkins, P. Blais, P. Rai-Choudhury, J. McCormick, and H. Mollenkopf, Electron Devices, IEEE Transactions on **27**, 677 (1980).

[19] A. Rohatgi and P. Rai-Choudhury, Solar Cells **17**, 119 (1986).

[20] P. Deixler, J. Terry, I. D. Hawkins, J. H. Evans-Freeman, A. R. Peaker, L. Rubaldo, D. K. Maude, J.-C. Portal, L. Dobaczewski, K. Bonde Nielsen, A. Nylandsted Larsen, and A. Mesli, Applied Physics Letters **73**, 3126 (1998).

[21] C. G. Van de Walle, Journal of Vacuum Science and Technology A **16**, 1767 (1998).

[22] P. Karzel, A. Frey, S. Fritz, and G. Hahn, Journal of Applied Physics **113**, 114903 (2013).

[23] K. Graff, *Metal Impurities in Silicon-Device Fabrication* (Springer, Berlin, 1995).

[24] W. Jost and J. Weber, Physical Review B **54**, R11038 (1996).

[25] T. Sadoh, H. Nakashima, and T. Tsurushima, Journal of Applied Physics **72**, 520 (1992).

[26] D. J. Backlund and S. K. Estreicher, Physical Review B **82**, 155208 (2010).

[27] D. J. Backlund, T. M. Gibbons, and S. K. Estreicher, Physical Review B **94**, 195210 (2016).

[28] P. M. H. J. Mullins, V. P. Markevich and A. R. Peaker, physica status solidi (a) **213**, 2838 (2016).

[29] S. Pizzini, M. Acciarri, and S. Binetti, physica status solidi (a) **202**, 2928 (2005).

[30] E. R. Weber, Applied Physics A **30**, 1 (1983).

[31] K. Graff, Materials Science and Engineering: B **4**, 63 (1989).

[32] A. A. Istratov, H. Hieslmair, and E. R. Weber, Applied Physics A **69**, 13 (1999).

[33] H. H. Woodbury and G. W. Ludwig, Physical Review **117**, 102 (1960).

[34] G. W. Ludwig and H. H. Woodbury, Physical Review Lett. **5**, 98 (1960).

[35] E. Weber and H. G. Riotte, Journal of Applied Physics **51**, 1484 (1980).

[36] Z. Z. Zhang, B. Partoens, K. Chang, and F. M. Peeters, Physical Review B **77**, 155201 (2008).

[37] G. G. DeLeo, G. D. Watkins, and W. B. Fowler, Physical Review B **23**, 1851 (1981).

[38] G. G. DeLeo, G. D. Watkins, and W. B. Fowler, Physical Review B **25**, 4972 (1982).

[39] A. Zunger, Physical Review B **28**, 3628 (1983).

[40] H. Katayama-Yoshida and A. Zunger, Physical Review B **31**, 8317 (1985).

[41] C. B. Collins and R. O. Carlson, Physical Review **108**, 1409 (1957).

[42] H. Feichtinger and R. Czaputa, Applied Physics Letters **39**, 706 (1981).

[43] F. Beeler and M. Scheffler, in *Defects in Semiconductors 15*, Materials Science Forum, Vol. 38 (Trans Tech Publications, 1991) pp. 257–262.

[44] H. Lemke, physica status solidi (a) **122**, 617 (1990).

[45] S. Leonard, V. P. Markevich, A. R. Peaker, B. Hamilton, K. Youssef, and G. Rozgonyi, physica status solidi (b) **251**, 2201 (2014).

[46] A. Rohatgi, R. Hopkins, J. Davis, R. Campbell, and H. Mollenkopf, Solid-State Electronics **23**, 1185 (1980).

[47] T. Kunio, T. Yamazaki, E. Ohta, and M. Sakata, Solid-State Electronics **26**, 155 (1983).

[48] D. Mathiot and S. Hocine, Journal of Applied Physics **66**, 5862 (1989).

[49] T. Hamaguchi and Y. Hayamizu, Japanese Journal of Applied Physics **30**, L1837 (1991).

[50] T. H. Huang, H. Kinoshita, and D. L. Kwong, Applied Physics Letters **65**, 1829 (1994).

[51] M. L. Polignano, D. Codegoni, G. Borionetti, F. Bonoli, J. Brivio, S. Greco, A. Marino, P. Monge, I. Patoprsta, V. Privitera, and C. Riva, ECS Transactions **33**, 133 (2010).

[52] B. B. Paudyal, K. R. McIntosh, D. H. Macdonald, and G. Coletti, Journal of Applied Physics **107**, 054511 (2010).

[53] S. Leonard, V. P. Markevich, A. R. Peaker, and B. Hamilton, Applied Physics Letters **103**, 132103 (2013).

[54] S. M. Cox, ECS Journal of Solid State Science and Technology **3**, P397 (2014).

[55] V. Kolkovsky, L. Scheffler, and J. Weber, Physica B: Condensed Matter **439**, 24 (2014), 5th South African Conference on Photonic Materials (SACPM 2013).

[56] S. K. Estreicher, M. Sanati, and N. G. Szwacki, Physical Review B **77**, 125214 (2008).

[57] K. Sánchez, I. Aguilera, P. Palacios, and P. Wahnón, Physical Review B **79**, 165203 (2009).

[58] D. J. Backlund and S. K. Estreicher, Physical Review B **81**, 235213 (2010).

[59] V. P. Markevich, S. Leonard, A. R. Peaker, B. Hamilton, A. G. Marinopoulos, and J. Coutinho, Applied Physics Letters **104**, 152105 (2014).

[60] D. A. van Wezep, R. van Kemp, E. G. Sieverts, and C. A. J. Ammerlaan, Physical Review B **32**, 7129 (1985).

[61] A. C. Wang and C. T. Sah, Journal of Applied Physics **56**, 1021 (1984).

[62] V. Kolkovsky, L. Scheffler, and J. Weber, physica status solidi (c) **9**, 1996 (2012).

[63] S. Hocine and D. Mathiot, Applied Physics Letters **53**, 1269 (1988).

[64] T. Sadoh and H. Nakashima, Applied Physics Letters **58**, 1653 (1991).

[65] J. Zhu, J. Diz, D. Barbier, and A. Laugier, Materials Science and Engineering: B **4**, 185 (1989).

[66] A. A. Istratov, H. Hieslmair, and E. R. Weber, Applied Physics A **70**, 489 (2000).

[67] S. Greulich-Weber, J. R. Niklas, E. R. Weber, and J. M. Spaeth, Physical Review B **30**, 6292 (1984).

[68] U. Wahl, J. G. Correia, E. Rita, J. P. Araújo, and J. C. Soares (The ISOLDE Collaboration), Physical Review B **72**, 014115 (2005).

[69] U. Wahl, J. Correia, E. Rita, J. Araújo, and J. Soares, Nuclear Instruments and Methods in Physics Research Section B: Beam Interactions with Materials and Atoms **253**, 167 (2006).

[70] G. Langouche, Hyperfine Interactions **72**, 215 (1992).

[71] G. Weyer, S. Degroote, M. Fanciulli, V. N. Fedoseyev, G. Langouche, V. I. Mishin, A.-M. V. Bavel, A. Vantomme, and the ISOLDE Collaboration, in *Defects in Semiconductors 19*, Materials Science Forum, Vol. 258 (Trans Tech Publications, 1997) pp. 437–442.

[72] G. Weyer, A. Burchard, M. Fanciulli, V. N. Fedoseyev, H. P. Gunnlaugsson, V. I. Mishin, and R. Sielemann, Physica B: Condensed Matter **273**, 363 (1999).

[73] Y. Yoshida, Y. Kobayashi, A. Yoshida, X. Diao, S. Ogawa, K. Hayakawa, K. Yukihira, F. Shimura, and F. Ambe, Hyperfine Interactions **141**, 157 (2002).

[74] Y.Yoshida, S. Ogawa, and K. Arikawa, Physica B: Condensed Matter **340**, 605 (2003), proceedings of the 22nd International Conference on Defects in Semiconductors.

[75] N. G. Szwacki, M. Sanati, and S. K. Estreicher, Physical Review B **78**, 113202 (2008).

[76] H. Feichtinger, J. Waltl, and A. Gschwandtner, Solid State Communications **27**, 867 (1978).

[77] P. Kaminski, R. Kozlowski, A. Jelenski, T. Mchedlidze, and M. Suezawa, Japanese Journal of Applied Physics **42**, 5415 (2003).

[78] D. J. Backlund and S. K. Estreicher, Physical Review B **81**, 235213 (2010).

[79] J. L. Benton, D. C. Jacobson, B. Jackson, J. A. Johnson, T. Boone, D. J. Eaglesham, F. A. Stevie, and J. Becerro, Journal of The Electrochemical Society **146**, 1929 (1999).

[80] M. Quevedo-Lopez, M. El-Bouanani, S. Addepalli, J. L. Duggan, B. E. Gnade, R. M. Wallace, M. R. Visokay, M. Douglas, M. J. Bevan, and L. Colombo, Applied Physics Letters **79**, 2958 (2001).

[81] K. Schmalz, H. G. Grimmeiss, H. Pettersson, and L. Tilly, in *Defects in Semiconductors 17*, Materials Science Forum, Vol. 143 (Trans Tech Publications, 1993) pp. 809–814.

[82] M. S. S. K. Estreicher and J. Weber, in *Silicon, Germanium, and Their Alloys: Growth, Defects, Impurities, and Nanocrystals (Hardback)*, edited by G. Kissinger and S. Pizzini (CRC Press, 2014) Chap. 7.

[83] J. B. B. Bech Nielsen, K. Bonde Nielsen, Materials Science Forum **143-147**, 909 (1993).

[84] M. Budde, G. Lüpke, C. Parks Cheney, N. H. Tolk, and L. C. Feldman, Physical Review Letters **85**, 1452 (2000).

[85] K. B. Nielsen, L. Dobaczewski, S. Søgård, and B. B. Nielsen, Physical Review B **65**, 075205 (2002).

[86] I. Fan, K. H. Chow, B. Hitti, R. Scheuermann, W. A. MacFarlane, A. I. Mansour, B. E. Schultz, M. Egilmez, J. Jung, and R. L. Lichti, Physical Review B **77**, 035203 (2008).

[87] J. Corbett, S. Sahu, T. Shi, and L. Snyder, Physics Letters A **93**, 303 (1983).

[88] A. W. R. Leitch, V. Alex, and J. Weber, Physical Review Letters **81**, 421 (1998).

[89] M. Budde, B. Bech Nielsen, P. Leary, J. Goss, R. Jones, P. R. Briddon, S. Öberg, and S. J. Breuer, Physical Review B **57**, 4397 (1998).

[90] S. K. Estreicher, A. Docaj, M. B. Bebek, D. J. Backlund, and M. Stavola, physica status solidi (a) **209**, 1872 (2012).

[91] E. V. Lavrov and J. Weber, Physical Review Lett. **89**, 215501 (2002).

[92] S. J. Pearton, W. L. Hansen, E. E. Haller, and J. M. Kahn, Journal of Applied Physics **55**, 1221 (1984).

[93] R. Singh, S. J. Fonash, and A. Rohatgi, Applied Physics Letters **49**, 800 (1986).

[94] T. Sadoh, M. Watanabe, H. Nakashima, and T. Tsurushima, Journal of Applied Physics **75**, 3978 (1994).

[95] T. Sadoh, K. Tsukamoto, A. Baba, D. Bai, A. Kenjo, T. Tsurushima, H. Mori, and H. Nakashima, Journal of Applied Physics **82**, 3828 (1997).

[96] A. Liu, C. Sun, and D. Macdonald, Journal of Applied Physics **116**, 194902 (2014).

[97] T. Takahashi and M. Suezawa, Physica B: Condensed Matter **273–274**, 445 (1999).

[98] P. R. Briddon and M. J. Rayson, physica status solidi (b) **248**, 1309 (2011).

[99] G. Kresse and J. Hafner, Physical Review B **47**, 558 (1993).

[100] G. Kresse and J. Hafner, Physical Review B **49**, 14251 (1994).

[101] G. Kresse and J. Furthmüller, Physical Review B **54**, 11169 (1996).

[102] P. Giannozzi, S. Baroni, N. Bonini, M. Calandra, R. Car, C. Cavazzoni, D. Ceresoli, G. L. Chiarotti, M. Cococcioni, I. Dabo, A. D. Corso, S. de Gironcoli, S. Fabris, G. Fratesi, R. Gebauer, U. Gerstmann, C. Gougoussis, A. Kokalj, M. Lazzeri, L. Martin-Samos, N. Marzari, F. Mauri, R. Mazzarello, S. Paolini, A. Pasquarello, L. Paulatto, C. Sbraccia, S. Scandolo, G. Sclauzero, A. P. Seitsonen, A. Smogunov, P. Umari, and R. M. Wentzcovitch, Journal of Physics: Condensed Matter **21**, 395502 (2009).

Chapter 2

# Methods and approximations

## 2.1 The many-body problem

The current state-of-the-art electronic structure calculations aim at solving the Schrödinger equation for large sets of atomic particles, i.e., electrons and nucleons. Considering the atomic nuclei as single particles, the non-relativistic Schrödinger equation for a set of $N_\mathrm{e}$ electrons and $N_\mathrm{n}$ atomic nuclei in the absence of external fields is:

$$\hat{H}\Psi = E\Psi, \tag{2.1.1}$$

where $\hat{H}$ is the Hamiltonian operator for the system described by the wavefunction $\Psi$, which, in atomic units, can be written as:

$$\begin{aligned}\hat{H} &= \hat{T}_\mathrm{e} + \hat{T}_\mathrm{n} + \hat{\mathrm{V}}_\mathrm{e-e} + \hat{V}_\mathrm{n-n} + \hat{V}_\mathrm{n-e} \\ &= -\frac{1}{2}\sum_{i}^{N_\mathrm{e}} \boldsymbol{\nabla}_i^2 - \frac{1}{2}\sum_{\alpha}^{N_\mathrm{n}} \frac{1}{M_\alpha}\boldsymbol{\nabla}_\alpha^2 + \frac{1}{2}\sum_{i,j;i\neq j}^{N_\mathrm{e}} \frac{1}{|\mathbf{r}_i - \mathbf{r}_j|} \\ &+ \frac{1}{2}\sum_{\alpha,\beta;\alpha\neq\beta}^{N_\mathrm{n}} \frac{Z_\alpha Z_\beta}{|\mathbf{R}_\alpha - \mathbf{R}_\beta|} - \sum_{i,\alpha}^{N_\mathrm{e},N_\mathrm{n}} \frac{Z_\alpha}{|\mathbf{r}_i - \mathbf{R}_\alpha|},\end{aligned} \tag{2.1.2}$$

where $\hat{T}$ and $\hat{V}$ are the kinetic energy and Coulomb potential operators, $\mathbf{R}_\alpha$, $M_\alpha$ and $Z_\alpha$, are the position, mass and charge of the $\alpha$-th atomic nucleus, and $\mathbf{r}_i$ gives the coordinates of the $i$-th electron. Subscripts "n" and "e" stand for nuclei and electron related terms respectively. For this Hamiltonian, the total wavefunction of the system will be a function of the spatial coordinates of the $N_\mathrm{n}$ nuclei and $N_\mathrm{e}$ electrons.

Excluding the 2-body problems such as the hydrogen atom or the $He^+$ ion [1], there is no analytical solution for Eq. 2.1.2. The determination of a solution for a many-body problem should always require the use of approximations. Given the mass ratio between electrons and nuclei (electrons are ˜2000 times lighter) the first approximation is to assume that, in the reference frame of the electron interacting with an atomic nucleus, the nuclear particles are virtually static. Thus, any change in the spatial coordinates of the nuclei should be followed by an *instantaneous* response by the electron trajectories (or, in other words, an adiabatic response of the electron-only wavefunction). Based on this assumption Max Born and J. Robert Oppenheimer proposed [2] the separation of the system wavefunction into nuclear and electronic wavefunctions:

$$\Psi(\boldsymbol{r}, \mathbf{R}) = \psi_\mathbf{R}(\mathbf{r})\phi(\mathbf{R}), \tag{2.1.3}$$

where $\mathbf{r}$ and $\mathbf{R}$ represent the complete set of degrees of freedom (spatial coordinates and spin) of the electrons and atomic nuclei of the system, $\phi(\mathbf{R})$ is the nuclear wavefunction and $\psi_\mathbf{R}(\mathbf{r})$ is the electron wave unction, where the subscripted $\mathbf{R}$ means that $\psi$ depends parametrically on the nuclei coordinates. This allows us to reduce the electron-nuclear problem to an electron-only problem, where the electrons are under the influence of an external potential provided by the electrostatic interaction with the nuclei. The electron-only Hamiltonian $\hat{\mathcal{H}}$ becomes:

$$\begin{aligned}\hat{\mathcal{H}} &= \hat{\mathcal{T}}_\mathrm{e} + \hat{\mathcal{V}}_\mathrm{e-e} + \hat{\mathcal{V}}_\mathrm{n-e} = \\ &= -\frac{1}{2}\sum_{i}^{N_\mathrm{e}} \boldsymbol{\nabla}_i^2 + \frac{1}{2}\sum_{i,j;i\neq j}^{N_\mathrm{e}} \frac{1}{|\mathbf{r}_i - \mathbf{r}_j|} - \sum_{i,\alpha}^{N_\mathrm{e},N_\mathrm{n}} \frac{Z_\alpha}{|\mathbf{r}_i - \mathbf{R}_\alpha|}.\end{aligned} \tag{2.1.4}$$

This is referred to as the Born-Openheimer approximation. Now, having reduced the many-body problem to an electron-only problem with fixed nuclear parameters, we are still far from a methodology which is able to provide us with a description of the electronic structure of the systems of interest for this thesis. This is the point where density functional theory comes in. The following sections display a brief explanation of the basics behind the density functional theory and the several approximations in combination with DFT to obtain the many-electron solution of a system comprising hundreds or even thousands of electrons.

## 2.2 Density functional theory

In 1964, Hohemberg and Kohn proposed and demonstrated two theorems [3], telling us that the ground-state energy of a many-particle Hamiltonian is given exactly by a functional of the charge density, $E[n(\mathbf{r})]$, at the ground state of the system given by the wavefunction $\Psi_0(\mathbf{r})$, where the charge density $n(\mathbf{r})$ is defined as:

$$n(\mathbf{r}) = \int \Psi_0 \Psi_0^* \mathrm{d}\mathbf{r}, \tag{2.2.1}$$

### 2.2.1 Hohemberg and Kohn theorems

For a normalized and non-degenerate ground state $\Psi_0(\mathbf{r})$ in the absence of a magnetic field:

1. **Hohenberg-Kohn first theorem:** *The external potential is determined, within a trivial additive constant, by the charge density $n(\mathbf{r})$.*

2. **Hohenberg-Kohn second theorem:** *For a trial density $\tilde{n}(\mathbf{r})$, such that $\tilde{n}(\mathbf{r}) \geq 0$ and $\int \tilde{n}(\mathbf{r})dr = N$, the ground-state energy is:*

$$E_0 \leq E[\tilde{n}(\mathbf{r})]. \tag{2.2.2}$$

The second theorem is basically the application of the variational principle. Hence, by performing a full minimization of $E[n(\mathbf{r})]$ with respect to $n(\mathbf{r})$, we can obtain the exact value for the ground-state energy $E_0$ and the exact form of the ground-state electron density $n_0$. If the explicit form of $E[n(\mathbf{r})]$ is known, the exact solution for the ground-state charge density $n_0(\mathbf{r})$ can be determined. In the light of the Born-Openheimer approximation, the density functional theory is typically applied to electron-only systems that consider the nuclear coordinates to be fixed and thus, $n(\mathbf{r})$ will be from now on referred to as electron density instead of charge density.

### 2.2.2 Kohn-Sham equations

The total energy of a many-electron system $E[n(\mathbf{r})]$ under an external potential $v_0$ is a functional of the electron density $n(\mathbf{r})$, and is given by [4]:

$$E[n(\mathbf{r})] = T[n(\mathbf{r})] + V_{\mathrm{ee}}[n(\mathbf{r})] + \int d^3\mathbf{r} v_0(\mathbf{r}) n(\mathbf{r}), \tag{2.2.3}$$

where $T[n(\mathbf{r})]$ is the kinetic energy functional and $V_{\mathrm{ee}}[n(\mathbf{r})]$ is the functional that corresponds to the electrostatic potential resulting from the interaction between electrons. The explicit form of $E[n(\mathbf{r})]$ is unknown. However, we may consider an equivalent auxiliary system of

non-interactive electrons under an effective potential $v_s = v_s[n(\mathbf{r})]$. This system would be described by a set of independent one-electron Schrödinger equations. The one-electron equation correponding to the $l$-th electron orbital is given by [5]:

$$-\frac{1}{2}\nabla^2\psi_l + v_\mathrm{s}\psi_l = \epsilon_l\psi_l, \tag{2.2.4}$$

and the total density would be simply:

$$n(\mathbf{r}) = \sum_l^N \mid \psi_l(\mathbf{r}) \mid^2, \tag{2.2.5}$$

where $\psi_l = \psi_l(\mathbf{r})$ is a non-interacting electron orbital and $\epsilon_l$ is the corresponding eigenvalue. These are called Kohn-Sham orbitals. One must bear in mind that they have no true physical meaning, since they only describe this auxiliary non-interacting system. For this auxiliary system the total energy functional becomes:

$$E[n(\mathbf{r})] = T_\mathrm{s}[n(\mathbf{r})] + \int d^3\mathbf{r} v_0(\mathbf{r})n(\mathbf{r}) + E_\mathrm{H}[n(\mathbf{r})] + E_\mathrm{XC}[n(\mathbf{r})], \tag{2.2.6}$$

and the independent-electron kinetic energy becomes $T_\mathrm{s}[n(\mathbf{r})]$:

$$T_\mathrm{s}[n(\mathbf{r})] = -\sum_l^N \langle\psi_l \mid \frac{1}{2}\nabla^2 \mid \psi_l\rangle, \tag{2.2.7}$$

where $\mid \psi_l\rangle$ is the quantum state corresponding to the Kohn-Sham function $\psi_l(\mathbf{r})$, defined by the real space projection $\psi_l(\mathbf{r})$=$\langle\mathbf{r}\mid \psi_l\rangle$, and $\langle\psi_l \mid$ corresponds to its complex conjugate.
The two rightmost terms in Eq. 2.2.6, namely $E_\mathrm{H}[n(\mathbf{r})]$ and $E_\mathrm{XC}[n(\mathbf{r})]$ are the Hartree energy functional and exchange correlation energy functional respectively. While the Hartree energy can be expressed explicitly as:

$$E_\mathrm{H}[n(\mathbf{r})] = \frac{1}{2}\int\int d^3\mathbf{r}d^3\mathbf{r}'\frac{n(\mathbf{r})n(\mathbf{r}')}{|\mathbf{r}-\mathbf{r}'|}, \tag{2.2.8}$$

the exact form of $E_\mathrm{XC}$ is unknown. Several approximations are discussed in section 2.3.1. The effective external potential $v_\mathrm{s}$ will be the combination of the real external potential $v_0$ and the Hartree and Exchange and Correlation potentials, $v_\mathrm{H}$ and $v_\mathrm{XC}$ which are simply the variational derivative of $E_\mathrm{H}$ and $E_\mathrm{XC}$ with respect to the electron density, respectively:

$$v_\mathrm{s} = v_0 + v_\mathrm{XC} + v_\mathrm{H} = v_0 + \frac{\delta E_\mathrm{XC}}{\delta n} + \frac{1}{2}\int d^3\mathbf{r}'\frac{n(\mathbf{r}')}{|\mathbf{r}-\mathbf{r}'|} \tag{2.2.9}$$

The Equations 2.2.5 and 2.2.4 form a set of $N+1$ equations [5] that can be solved in a self-consistent cycle: we start with a trial electron density $n_\mathrm{trial}(r)$ and replace the corresponding potential on Eq. 2.2.4, which can be solved in order to obtain a set of eigenfunctions $\psi_l$ and eigenvalues $\epsilon_l$. From those eigenfunctions, a new electron density can be computed. This two-step process is repeated until the electron density does not change significantly between cycles. Once the final values of $n(\mathbf{r})$ and $\psi_l$ are obtained, we can solve Eq. 2.2.6 and determine the total energy of the many-electron system. The ground-state wavefunction $\Psi$ for the all-electron system can be described using a single determinant based on the Kohn-Sham orbitals:

$$\Psi = \frac{1}{\sqrt{N_e!}}\det[\psi_1(\mathbf{r})\psi_2(\mathbf{r})...\psi_{N_e}(\mathbf{r})]. \tag{2.2.10}$$

## 2.3 Approximations

### 2.3.1 Exchange and correlation functional

As it was mentioned in the previous Section, the exact form of the exchange-correlation functional $E_{\mathrm{XC}}$ is not known, and this is particularly problematic for heterogeneous systems. However, some approximations can be made. One important property of this functional is that it is non-local, *i.e.* it depends not only on the electron density at a given position $\mathbf{r}$, but also on the density away from that point. Thus, $E_{\mathrm{XC}}$ can be expanded in terms of $n(\mathbf{r})$ and all of its spatial derivatives. The most straightforward approximation is to assume that $E_{\mathrm{XC}}$ depends only on the local density. This approximation is called LDA (local density approximation), and for non-zero spin systems an analogous approximation called LSDA (local spin density approximation) [5–7] is available (densities for spin-up and spin-down electrons are considered separately). Another common approximation consists on a first-order expansion of $E_{\mathrm{XC}}$ over $n$ and $\boldsymbol{\nabla} n$ dependent terms, referred to as GGA (generalized gradient approximation) [8]. Nevertheless, these two approximations tend to have problems in estimating the band gap and relative position of levels, particularly in highly correlated systems. Further improvements are obtained with the application of hybrid exchange-correlation functionals [9], which admix a portion of exact non-local Fock exchange to the local or semi-local exchange. This method can give accurate estimates of band gaps of several semiconductor materials [10]. A specific GGA-based functional proposed by Perdew, Burke and Ernzerhof (PBE)[11] was employed for most of the work presented in this thesis.

Approximations such as the GGA do not account for self-interaction errors due to Coulomb interaction of the density with itself. This can be particularly severe within the localized electrons of the $d$ shells [12]. With these issues in mind we tested the DFT+$U$ approach [13], where a Hubbard-corrected semi-local density approximation term $U$ is introduced. On-site exchange effects are also added via a screened exchange parameter $J$ [14]. The results of the comparison between GGA+$U$ and pure GGA for early TMs are reported in Chapter 3. The on-site $U$ and $J$ parameters for each TM were calculated separately by means of a linear-response procedure as proposed by Cococcioni and co-workers [15].

### 2.3.2 Supercell Approximation

Given a perfect crystalline lattice, built from a unit cell defined by the unit vectors $\mathbf{a}_i$, the Bravais lattice points $\mathbf{l}_n$ are given by:

$$\mathbf{l}_n = \sum_i n_i \mathbf{a}_i \tag{2.3.1}$$

and the reciprocal lattice unit vectors $\mathbf{B}_i$ are defined as:

$$\mathbf{B}_i = 2\pi \frac{\mathbf{a}_j \times \mathbf{a}_k}{\mathbf{a}_i \cdot (\mathbf{a}_j \times \mathbf{a}_k)}. \tag{2.3.2}$$

A supercell can be obtained by means of a linear transformation $W$ that operates on the unit vectors $\mathbf{a}_i$:

$$\mathbf{A}_j = \sum_{i=1,3} W_{ij} \mathbf{a}_i. \tag{2.3.3}$$

where $W_{ij}$ are integer matrix elements that will define the size and shape of the supercell, and $\mathbf{A}_j$ are the vectors of the supercell with the respective lattice defined by $\mathbf{L_n} = \sum_i n_i \mathbf{A}_i$. Therefore, the volume of the supercell $V_{\mathrm{SC}}$ and the number of atoms in the supercell $N_a^{\mathrm{SC}}$ will be given by:

$$V = \det(W)\mathrm{v}_0; \tag{2.3.4}$$

$$N_{\mathrm{a}} = \det(W)n_{\mathrm{a}} \tag{2.3.5}$$

Where $\mathrm{v}_0$ and $n_{\mathrm{a}}$ are the volume and number of atoms of the unit cell.

The atomic positions $\mathbf{R}$ of the $N_a$ atoms of the supercell can be obtained from the atomic positions of the original cell $\mathbf{r}$:

$$\mathbf{R}_i^{\mathrm{SC}} = \mathbf{l}_n + \mathbf{r}_k, \text{ for } 1 \leq k \leq n_{\mathrm{a}} \text{ and } n \geq 1 \text{ such as } \mathbf{R}_i^{\mathrm{SC}} - \mathbf{R}_j^{\mathrm{SC}} \neq \mathbf{L}_m. \tag{2.3.6}$$

The condition $\mathbf{R}_i - \mathbf{R}_j \neq \mathbf{L}_m$ ensures that no two atomic positions, $\mathbf{R}_i$ and $\mathbf{R}_j$ may differ by a super-lattice vector $\mathbf{L}_m$.

The supercell method will generate a supercell $\det(W)$ times larger than the unit cell, with a Brillouin zone $\det(W)$ times smaller. Just like a unit cell, this supercell repeats itself periodically through space in order to model the crystalline material. Any defect introduced in the supercell will also repeat itself in space, creating images of the original defect. The choice of size and shape of the supercell is important to minimize any errors that may arise from coupling effects of the defect with its images.

### 2.3.3 Basis functions and core-state approximations

According to Felix Bloch's theorem, for a set of electrons bound to an infinitely repeating periodic potential (such as the case of a perfect crystal), there is a basis of electron wavefunctions $u_{\mathbf{k}i}(\mathbf{r})$ with the following properties:

- Each of these wavefunctions is an eigenstate
- Each of these wavefunctions can be written as follows:

$$u_{\mathbf{k}i}(\mathbf{r} + \mathbf{L_n}) = u_{\mathbf{k}i}(\mathbf{r})e^{\mathbf{ik}\cdot\mathbf{L_n}}, \tag{2.3.7}$$

where the $i$-th basis function $u_{\mathbf{k}i}(\mathbf{r})$ has the same periodicity of the potential (i.e. the same periodicity of the crystal lattice defined by the lattice vector $\mathbf{L}_n$) and has a Bloch wave vector $\mathbf{k}$. The Kohn-Sham orbitals $\psi_{\mathbf{k}l}$ can be then expanded in the $u_{\mathbf{k}i}$ basis as follows:

$$\psi_{\mathbf{k}l}(r) = \sum_i c_{\mathbf{k}li} u_{\mathbf{k}i}(\mathbf{r}), \tag{2.3.8}$$

where $c_{\mathbf{k}li}$ are the coefficients of the linear combination that results from the projection of $\psi_{\mathbf{k}l}$ in the $u_{\mathbf{k}i}$ basis. The speed and accuracy of the calculations will heavily depend on the choice of a good set of basis functions. Nevertheless, difficulties arise when it comes to describe the shape of the orbitals near the nucleus: in order to meet the orthogonality criterion, the orbitals will oscillate sharply in this region. As we move away from the nucleus, core-states will tend to zero, and the valence states are smoother. The description of these sharp oscillations would require the use of unpractically large basis-sets. The DFT codes employed in this work

take different approaches in establishing a Bloch basis and dealing with this issue: While the `AIMPRO` code (used in Chapter 4) employs Cartesian-Gaussian functions centered at the atomic coordinates with the application of the pseudopotential method [16], the `VASP` code (Chapters 3, 5 and 6) uses a plane-wave basis set in conjunction with the projected augmented method to account for core states [17].

### Cartesian-Gaussian functions (AIMPRO)

The Bloch basis built from a set Cartesian-Gaussian functions $\phi_i(\mathbf{r})$, centered at the atomic coordinates $\mathbf{R}_i$, across a lattice defined by $\mathbf{L}$ is given by:

$$u_{\mathbf{k}i}(\mathbf{r}) = \frac{1}{\sqrt{N_L}} \sum_{\mathbf{L}}^{N_L} \phi_i(\mathbf{r} - \mathbf{R}_i - \mathbf{L}) e^{\mathbf{i}\mathbf{k}\cdot\mathbf{L}} \tag{2.3.9}$$

$$\phi_i(\mathbf{r}) = (x - R_{ix})^{p1}(y - R_{iy})^{p2}(z - R_{iz})^{p3} e^{-\alpha_i(\mathbf{r}-\mathbf{R}_\alpha)^2} \tag{2.3.10}$$

Depending on the values of the exponents $p_j; j = 1, 2, 3$, the localized orbital $\phi_i(\mathbf{r})$ can be $s$-, $p$- or $d$-like for $\sum_j p_j$ =0, 1 or 2 respectively. The Gaussian component of $\phi_i(\mathbf{r})$ is parametrized by $\alpha_i$.

This basis allows for the evaluation of several quantities, including overlap integrals and can be made as to quickly vanish away from $\mathbf{R}_i$ [18]. However, this basis is non-orthogonal and can induce numerical instabilities.

### Pseudo-potentials (AIMPRO)

The pseudo-potential method is a way to describe the screening effective potential seen by valence electrons which is caused by the electrons in the core states. This approach allows us to remove the core-electron orbitals states from the problem and replace them with a pseudo-potential, leaving only the valence-electron eigenstates and respective energies to be determined.

This method makes use of two approximations:

1. *The frozen core approximation*: This approximation assumes that core electron wavefunctions remain unperturbed when the atom is transferred to different specific environments.

2. *Small core approximation*: It is assumed that the overlap between core-electron and valence-electron wavefunctions is negligible. Therefore, we can neglect exchange-correlation matrix elements that link core-electron and valence-electron states, allowing us to treat exchange correlation terms regarding core and valence electrons separately.

The pseudopotential approach comes with the drawback of the loss of the information on the full wavefunction close to the nuclei. In Chapter 4, Hartwigsen-Goedecker-Hutter pseudopotentials were employed [19].

### Plane-Wave functions (VASP)

In this case the Kohn-Sham states are simply projected into a plane-wave basis, over a set of reciprocal lattice vectors $\mathbf{G}$:

$$\psi_{\mathbf{k}l}(\mathbf{r}) = \frac{1}{\sqrt{\Omega}} \sum_{\mathbf{G},\mathbf{k}} C_{\mathbf{G}\mathbf{k}} e^{i(\mathbf{G}+\mathbf{k})\cdot\mathbf{r}}. \tag{2.3.11}$$

The size of the basis is limited as follows (in atomic units):

$$\frac{1}{2} |\mathbf{G} + \mathbf{k}|^2 < E_{\text{cut}}, \tag{2.3.12}$$

where $E_{\text{cut}}$ is the energy cut-off parameter for the plane-wave basis.

In the case of many solids (specially $s$ and $p$ metallic elements), where correlation effects are small enough and the free-electron picture is a good approximation, the use of a plane-wave basis is very efficient. However, the more localized the electron states, the larger the plane-wave basis required to describe them should be.

**Projected augmented wave method (VASP)**

The projected augmented wave (PAW) method [17] is a generalization of the pseudopotential method. This technique defines a set of pseudo-wave functions $\hat{\psi}_l(\mathbf{r})$ that are smooth in all the regions of space. This is accomplished by defining augmentation spheres with radius $R_{\text{PAW}}$ around the nuclei which is chosen so as to ensure that the augmentation sphere regions do not overlap. Outside the spheres, the pseudo-wave function is equal to the original Kohn-Sham wavefunction $\psi_l(\mathbf{r})$. Inside, a linear transformation $\hat{\mathcal{T}}$ that operates on $\hat{\psi}_l(\mathbf{r})$ and generates $\psi_l(\mathbf{r})$ is defined:

$$|\psi_l\rangle = \hat{\mathcal{T}}|\hat{\psi}_l\rangle. \tag{2.3.13}$$

$\hat{\mathcal{T}}$ should work as an identity operator outside the sphere delimited by $R_{\text{PAW}}$, and thus should be defined as:

$$\hat{\mathcal{T}} = 1 + \sum_{\alpha} \hat{\mathcal{T}}^{\alpha}, \tag{2.3.14}$$

where the $\alpha$ index corresponds to the $\alpha$-th atomic nuclei and $\hat{\mathcal{T}}^{\alpha}$ is an operator that is zero outside the augmentation spheres. Inside the spheres the pseudo-wave functions $|\hat{\psi}_l\rangle$ are expanded into computationally convenient partial waves $|\hat{\phi}_i^{\alpha}\rangle$ that can be mapped on a basis of the Kohn-Sham partial wavefunctions $|\phi_i^{\alpha}\rangle$ through the following relation:

$$|\phi_i^{\alpha}\rangle = (1 + \hat{\mathcal{T}}^{\alpha})|\hat{\phi}_i^{\alpha}\rangle \iff \hat{\mathcal{T}}^{\alpha}|\hat{\phi}_i^{\alpha}\rangle = |\phi_i^{\alpha}\rangle - |\hat{\phi}_i^{\alpha}\rangle. \tag{2.3.15}$$

To ensure that $\hat{\mathcal{T}}^{\alpha}$ elements outside the augmentation sphere are null, for $|\mathbf{r} - \mathbf{R}_{\alpha}| > R_{\text{PAW}}$, $\phi_i^{\alpha}(\mathbf{r})$ and $\hat{\phi}_i^{\alpha}(\mathbf{r})$ are set equal. The expansion of $|\hat{\psi}_l\rangle$ in terms of $|\hat{\phi}_i^{\alpha}\rangle$ is given by the following linear combination:

$$|\hat{\psi}_l\rangle = \sum_i P_{li}^{\alpha} |\hat{\phi}_i^{\alpha}\rangle, \tag{2.3.16}$$

where the expansion coefficients $P_{li}^{\alpha}$ must be linear functionals of $|\hat{\psi}_l\rangle$, meaning that they can be obtained by projecting $|\hat{\psi}_l\rangle$ in a basis of projector functions $\langle\hat{p}_i^{\alpha}|$.

$$P_{li}^{\alpha} = \langle\hat{p}_i^{\alpha}|\,\hat{\psi}_l\rangle. \tag{2.3.17}$$

These projector functions obey the following two conditions:

$$\sum_i \left|\hat{\phi}_i^\alpha\right\rangle\left\langle\hat{p}_i^\alpha\right| = 1; \tag{2.3.18}$$

$$\left\langle\hat{p}_i^\alpha\middle|\hat{\phi}_i^\alpha\right\rangle = \delta_{i,j}. \tag{2.3.19}$$

Given a known set of projector functions $\left\langle\hat{p}_i^\alpha\right|$ , pseudo partial waves $\left|\hat{\phi}_i^\alpha\right\rangle$ and partial waves $|\phi_i^\alpha\rangle$ that meet these conditions, the operator $\hat{\mathcal{T}}$ can then be built. From equations 2.3.14, 2.3.15 and 2.3.18 we obtain:

$$\hat{\mathcal{T}} = 1 + \sum_\alpha \sum_i (|\phi_i^\alpha\rangle - \left|\hat{\phi}_i^\alpha\right\rangle)\left\langle\hat{p}_i^\alpha\right| \tag{2.3.20}$$

These sets of projector functions and partial waves are typically chosen so the Kohn-Sham partial waves $|\phi_i^\alpha\rangle$ are solutions to the Kohn-Sham Schrödinger equation for one isolated atom. The pseudo-wave functions $\left|\hat{\psi}_l\right\rangle$ are obtained as solutions of the pseudo Kohn-Sham equations with eigenvalues $\hat{\epsilon}_l$:

$$\hat{\mathcal{T}}^\dagger \widehat{H} \hat{\mathcal{T}} \left|\hat{\psi}_l\right\rangle = \hat{\epsilon}_l \left|\hat{\psi}_l\right\rangle, \tag{2.3.21}$$

And the expected value of a given local operator $\widehat{O}$ becomes:

$$\left\langle\widehat{O}\right\rangle = \left\langle\hat{\psi}_l\middle|\hat{\mathcal{T}}^\dagger \widehat{O} \hat{\mathcal{T}}\middle|\hat{\psi}_l\right\rangle \tag{2.3.22}$$

The projected augmented wave method is also used in conjunction with the frozen-core approximation, keeping the core orbitals constant in the process of electronic relaxation. However, unlike the pseudopotential method these core orbitals are not removed from the all-electron problem, and the issue of the sharp oscillation manifested by the Kohn-Sham orbital solutions near the atomic nucleus is dealt by means of a linear transformation to a set of smooth orbitals that are more convenient to work with in a computer.

### 2.3.4 Brillouin-Zone sampling

Many of the integrals in electronic structure calculations for periodic systems are performed in the reciprocal space over the Brillouin zone. Usually, these integrals cannot be evaluated analytically and, therefore, are discretized into weighted sums over a grid of **k**-points in the reciprocal lattice. The average value $\bar{f}$ of a given integrand function $f(\mathbf{k})$ over the Brillouin-Zone with volume $\Omega_{\mathrm{BZ}}$ can be approximated as follows:

$$\bar{f} = \frac{\Omega_{\mathrm{BZ}}}{(2\pi)^3} \int_{BZ} f(\mathbf{k}) d\mathbf{k} \approx \frac{1}{N} \sum_i^N w_i f(\mathbf{k}_i), \tag{2.3.23}$$

where $\mathbf{k}_i$ is the $i$-th special **k**-point from a grid of $N$ special **k**-points used to approximate the Brillouin zone and $w_i$ is a weighting factor.

In our calculations we applied the method proposed by Monkhorst and Pack [20] to define the **k**-points and their weights. The first step consists in defining a grid $\mathbf{k}(i,j,k)$, in the first Brillouin zone:

$$\mathbf{k}(i,j,k) = u_i \mathbf{b}_1 + u_j \mathbf{b}_2 + u_k \mathbf{b}_3, \tag{2.3.24}$$

where $\mathbf{b}_i, i = 1, 2, 3$ are the primitive reciprocal lattice vectors and the coefficients $u_i$, $u_j$ and $u_k$ are defined as follows:

$$u_i = (2i - I - 1)/2I \qquad (i = 1, ...I) \tag{2.3.25}$$
$$u_j = (2j - J - 1)/2J \qquad (j = 1, ...J) \tag{2.3.26}$$
$$u_k = (2k - K - 1)/2K \qquad (k = 1, ...K), \tag{2.3.27}$$

with $I, J, K$ being integers larger or equal to 1, defining the size of the grid.

Then, we take into consideration the point-groups for the Wigner-Seitz cell, Brillouin-zone and Crystal, labeled as $F$, $G$ and $H$, with orders $g_F$, $g_G$ and $g_H$. To each of the $\mathbf{k}(i, j, k)$ we apply the symmetry operations of the point group $F$ to generate a full star. Then we fold each star by using the symmetry operations of $G$ (note that $G$ is contained in $F$) to obtain a set of irreducible $\mathbf{k}$-points. The weight $w_\mathbf{k}$ of each one of these irreducible $\mathbf{k}$-points is given by:

$$w_k = g_G/g_\mathbf{k}, \tag{2.3.28}$$

where $g_\mathbf{k}$ is the order of the site symmetry of that specific $\mathbf{k}$-point within the Brillouin Zone.

## 2.4 Calculation of defect properties

### 2.4.1 Defect structure

Once the Kohn-Sham equations are solved, we are able to determine the electron density $n(\mathbf{r})$ and total energy $E_{\mathrm{TOT}} = E[n(\mathbf{r})]$ of a system with fixed atomic positions. However, for most of the situations, the equilibrium atomic positions of the system are unknown. The equilibrium configurations of the system correspond to local minima of the total energy with respect to all atomic coordinates. The search for these local minima can be done with several algorithms such as quasi-Newton-Raphson type algorithms [21] or the conjugate gradient technique [22]. In this work we applied the conjugated gradient minimization method for most situations. The process consists on determining the forces acting on each atom $\mathbf{F}_\alpha$, which can be obtained from the gradient of the total energy of the system with respect to the spatial coordinates of each atom:

$$\mathbf{F}_\alpha = -\nabla_\alpha E_{\mathrm{TOT}} \tag{2.4.1}$$

This gradient can be determined with the application of the Hellman-Feynman theorem [23]: In Hilbert space, if a given Hamiltonian $\hat{\mathrm{H}}$ depends on a parameter $\lambda$, and the respective expectable value of the derivative $\frac{\partial E}{\partial \lambda}$ at the state $\psi$ can be defined as:

$$\frac{\partial E}{\partial \lambda} = \left\langle \psi \left| \frac{\partial \widehat{H}}{\partial \lambda} \right| \psi \right\rangle \tag{2.4.2}$$

Once the forces are known, the atom positions are changed according to the forces applied on them. This process is iterated until all vectorial components of the forces applied on each atom are under a previously defined threshold value (and the total energy difference between iterations is under a pre-defined convergence criterion). For a given component $m = x; y; z$ of the force $F^n_{m,\alpha}$ applied on the atom $\alpha$ at the iteration $n$, the coordinates of the new atomic position $R^n_{m,\alpha}$ of the atom $\alpha$ will be given by:

$$R^n_{m,\alpha} = R^n_{m,\alpha} + w d^n_{\alpha,m}, \tag{2.4.3}$$

where $w$ is a scaling parameter and $d^n_{\alpha,m}$ is given by:

$$d^n_{m,\alpha} = F_{m,\alpha} - \kappa^n_{m,\alpha} d^{n-1}_{m,\alpha} \tag{2.4.4}$$

with

$$\kappa^n_{m,\alpha} = \frac{\sum_{m,\alpha} F^n_{m,\alpha}(F^n_{m,\alpha} - F^{n-1}_{m,\alpha})}{\sum_{m,\alpha}(F^{n-1}_{m,\alpha})^2} \tag{2.4.5}$$

### 2.4.2 Migration barriers - nudged elastic band method

The nudged elastic band (NEB) method [24] is applied to determine saddle points of reconfiguration reaction paths between two stationary states. For instance, this method can be applied in the determination of migration barriers of defects in crystalline materials. The method is based on a chain of *images* that constitute a discrete representation of the reconfiguration path, with each image corresponding to an intermediary configuration of the defective supercell. These images are linked by a virtual elastic band that prevents them to collapse against each other or to return to the ground state. The effective force $\mathbf{F}^{\mathrm{NEB}}_{\alpha,i}$ acting on each atom $\alpha$ of a given image $i$ will take into account the elastic band force $\mathbf{F}^{/\!/}{}_{\alpha,i}$ for that image, and is given by:

$$\mathbf{F}^{\mathrm{NEB}}_{\alpha,i} = \mathbf{F}^{\perp}{}_{\alpha,i} + \mathbf{F}^{/\!/}{}_{\alpha,i}, \tag{2.4.6}$$

where $\mathbf{F}^{\perp}{}_{\alpha,i}$ are obtained projecting the real forces $\mathbf{F}_{\alpha,i}$, determined through the method presented in the previous subsection (see Eq. 2.4.1), for the image $i$, in the directions that are orthogonal to the elastic band:

$$\mathbf{F}^{\perp}{}_{\alpha,i} = \mathbf{F}_{\alpha,i} - \left(\mathbf{F}_{\alpha,i}.\mathbf{e}^{/\!/}_{\alpha,i}\right)\mathbf{e}^{/\!/}_{\alpha,i}. \tag{2.4.7}$$

The unitary vector $\mathbf{e}^{/\!/}_{\alpha,i}$ gives us the direction of the elastic band force, that separates the current image $i$ from the previous image $i-1$ and the next image $i+1$:

$$\mathbf{e}^{/\!/}{}_{\alpha,i} = \frac{\mathbf{v}^{/\!/}_{\alpha,i}}{\| \mathbf{v}^{/\!/}_{\alpha,i} \|}, \tag{2.4.8}$$

with:

$$\mathbf{v}^{/\!/}_{\alpha,i} = \frac{\mathbf{R}_{\alpha,i} - \mathbf{R}_{\alpha,i-1}}{\| \mathbf{R}_{\alpha,i} - \mathbf{R}_{\alpha,i-1} \|} + \frac{\mathbf{R}_{\alpha,i+1} - \mathbf{R}_{\alpha,i}}{\| \mathbf{R}_{\alpha,i+1} - \mathbf{R}_{\alpha,i} \|}. \tag{2.4.9}$$

The elastic band force $\mathbf{F}^{/\!/}{}_{\alpha,i}$ has the same direction as $\mathbf{e}^{/\!/}_{\alpha,i}$ and comes as:

$$\mathbf{F}^{/\!/}{}_{\alpha,i} = [k(\| \mathbf{R}_{\alpha,i+1} - \mathbf{R}_{\alpha,i} \| - \| \mathbf{R}_{\alpha,i} - \mathbf{R}_{\alpha,i-1} \|).\mathbf{e}^{/\!/}_{\alpha,i}]\mathbf{e}^{/\!/}_{\alpha,i}, \tag{2.4.10}$$

Where $k$ is the elastic constant of the band. The condition presented in Eq. 2.4.6 is applied in the relaxation algorithm, assuring that each image finds its lowest possible energy while maintaining equal spacing to neighboring images. The image with highest energy will be the closest representation of the saddle point. The energy difference between the saddle point and the starting image gives us the energy barrier associated to the reaction path.

### 2.4.3 Electrical levels - the marker method

The transition energy between two consecutive charge states (also called electrical level) of a defect is an observable that can be predicted with the aid of DFT *ab-initio* codes, and it is easily compared to experimental data, more specifically, with deep level transient spectroscopy (DLTS) or optical measurements. Nevertheless, there are some errors associated to the calculations that must be taken into account. There are two main sources of error: defect-image interactions in supercell calculations or self-interaction errors not accounted for by the exchange-correlation approximations applied. There are several approaches that can be used to avoid or minimize these errors. In this work in particular we apply the *marker* approach [25], which involves using a defect whose electrical levels are well established experimentally as a benchmark for our calculations. The marker method basically assumes that, for two consecutive charge states $q$ and $q+1$, the off-set between ionization potentials for the defect under scrutiny $I_{\mathrm{d}}(q/q+1)$ and the marker defect $I_{\mathrm{m}}(q/q+1)$ is approximately same as the off-set between the respective electrical levels $E_{\mathrm{d}}(q/q+1)$ and $E(q/q+1)$, i.e.

$$I_{\mathrm{d}}(q/q+1) - I_{\mathrm{m}}(q/q+1) \approx E_{\mathrm{d}}(q/q+1) - E_{\mathrm{m}}(q/q+1), \tag{2.4.11}$$

Then, the electrical level of the defect under scrutiny simply becomes:

$$E_{\mathrm{d}}(q/q+1) \approx I_{\mathrm{d}}(q/q+1) - I_{\mathrm{m}}(q/q+1) + E_{\mathrm{m}}(q/q+1), \tag{2.4.12}$$

The accuracy of this approximation is deeply related to the degree of similarity between shapes and localization between the acceptor (or donor) states of both defects. If the defect under scrutiny and the marker defect produce states in the gap that are similar enough, the errors in the calculations will practically cancel each other in 2.4.12 . We also must ensure that the calculations are made in the same conditions (supercell size, basis functions, pseudopotentials/PAW basis, **k**-point grids, and so on). Since the value of the transition energy $E_m(q/q+1)$ is known from experiments, we just have to calculate the ionization potentials $I_d(q/q+1)$ and $I_m(q/q+1)$. Ionization energies are simply obtained as:

$$I_{\mathrm{d}}(q/q+1) = \tilde{E}_{\mathrm{d}}[q, \mathbf{R}_q] - \tilde{E}_{\mathrm{d}}[q+1, \mathbf{R}_{q+1}] \tag{2.4.13}$$

where $\tilde{E}_{\mathrm{d}}[q, \mathbf{R}_q]$ is the calculated total energy of a supercell hosting a defect with configuration $\mathbf{R}_q$ for the charge state $q$. An analogous reasoning is applied for the electron affinities $A(q-1/q)$. For negative charge states, these calculations are performed by adding electrons to the lowest unoccupied Kohn-Sham level and placing a uniformly positively charged background *jellium* ensuring the charge neutrality of the supercell for negative charge states. (For positive charge states we remove electrons from the highest occupied Kohn-Sham level and apply a negative background charge). In some particular cases, it is convenient to use the bulk material itself as a benchmark (marker). In that case $E_{\mathrm{m}}(q/q+1)$ is replaced by the energy of the conduction band bottom ($E_{\mathrm{c}}$) or valence band top ($E_{\mathrm{v}}$) for $q<0$ or $q \geq 0$ respectively. This removes the experimental input from the method, however in this case one must take into account the errors coming from long range defect-image interactions. These errors can be minimized with the use of charge corrections. With the exception of Chapter 3, where a first-order Madlung correction was applied, we adopted the method proposed by Freysoldt, Neugebauer and Van de Walle [26]. This method approximates the total energy of an *infinite* crystal hosting a defect with charge $q$ and corresponding ground-state configuration $\mathbf{R}_q$, $E_{\mathrm{d}}[q, \mathbf{R}_q]$ as:

$$E_{\mathrm{d}}[q, \mathbf{R}_q] \approx \tilde{E}_d(q, \mathbf{R}_q) + E_{\mathrm{d,corr}}(q, \mathbf{R}_q), \tag{2.4.14}$$

where $E_{\mathrm{d,corr}}(q, \mathbf{R}_q)$ is the charge correction. For cubic materials (which is the case of every problem addressed in this thesis) this correction is given by:

$$E_{\mathrm{d,corr}}(q, \mathbf{R}_q) = \frac{\alpha_{\mathrm{M}} q^2}{2\epsilon L} - q\Delta\bar{\phi}_{\mathrm{PC,ind}}(q, \mathbf{R}_q). \tag{2.4.15}$$

The term $\alpha_{\mathrm{M}} q^2/2\epsilon L$, corresponds to the first order Madlung correction, where $\alpha_{\mathrm{M}}$ is the Madlung constant for the geometry of the system, $\epsilon$ is the dielectric constant of the material and $L$ is the supercell lattice parameter. In the second term of the correction, $\Delta\bar{\phi}_{\mathrm{PC,ind}}(q, \mathbf{R}_q)$ is defined as the offset between the induced average potentials of the defect $\bar{\phi}_{\mathrm{ind}}(q, \mathbf{R}_q) = \bar{\phi}_{\mathrm{d}}(q, \mathbf{R}_q) - \bar{\phi}_{\mathrm{bulk}}$ and of a point charge $\bar{\phi}_{\mathrm{PC}}(q)$:

$$\Delta\bar{\phi}_{\mathrm{PC,ind}}(q, \mathbf{R}_q) = \bar{\phi}_{\mathrm{ind}}(q) - \bar{\phi}_{\mathrm{PC}}(q, \mathbf{R}_q). \tag{2.4.16}$$

These space-averaged potentials are obtained from the Hartree potential of the pristine and defective supercells. This average is computed in the region of space outside of the largest sphere that can be inscribed by the Wigner-Seitz supercell, far from the defect. For the calculation of electrical levels, the corrected values $E_{\mathrm{d,corr}}(q, \mathbf{R}_q)$ can replace the uncorrected total energies of the defective supercells $\tilde{E}_{\mathrm{d}}[q, \mathbf{R}_q]$ in Eq. 2.4.13.

### 2.4.4 Electrical levels - experimental techniques

#### Deep level transient spectroscopy (DLTS)

Similarly to the other two techniques presented below, the main idea of standard DLTS [27] is to measure the transient capacitance in the depletion region of a p-n junction or a Shotky junction diode, in reverse-bias, as a response to a certain stimulus. In the case of DLTS the stimulus is a voltage pulse. The voltage pulse switches the bias in the depletion region, allowing charge carriers to fill the defect levels that exist in that region and resulting in the sudden change of the capacitance. This pulse is typically referred to as filling pulse. The rates $e_{\mathrm{n,p}}$ at which the defects emit back the charge carriers (n for electrons and p for holes) after the pulse depends on the temperature T as follows:

$$e_{\mathrm{n,p}} = \frac{N_{\mathrm{n,p}}\, c_{\mathrm{n,p}}}{g} \exp\left(-\frac{E_{\mathrm{A}}}{k_{\mathrm{B}} T}\right), \tag{2.4.17}$$

where $\mathrm{N_{n,p}}$ is the density of states at the conduction/valence band edges (for electron or hole emission respectively), $g$ is the degeneracy factor of the level, $c_{\mathrm{n,p}}$ is a pre-factor specific to the defect level and $E_{\mathrm{A}}$ is the activation barrier for the charge emission process. The time constant for this process $\tau$ is defined as $1/e_{\mathrm{n,p}}$. As a result of this emission, the capacitance restores its value prior to the pulse at a rate $e_{\mathrm{n,p}}$. The DLTS technique repeats this process of introducing a filling pulse followed by the thermal emission of charge carriers for a wide range of temperatures, resulting in multiple emission rates corresponding to each temperature. After a given filling pulse, the capacitance in the depletion region of the junction is measured in two different instants $t_1$ and $t_2$. The DLTS spectra corresponds to the difference $\Delta$C between the capacitance measured at $t_2$ and at $t_1$. If the emission rate is too fast (high temperatures), the original capacitance in the depletion region will be recovered even before $t_1$, and there will be no measured variance of capacitance i.e. $\Delta\mathrm{C} = 0$. At low temperatures the defect levels

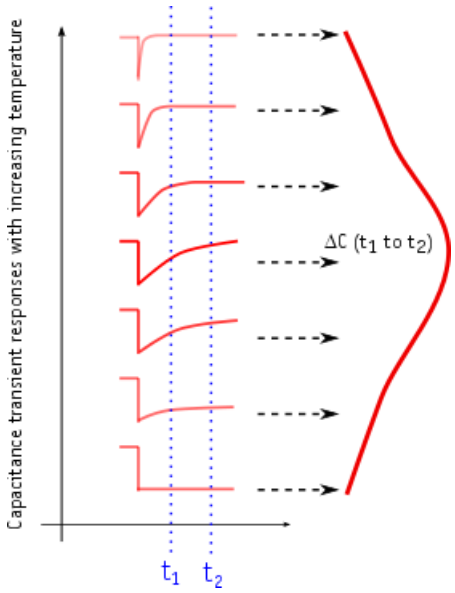


Figure 2.4.1: Schematic representation of a DLTS measurement. On the left side, the horizontal axis corresponds to time, while the vertical axis represents temperature. Different emission rates are corresponding to different temperatures are illustrated in the y-axis. On the right side the resulting signal is represented. An example of a DLTS spectra can be seen in chapter 6, Fig. 6.3.1

will emit charge carriers at such a slow rate that the capacitance will remain nearly constant after the filling pulse. When the emission rates match the rate window defined by $t_1$ and $t_2$, that is:

$$\tau = (t_2 - t_1)/\ln(t_2/t_1), \tag{2.4.18}$$

the value of $\Delta$C is maximized and a DLTS peak is observed. These measurements are averaged over multiple cycles of the measurement, allowing to obtain the activation energy of the emission. This activation energy corresponds to the position of the level in the band-gap in relation to the conduction band (electrons) or valence band (holes). The temperature scan process is illustrated in Fig. 2.4.1.

### Laplace DLTS

In some situations, the standard DLTS technique might not be able to resolve emission rates that are due to carrier traps with close activation energies for emission, or when there is superimposed noise. The goal of Laplace DLTS (LDLTS) [28] is to, at a specific temperature, measure the capacitance transient response signal, and decompose it by means of an inverse Laplace transformation. The principle is analogous to the decomposition of a periodic signal in multiple sinusoidal frequencies by means of a Fourier transformation. In this case the capacitance signal is decomposed into multiple exponential components. However, the number of exponential components can be chosen and must be adequate so the resulting spectral decomposition has a physical meaning. This choice must be done with knowledge of the existing signal-to-noise ratio and also in light of previous DLTS measurements. The resulting spectra provides higher resolution between different emission rates when compared to the standard DLTS signal.

**Minority carrier transient spectroscopy (MCTS)**

DLTS techniques provide information on the capture and emission of majority carriers, by means of a voltage pulse. However, it is also useful to obtain information on the minority carrier trapping process. In this situation, the perturbation of the depletion region of the junction can be either done by injection of minority carriers (p-n junction) with the introduction of forward bias, or with the use of optical excitation [29]. Minority carrier transient spectroscopy (MCTS) techniques typically use the latter method, with the application optical signals with a wavelength corresponding to an energy slightly larger than the band gap, generating both majority and minority carriers. The illumination source can be at the front or at the backside of the sample. Illumination from the backside comes with the advantage that majority carriers are rejected by the depletion field, and, if in the case of indirect gap semiconductors like silicon (no light absorption in the depletion region) the carrier flux will be exclusively due to minority carriers. This is a transient capacitance technique just like DLTS and the spectrum is obtained similarly, typically represented with negative amplitudes (see example of a MCTS spectrum in Chapter 6, Fig. 6.3.1).

### 2.4.5 Formation Energies

The free energy of formation required to introduce a defect in a crystalline structure is given by:

$$G_f = E - \sum_i N_i \mu_i + PV - TS \tag{2.4.19}$$

where $E$ is the internal energy of the crystal that hosts the defect, containing $N_i$ elements of species $i$ with chemical potential $\mu_i$. The remaining terms stand for the thermodynamic variables of the system: Pressure ($P$), Volume ($V$), Temperature ($T$) and Entropy ($S$) While the $PV$ term is usually negligible, the $TS$ term is often not considered in DFT calculations due to the fact that entropy calculations would bring huge computational costs, and there are larger sources of error introduced by the approximations mentioned in this chapter. The $\sum_i N_i \mu_i$ term includes both atomic species and electrons. In a solid, the fermi level $E_{\mathrm{F}}$ can be defined as a thermodynamic work required to add one electron to the system. In this specific situation, the fermi level is equivalent to the electron chemical potential. Thus, the free energy of formation for a charged defect becomes:

$$G_f = E(\mathbf{R}, q) - \sum_i N_i \mu_i + q(E_{\mathrm{F}} + E_{\mathrm{v}}), \tag{2.4.20}$$

Where $E_{\mathrm{F}}$ corresponds to the position of the fermi level with respect to the top of the valence band $E_{\mathrm{v}}$. The total energy of the defective crystal $E(\mathbf{R}, q)$ corresponds to a specific structural configuration defined by atomic coordinates $\mathbf{R}$ and charge state $q$. In the particular case of DFT calculations within the supercell approximation $E(\mathbf{R}, q)$ is defined as the total energy of the supercell including $N_i$ atoms of each species. The chemical potential $\mu_i$ of a given species $i$ is typically obtained from the energy of a standard thermodynamic state for that species. For instance, to obtain the chemical potential of hydrogen we can consider the $H_2$ molecule, find the equilibrium bond-length using the conjugate gradient technique, and determine the total energy of the molecule. The calculated chemical potential of hydrogen will be simply $\mu_{\mathrm{H}} = E_{\mathrm{TOT}}(\mathrm{H}_2)/2$. In the case of silicon, the total energy of the pristine supercell can be taken in order to determine $\mu_{\mathrm{Si}}$, whereas in the case of transition metals one can use the stable phases of metal-silicides. In some situations it is convenient to use the ground-state energy

of certain impurities in a silicon crystal environment to obtain the chemical potential of that species. In Chapter 4 we use the ground state of titanium interstitial in silicon to define the chemical potential of titanium. Thus, the formation energies presented in Fig. 4.2.1 were determined with respect to the formation energy of the neutral titanium interstitial.

According to Eq. 2.4.20 the formation energy of defects in the neutral charge state will not depend on the fermi level. However, the formation energy of defects with $q \neq 0$ will depend linearly on the position of $E_{\mathrm{F}}$ in the gap. When the Fermi level coincides with the transition level between two charged states, defects on both charge states have equal probability to show up in the sample. For instance, in the case of a defect with an acceptor level when $E_F = E\,(-/0)$, we have:

$$G_f[q=0] = G_f[q=-1; E_F = E\,(-/0)]. \tag{2.4.21}$$

From eqs. 2.4.20 and 2.4.21 we obtain:

$$G_f[q=-1; E_{\mathrm{F}}] = G_f[q=0] + E\,(-/0) - (E_{\mathrm{F}} + E_{\mathrm{v}}). \tag{2.4.22}$$

This means that knowing the formation energy of the neutrally charged defect and the position of the electrical levels that dictate the transition from the neutral state to charged states we can determine the formation energies of these charged states. Equation 2.4.22 can be generalized for any charge state, with $q < 0$:

$$G_f[q<0; E_{\mathrm{F}}] = G_f[q=0] + \sum_{\rho=q+1}^{\rho=0} E(\rho - 1/\rho) + q(E_{\mathrm{F}} + E_{\mathrm{v}}), \tag{2.4.23}$$

and for $q > 0$:

$$G_f[q>0; E_{\mathrm{F}}] = G_f[q=0] - \sum_{\rho=0}^{\rho=q-1} E(\rho/\rho + 1) + q(E_{\mathrm{F}} + E_{\mathrm{v}}) \tag{2.4.24}$$

where $E(\rho - 1/\rho)$ and $E(\rho - 1/\rho)$ correspond to the transition levels calculated with the marker method.

### 2.4.6 Localized Vibrational Modes

Normal vibrational modes with frequencies above the Raman frequency of the material and localized around defects are denominated as local vibrational modes (LVM's). The LVM's and their respective frequencies can be determined accurately with the aid of DFT based methods. Here, the total energy $E$ of a $N$ atom system is expanded to the second order, relatively to the atomic displacements (assuming the harmonic approximation) [30]:

$$E = E_0 + \frac{1}{2}\sum_{i,j}^{N} \mathbf{u}_i \cdot K(i,j) \cdot \mathbf{u}_j, \tag{2.4.25}$$

where $E_0$ is the static total energy, $u_i$ is the displacement of the atom $i$. $K(i,j)$ is a rank 2 tensor, whose elements $K_{ab}(i,j)$ are usually referred to as force constants, and are given by:

$$K_{ab}(i,j) = \frac{\partial^2 E}{\partial u_{i,a} \partial u_{j,b}} \tag{2.4.26}$$

where the indexes $a$ and $b$ stand for any of the three Cartesian coordinates. It is possible to obtain all the matrix elements $K_{ab}(i,j)$ by evaluating second derivatives in Eq. 2.4.26 numerically.

For an atom $i$ with mass $M_i$ the equation of motion will be:

$$M_i \frac{\partial^2 \mathbf{u}_i}{\partial^2 t} = -\nabla_i E = -\sum_j^N K(i,j) \cdot \mathbf{u}_j. \tag{2.4.27}$$

Assuming an oscillatory solution for $u_i$ as a function of time $u_i = u_i(t)$, we transform the set of equations of motion for all the $N$ atoms into an eigenvalue problem:

$$\mathrm{D} \cdot \mathbf{U} = \omega^2 \mathbf{U}, \tag{2.4.28}$$

where D is the $3N \times 3N$ dynamical matrix whose elements are given by:

$$D_{ab}(i,j) = \frac{1}{\sqrt{M_i M_j}} K_{ab}(i,j). \tag{2.4.29}$$

The eigenvalues $\omega^2$ and eigenvectors $\mathbf{U}$ in of the dynamical matrix correspond to the squared frequencies and displacement vectors for the local vibrational modes of the $N$ atom system. Knowing $\mathbf{U}$ and $\omega^2$ , one can determine the modes that are allowed by the selection rules in infra-red or Raman spectroscopy, by establishing which representations of the symmetry group of the defect correspond to the displacement of the atomic positions of the defect.

In order to determine localized vibrational modes related to a specific point defect, it is a common procedure to limit the dynamical matrix size to a local set of $N$ atoms around the defect under scrutiny, since only these atoms will have considerable displacement amplitudes. The next subsection is a brief introduction of the Fourier transform infrared spectroscopy technique, applied to detect localized vibrational modes.

### 2.4.7 Fourier transform infrared spectroscopy (FTIR)

#### Selection rule for infrared spectroscopy

The energy range of separation between vibrational states typically corresponds to the infrared (IR) region of the electromagnetic spectrum. For a local vibrational mode to be observed by means of infrared absorption the dipole moment of the system $\boldsymbol{\mu}$ must vary with respect to the change in atomic positions that correspond to that LVM, that is:

$$\frac{d\boldsymbol{\mu}}{d\mathbf{R}} \neq 0. \tag{2.4.30}$$

The dipole moment $\boldsymbol{\mu}$ is defined from a set of charges $q_i$ located at coordinates $\mathbf{R}_i$:

$$\boldsymbol{\mu} = \sum_i q_i \mathbf{R}_i \tag{2.4.31}$$

For instance, in the case of the $CO_2$ molecule, the two oxygen atoms are more electronegative, attracting more negative charge to their positions (see Fig. 2.4.2). While the symmetric stretch mode will correspond to no changes in the dipole moment ($\boldsymbol{\mu}$ is always zero), in the case of anti-symmetric stretch, the difference in length between the two opposing C-O bonds is changing, resulting in a variation of the global dipole moment of the molecule. The

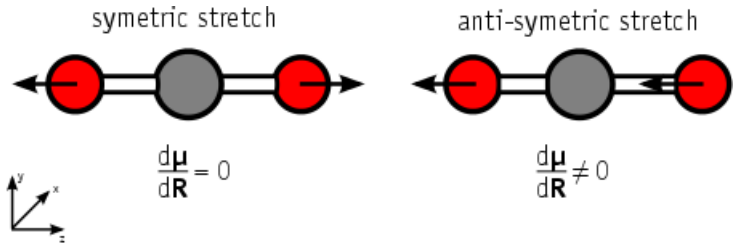


Figure 2.4.2: The symmetric anti-symmetric stretch modes of the $CO_2$ molecule

anti-symmetric stretch mode of the $CO_2$ molecule breaks some of the static molecule original symmetry: the mode is anti-symmetric with respect to the inversion operation centered at the carbon atom, to all the $S_\infty$ improper rotation axis, and to the $C_2$ rotation axis. For the $CO_2$ molecule symmetry group, $D_{\infty h}$, and considering the molecule axis is parallel to the cartesian $z$ axis, this mode corresponds to an irreducible representation that transforms in the same way as linear function of the type $f(x, y, z) = z$ which is odd (or anti-symmetric) with respect to the $xy$ plane. In the general case, a vibrational mode is IR active when the respective irreducible representation of the symmetry group of the molecule or defect transforms like a linear function upon application of the symmetry operations of that group.

**The FTIR technique**

The goal of Fourier-transform infra-red (FTIR) absorption is to obtain the response of a sample to a broad band of frequencies [31]. This is typically attained with the use of a Michelson interferometer that splits the incident collimated polychromatic beam in two and continually changes the optical path of one of the split beams with respect to the other, resulting in successive cycles of constructive and destructive interference when the split beams merge back and inside in the sample. This change in optical path is provided by a moving mirror (see Fig.2.4.3). The recombined beam will then illuminate with the sample, resulting in a modified IR beam that is then converted to an electrical signal by the detector. The resulting data is the signal intensity $I$ as function of the time delay $\theta$ between split beams that is directly proportional to the variation of position of the moving mirror. After a full scan, the signal $I = I(\theta)$ can then be converted from the time domain to the frequency domain by means of a Fourier transform:

$$S(\nu) = 2 \int_0^\infty I(\Delta t) cos(2\pi\nu\theta) d\theta \tag{2.4.32}$$

where $\nu$ corresponds to a given wave number and $S(\nu)$ is the signal intensity in the frequency/wave-number domain. The transformation presented in Eq. 2.4.32 is done numerically. The transformed signal $S(\nu)$ can then be averaged through the course of multiple scans. Frequencies corresponding to minimum signal intensities (maximum absorption) should correspond to specific excitations that occur in the sample as a response to infrared illumination.

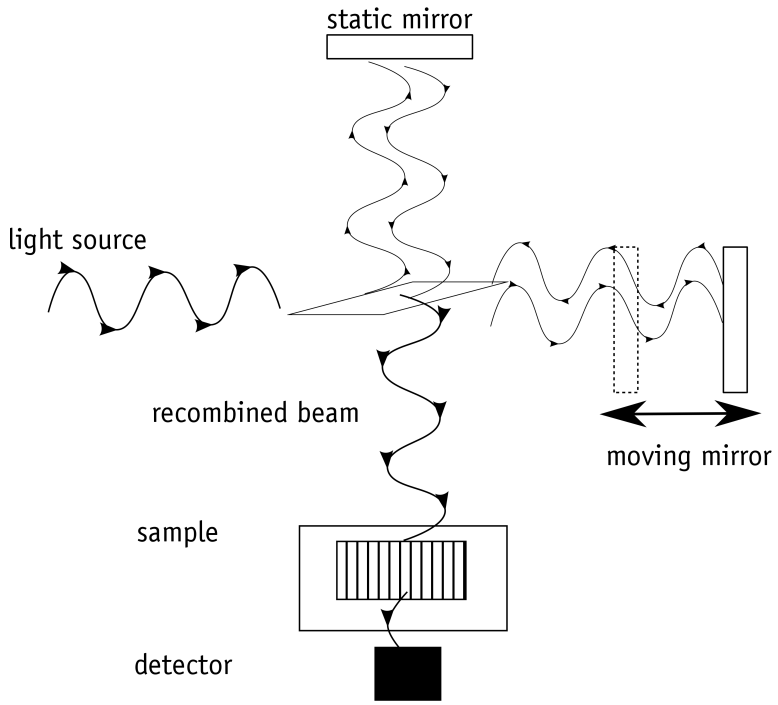


Figure 2.4.3: Concept of a Michelson interferometer for a FTIR experiment

# Bibliography


[1] L. I. Schiff, *Quantum Mechanics*, International series in pure and applied physics (McGraw-Hill, Singapore, 1955).

[2] M. Born and R. Oppenheimer, Annalen der Physik **389**, 457 (1927).

[3] P. Hohenberg and W. Kohn, Physical Review **136**, B864 (1964).

[4] J. L. Calais, International Journal of Quantum Chemistry **47**, 101 (1993).

[5] W. Kohn and L. J. Sham, Physical Review **140**, A1133 (1965).

[6] U. von Barth and L. Hedin, Journal of Physics C: Solid State Physics **5**, 1629 (1972).

[7] J. P. Perdew and A. Zunger, Physical Review B **23**, 5048 (1981).

[8] J. P. Perdew, Physica B: Condensed Matter **172**, 1 (1991).

[9] J. Heyd, G. E. Scuseria, and M. Ernzerhof, The Journal of Chemical Physics **118**, 8207 (2003).

[10] J. Paier, M. Marsman, K. Hummer, G. Kresse, I. C. Gerber, and J. G. Ángyán, The Journal of Chemical Physics **124**, 154709 (2006).

[11] J. P. Perdew, K. Burke, and M. Ernzerhof, Phys. Rev. Lett. **77**, 3865 (1996).

[12] P. Deák, B. Aradi, T. Frauenheim, E. Janzén, and A. Gali, Physical Review B **81**, 153203 (2010).

[13] V. I. Anisimov, J. Zaanen, and O. K. Andersen, Physical Review B **44**, 943 (1991).

[14] B. Himmetoglu, A. Floris, S. de Gironcoli, and M. Cococcioni, International Journal of Quantum Chemistry **114**, 14 (2014).

[15] M. Cococcioni and S. de Gironcoli, Physical Review B **71**, 035105 (2005).

[16] D. Vanderbilt, Physical Review B **41**, 7892 (1990).

[17] P. E. Blöchl, Physical Review B **50**, 17953 (1994).

[18] R. Jones and P. Briddon, in *Identification of Defects in Semiconductors*, Vol. 51A, edited by edited by M. Stavola Semiconductors and Semimetals (Academic Press, New York, 1998) p. 287.

[19] C. Hartwigsen, S. Goedecker, and J. Hutter, Physical Review B **58**, 3641 (1998).

[20] H. J. Monkhorst and J. D. Pack, Physical Review B **13**, 5188 (1976).

[21] P. Pulay, Chemical Physics Letters **73**, 393 (1980).

[22] W. H. Press, S. A. Teukolsky, W. T. Vetterling, and B. P. Flannery, *Numerical Recipes in C (2Nd Ed.): The Art of Scientific Computing* (Cambridge University Press, New York, NY, USA, 1992).

[23] S. T. Epstein, A. C. Hurley, R. E. Wyatt, and R. G. Parr, The Journal of Chemical Physics **47**, 1275 (1967).

[24] G. Henkelman, B. P. Uberuaga, and H. Jónsson, The Journal of Chemical Physics **113**, 9901 (2000).

[25] A. Resende, R. Jones, S. Öberg, and P. R. Briddon, Physical Review Letters **82**, 2111 (1999).

[26] C. Freysoldt, J. Neugebauer, and C. G. Van de Walle, Phys. Rev. Lett. **102**, 016402 (2009).

[27] D. V. Lang, Journal of Applied Physics **45**, 3023 (1974).

[28] L. Dobaczewski, I. D. Hawkins, and A. R. Peaker, Materials Science and Technology **11**, 1071 (1995).

[29] R. Brunwin, B. Hamilton, P. Jordan, and A. R. Peaker, Electronics Letters **15**, 349 (1979).

[30] M. Born and K. Huang, in *Oxfort Classic Texts* (Clarendon Press, 1954).

[31] "The infracord double-beam spectrophotometer," Clinical Science 16 (2) (1957).

# Chapter 3

# DFT+U study of electrical levels and migration barriers of early 3d and 4d transition metals in Silicon

Adapted from: A. G. Marinopoulos, *P. Santos, J. Coutinho, DFT+U study of electrical levels and migration barriers of early 3d and 4d transition metals in silicon*, Physical Review B, **92**, 075124 (2015)

**Author's contribution:** Calculation of GGA electrical levels, GGA and GGA+U migration barriers. Contribution to the writing of the text in subsections 3.3.1 (electrical levels) and 3.3.2 (Migration Barriers). Collaboration in the overall review and writing process of the paper.

## Abstract

Owing to their strong interaction with carriers, early 3d-row (Ti, V and Cr) and 4d-row (Zr, Nb and Mo) transition metals (TMs) are undesired contaminants in solar- and electronic-grade Si. The increasing stringent control of contamination levels is urging an accurate picture of their electronic structure. In the present work the electrical levels and migration energies of these TMs are determined by means of standard density-functional theory (DFT) and a rotationally-invariant formulation of DFT+$U$. The latter approach improves on the treatment of electronic correlations at the TM sites and relies on on-site Hubbard Coulomb and Hund's exchange parameters $U$ and $J$, respectively. These are calculated self-consistently from linear-response theory without fitting to experimental data. The effect of correlation was found more pronounced for Ti and V, with a strong impact on the location of their electrical levels. In most cases the agreement with the experimental data is satisfactory allowing the identification of the type and character of the levels. For Cr and Mo in particular, the results resolve longstanding controversies concerning the type and position of the levels. The obtained migration barriers display moderate charge-state and correlation dependency. High barriers were found for all metals studied, with the exception of Cr, confirming them as slow diffusers in silicon among the whole TM family.

## 3.1 Introduction

Understanding transition-metal (TM) impurities in semiconductors is simultaneously a problem with huge technological impact and a challenge in fundamental solid state physics. From a first-principles modeling perspective, the treatment of on-site correlations due to the d-electrons on the TMs, implies a departure from standard local or semi-local approximations to account for electron-electron interactions [1]. Within density-functional theory (DFT), recently developed hybrid functionals which admix a portion of exact non-local Fock exchange to the total exchange, have emerged as very accurate alternative approaches [2–4]. Nonetheless, they remain computationally expensive and they require by construction the tuning of a mixing parameter which defines the portion of the non-local exchange. Usually this parameter is chosen in order to reproduce the experimental gap or other properties of the specific bulk system under study. However, the use of a unique parameter does not warrant a proper description of d-electron defect states induced by a TM impurity when the latter is inserted in a sp-bonded semiconducting host [5]. Indeed, recent studies of TM defects in semiconductors have shown that hybrid functionals led to insufficient screening of Coulomb interactions within the localized d electrons of the TMs, failing to reduce the self-interaction error [6, 7]. The solution suggested by these authors was to apply an additional occupation-dependent potential to the d orbitals in order to satisfy a generalized Koopman's theorem.

In the present work we explore the use of an affordable first-principles methodology for the treatment of on-site exchange and correlation effects in TM point defects in semiconductors. Our case study was chosen to be the early transition metals of the 3d and 4d rows in crystalline silicon. Such defects are feared contaminants in solar- and electronic-silicon technology [8], being powerful recombination centers when dispersed in the lattice as single interstitial defects [9]. Owed to their low diffusivity, limited precipitation and segregation under thermal treatments, they are perceived as particularly detrimental in silicon photovoltaics [8]. Early studies based on electron paramagnetic resonance (EPR) pioneered by Ludwig and Woodbury [10, 11] were instrumental in resolving the hyperfine structure of the 3d-row metals in silicon and in identifying their electron spin state. Subsequent work by deep-level transient spectroscopy (DLTS) showed that both 3d- and 4d-row metals are electrically active and introduce several deep levels in the gap [8, 9, 12, 13]. Hence, it is of primary interest to be able to determine accurately the properties of these TMs in silicon, in particular, the location of their electrical levels in the gap. Understanding migration mechanisms and determining their corresponding energy barriers can also lead to a better perception and control of the kinetic processes involving these metals, in particular during annealing and gettering treatments.

TM impurities in silicon were studied in the past using a variety of first-principles approaches. These included early calculations where the crystalline host was represented by finite-sized atomic clusters [14, 15] and spin-unrestricted Green's function techniques [16–19] based on the atomic-sphere approximation. In spite of their contribution to the elucidation of the main trends regarding the electronic structure of the TMs (such as their ground-state spin configurations and the orbital symmetries of the energy levels in the gap), these studies lacked the required accuracy to provide reliable electrical levels to be compared with the experimental data. They also provided some initial estimates for migration barriers [14], but the neglect of structural-relaxation effects undermines any tentative connection to the experiments. More recently, light 3d-row TM impurities in Si have been subject to the scrutiny of *state-of-the-art* DFT calculations using transferable pseudopotentials, and including fully structural relaxation effects in periodic supercells [20–24]. Unfortunately, with the exception of Ti [23] only neutral states were considered [21][1]. Further, the reported barriers exhibited strong discrepancies with

[1] prior to this publication

the available diffusivity data, maybe reflecting the fact that the corresponding calculations were performed on rather small (sixteen-atom) supercells [20]. Interestingly, Estreicher and co-workers [25] have shown that the calculated barriers of point defects that are strongly bound to the lattice (such as interstitial oxygen) can show error bars above 0.1 eV, while the barriers of lightly bond defects (such as interstitial iron) usually show much lower discrepancies with respect to the experiments.

Among the above mentioned first-principles studies, exchange and correlation was described within the local density (LDA) or semi-local generalized-gradient (GGA) approximations, whose suitability for strongly correlated problems is questionable and prone to self-interaction errors [26]. The self-interaction error manifests itself due to an unphysical curvature of the total energy with respect to fractional electron occupations. In contrast, an exact DFT functional would lead to a piece-wise linear dependence of the energy between integer values of electron occupancies [26, 27]. One way to include on-site correlation effects within DFT is by means of the DFT+$U$ approach. This is a semi-empirical method initially introduced as a Hubbard-corrected Local Density Approximation (LDA+$U$) by Anisimov and co-workers [28], who extended the standard LDA functional with a Hubbard-type correction that contains an intra-atomic electron Coulomb interaction $U$ acting exclusively on the subset of highly correlated electrons. LDA+$U$ has been very successful in the description of insulating TM oxides bringing band gaps and other observables such as magnetic moments into much better agreement with the experiments. On-site exchange effects were also added via a screened exchange parameter $J$ [1]. However, $U$ and $J$ are system-dependent quantities and there is no obvious way to obtain them. Many DFT+$U$ studies include a preliminary step where $U$ and $J$ values are varied in order to reproduce experimentally-measured quantities such as the electronic band gap [29]. However, this common practice challenges the unbiased nature of the underlying first-principles calculations.

In the present work we employ both standard DFT and the rotationally-invariant DFT+$U$ formulation of Liechtenstein *et al.* [30] to calculate the electrical levels and migration barriers of six early 3d and 4d TM impurities in silicon, namely Ti, V, Cr, Zr, Nb and Mo. In this specific DFT+$U$ scheme the on-site $U$ and $J$ parameters enter separately (as opposed to alternative methodologies [7] where on-site correlation is accounted for through the effective interaction $U-J$), providing a flexible and clear assessment of Coulomb and exchange effects. The parameter $J$, in particular, describes intra-atomic exchange effects: it is a measure of Hund's coupling whereby mutually aligned spins preferentially occupy empty single-particle states on the same site, therefore maximizing the total spin $S$. The existence of defect states in the gap with a multitude of electron occupancies [17, 19, 31] can give rise to very different spin states with distinct $J$ values. A recent study [32] demonstrated the importance of the intra-atomic exchange $J$ to the description of magnetic susceptibilities and magneto-electric response of non-collinear antiferromagnetic materials. In the present work the on-site Hubbard $U$ and Hund's $J$ parameters are not treated as adjustable constants. Instead, they are determined self-consistently from linear-response theory and constrained DFT calculations [26, 33] that take into account the local environment of the impurity [34] and reduce the residual self-interaction error.

The paper is divided as follows: in Section 3.2 we introduce the theoretical framework for the total energy calculations, including a description of the calculation of $U$ and $J$ parameters. In Section 3.3 we start by reporting the results of the $U$ and $J$ values for all six TMs under scrutiny. We also present the results on their electrical levels and migration barriers, comparing with the existing experimental data and discussing the impact of correlation and exchange effects. Finally we close the paper in Section 3.4 with the concluding remarks.

## 3.2 Theoretical Framework

Density-functional calculations (ground state atomic and electronic structures, electrical levels and migration barriers) were carried out using the `VASP` code [35–37] and were based on the projector augmented-wave method. [38, 39] The exchange-correlation potential was accounted for within the GGA through the use of the Perdew-Burke-Ernzerhof (PBE) functional [40]. Semi-core 3s and 3p (4s and 4p) states of the 3d-row (4d-row) transition metals were described explicitly as part of the valence shells. The Kohn-Sham states were expanded in plane-waves with a kinetic energy cut-off $E_{\rm cut}$ = 300 eV. Such a cut-off energy was found sufficiently high to provide converged energy differences within a tolerance of 5 meV. For the defect calculations large 512 Si-atom cubic supercells were employed. These were constructed from a four-fold replication of the conventional 8-atom cell of silicon along each principal direction with a theoretical lattice parameter $a_0$ = 5.465 Å. The final results included full structural and electronic/spin relaxations with $L$-point sampled Brillouin-zones. A smearing width of 0.002 eV was used for filling in electronic states near the Fermi energy.

Both conventional DFT and DFT+$U$ approaches were employed on the present defect studies. In the latter case the rotationally-invariant formulation of DFT+$U$ originally introduced by Liechtenstein and co-workers [30] was adopted. Accordingly, the total energy functional of the electron $\sigma$-spin density $n^\sigma(\mathbf{r})$ is recast as

$$\begin{aligned} E_{\rm DFT+U}\left[n^\sigma(\mathbf{r}),\mathbf{n}^{I\sigma}\right] &= E_{\rm DFT}\left[n^\sigma(\mathbf{r})\right] + \\ &+ E^{U,J}_{\rm Hub}\left[\mathbf{n}^{I\sigma}\right] - E^{U,J}_{\rm dc}\left[\mathbf{n}^{I\sigma}\right], \end{aligned} \tag{3.2.1}$$

where $E_{\rm DFT}$ is the usual DFT total-energy functional and $E^{U,J}_{\rm Hub}$ is a Hubbard-type corrective functional operating exclusively on strongly correlated states (*ex.* states with angular momentum $l = 2$ or $l = 3$ on transition metals or lanthanides, respectively) that depends on a $\mathbf{n}^{I\sigma} \equiv \{n^{I\sigma}_{mm'}\}$ $2l+1$-fold occupation matrix. Superscripts $U$ and $J$ emphasize a parametric dependence on screened Coulomb and exchange constants. The $n^{I\sigma}_{mm'}$ elements are constructed from site-projections of the Kohn-Sham states $\psi^\sigma_{\mathbf{k},\lambda}$ (here labeled by a wave-vector/band-index pair, $\mathbf{k},\lambda$) onto atomic-like orbitals $\phi^I_m$ located on site $I$ with magnetic quantum number $m$. Hence, $n^{I\sigma}_{mm'} = \sum_{\mathbf{k},\lambda} f^\sigma_{\mathbf{k},\lambda}\langle\psi^\sigma_{\mathbf{k},\lambda}|P^I_{mm'}|\psi^\sigma_{\mathbf{k},\lambda}\rangle$, where $f^\sigma_{\mathbf{k},\lambda}$ is an occupation number and $P^I_{mm'} = |\phi^I_m\rangle\langle\phi^I_{m'}|$ is a generalized projection operator (see for example Ref. 26 for further details). $E^{U,J}_{\rm dc}$ is an additional correction to avoid double-counting of interactions among the correlated electrons [28].

The on-site $U$ and $J$ parameters for each TM were calculated separately by means of a linear-response procedure as proposed by Cococcioni and coworkers [26, 33] .This particular set of calculations was carried out using the `QUANTUM-ESPRESSO` package [41] considering defect configurations that were previously relaxed using the `VASP` code. Again, the underlying exchange and correlation potential was accounted for by the GGA through the use of the Perdew-Burke-Ernzerhof (PBE) functional [40]. Valence-core interactions were described by means of ultra-soft pseudopotentials [42] and the plane-wave basis cut-off was set at 300 eV. We found these values adequate to provide an acceptable convergence for the Hubbard parameters. The effect of increasing this cutoff up to 400 eV led to maximum deviations of 0.20 eV for the $U$ and $J$ parameters.

The procedure for the calculation of the $U$ parameter starts from the self-consistent density of the DFT ground state of an impurity in a supercell. The basic idea is to obtain numerically the total-energy curvature with respect to variations of the $d$-electron occupancies and

recover the exact piece-wise linear dependence [26]. This problem can be recast into linear-response calculations where the $U$ values satisfy the above requirement and are obtained from the density-response functions after imposing local perturbations to the TM sites $I$. These perturbations consist of potential shifts $\alpha_I$ of magnitude up to 0.05 eV. Next, one calculates the total on-site d-electron occupation $n_I = \sum_{\sigma,m} n^{I\sigma}_{mm}$ before and at the end of electronic self-consistency cycle, resulting in non-interacting ($\chi^0_I$) and screened ($\chi^{\rm scr}_I$) on-site response functions defined as,

$$\begin{aligned} \chi^0_I &= \frac{\Delta n^0_I}{\Delta \alpha_I} \\ \chi^{\rm scr}_I &= \frac{\Delta n^{\rm scr}_I}{\Delta \alpha_I}, \end{aligned}$$

and the on-site parameter $U$ is finally obtained from

$$U = \left(\chi^0_I\right)^{-1} - \left(\chi^{\rm scr}_I\right)^{-1}. \tag{3.2.2}$$

In a similar manner, Hund's exchange parameters $J$ for the TMs were determined from the self-consistent response of on-site magnetizations $m_I = n^{\uparrow}_I - n^{\downarrow}_I$ to on-site perturbations $\beta_I m_I$ (with $\beta_I$ values up to $\pm 0.05$ eV) imposed on the TM sites (see Ref. 33 for further details). In this case, however, we used the DFT+$U$ ground states as the non-interacting reference configurations to which the perturbations were applied.

Electrical levels of impurities were determined by means of the marker method [24]. This approach is based on a comparison between electron affinities ($A$) or ionization energies ($I$) of a particular defect under scrutiny, with analogous $A$ and $I$'s calculated for a reference system (referred to as *marker*). Unfortunately, in the absence of vacuum space, such as in the limit of an infinite solid within periodic boundary conditions, absolute values of $A$ and $I$ are ill-defined. Additional difficulties arise in the calculation of $A$ and $I$ using periodic supercells, where spurious effects such as (i) electronic dispersion of defect levels, (ii) elastic strain or (iii) long-ranged electrostatic interactions built up on a lattice of charged defects pose complications to the accuracy of the predictions.

The marker method is claimed to remove, or at least to mitigate, some of these difficulties, including a non-exact treatment of the exchange-correlation interactions through cancelation of terms at the expense of bringing in an empirical correction [24, 43]. Accordingly, a donor-transition level with respect to the valence-band (VB) edge, $E_{\rm V}$, is given by

$$\begin{aligned} E_{\rm D}(q/q+1) - E_{\rm V} &= I_{\rm D}(q/q+1) - I_{\rm M}(q/q+1) + \\ &+ \left\{E_{\rm M}(q/q+1) - E_{\rm V}\right\}_{\rm exp}, \end{aligned} \tag{3.2.3}$$

where the $I$ values are calculated from first-principles, while the third term on the right (between curly brackets) is an experimental quantity and refers to the donor level of the marker defect with respect to $E_{\rm V}$. Subscripts D, and M stand for the *defect* being examined and *marker*, respectively. Finally, the ionization energies are

$$I(q/q+1) = E(q) - E(q+1) + \xi(q) - \xi(q+1),$$

where $E(q)$ is the total energy of a defective supercell in charge state $q$, and $\xi(q)$ is a correction bundle incorporating all the above mentioned sources of errors for each charge state. The

strength of the method lies on the hypothesis that $\xi_{\mathrm{D}}(q) - \xi_{\mathrm{D}}(q+1) \approx \xi_{\mathrm{M}}(q) - \xi_{\mathrm{M}}(q+1)$ so that these corrections mutually cancel in the calculation of $I_{\mathrm{D}} - I_{\mathrm{M}}$ in Eq. 3.2.3. This is usually true when the defect under study and the marker have gap states with similar shape (symmetry and localization). We note that Eq. 3.2.3 does not involve the calculation of a band gap or a band edge energy. Donor (acceptor) levels of defects are simply calculated with respect to donor (acceptor) levels of a particular marker. Unfortunately many defects have no particularly suitable marker and the use of a proper first-principles approach is highly desirable. As proposed by Jeong and Oshiyama, [44] we may assume that our marker is a bulk supercell corresponding to $E_{\mathrm{bulk}}(q/q+1) - E_{\mathrm{V}} = 0$, and Eq. 3.2.3 simply becomes

$$E_{\mathrm{D}}(q/q+1) - E_{\mathrm{V}} = I_{\mathrm{D}}(q/q+1) - I_{\mathrm{bulk}}(q/q+1). \tag{3.2.4}$$

Although well grounded for donor (acceptor) levels with a strong admixing degree with crystalline valence band (conduction band) states, the applicability of Eq. 3.2.4 to defects with strongly localized mid-gap states could be questionable. Equation 3.2.4 involves the calculation of the valence band top energy (assumed to be $I_{\mathrm{bulk}}$), which can be erroneous when using (semi-)local DFT functionals. This problem has been recently raised by Alkauskas, Broqvist and Pasquarello [5], who showed that a proper alignment of the band edges with respect to the average electrostatic potential significantly improves the calculated levels, bringing them to a better agreement with the experiments. It was also clear that this improvement was more significant for materials with severely underestimated band gaps (such as metal oxides). Although our calculations using the bulk marker (Eq. 3.2.4) are certainly affected by such errors, we expect them to be relatively small in silicon, particularly for the case of defect-marked levels (Eq. 3.2.3). Further, the marker method has been a longstanding and successful approach to predict defect levels in group-IV semiconductors [43, 45–48].

Considering the size of the supercells employed in this work and the localization of the electronic states of interest, artificial electrostatic errors from charged calculations are likely to dominate the correction to $I_{\mathrm{D}}(q/q+1)$. To first order this can be approximated by the so-called Madelung correction [49]:

$$\xi_{\mathrm{D}}(q) - \xi_{\mathrm{D}}(q+1) \approx -\frac{\alpha_{\mathrm{M}}}{\epsilon L}(2q+1),$$

where $\alpha_{\mathrm{M}}$ is the Madelung constant of the supercell with characteristic length $L$ ($\alpha_{\mathrm{M}} = 1.41866$ and $L = 21.86$ Å for a 512-Si atom cubic supercell), and $\epsilon = 11.4$ is the static dielectric constant of silicon.

On the other hand, the Madelung correction is expected to be hardly applicable to $I_{\mathrm{bulk}}(q/q+1)$ [50]. Such calculation involves ionizing the top-most occupied crystalline state, which produces a positive charge density spanning the whole cell, along with a compensating background negative density to maintain charge neutrality. A more suitable charge correction for this case would be the electrostatic energy of *jellium*, which turns out to vanish due to long-range cancelation of the electronic, background and electron-background interactions [51]. Hence, we assume that $\xi_{\mathrm{bulk}}(q) - \xi_{\mathrm{bulk}}(q+1) \approx 0$ and a donor level with respect to the valence band top is finally obtained as

$$\begin{aligned} E_{\mathrm{D}}(q/q+1) - E_{\mathrm{V}} &= I_{\mathrm{D}}(q/q+1) - I_{\mathrm{bulk}}(q/q+1) - \\ &- \frac{\alpha_{\mathrm{M}}}{\epsilon L}(2q+1). \end{aligned} \tag{3.2.5}$$

Similar arguments are applicable for acceptor levels, although in this case we should be comparing electron affinities.

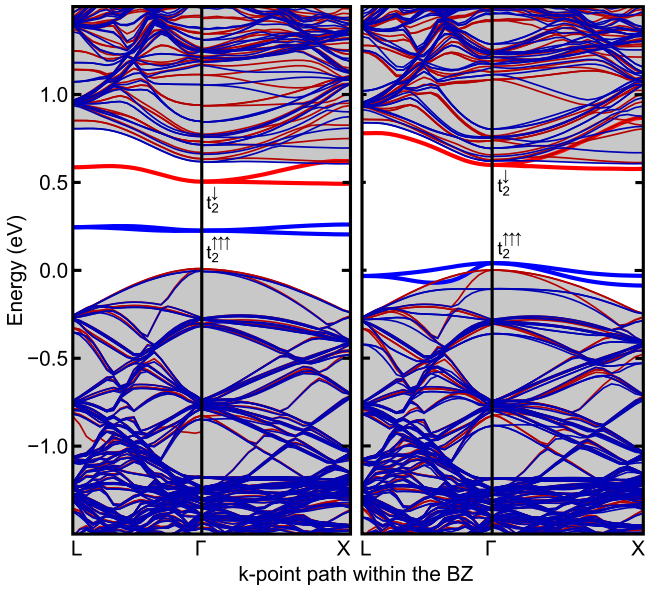


Figure 3.3.1: Band structure of an interstitial $^{1}\mathrm{Ti}^{0}$ impurity in silicon obtained within spin-polarized DFT (left) and DFT+$U$ (right). In the latter case $U$ and $J$ were equal to 4.6 eV and 0.6 eV, respectively. The electron occupations of the spin-up and spin-down channels of the triplet ($t_2$) are denoted by the arrows. Blue (red) curves denote the spin-up (spin-down) electron states. Shaded regions denote bulk-like host states. The valence-band maximum defines the zero-energy.

## 3.3 Results

Initial DFT calculations provided the minimum-energy ground states of all TMs occupying the tetrahedral interstitial positions in the silicon lattice. Structural relaxations were performed for charge states ranging from double plus to single minus. The respective electronic spin states $S$ were also found by concurrently minimizing the energy with respect to spin polarization. Several low-symmetry structures away from the perfect tetrahedral symmetry of the interstitial site were considered. This was done in order to avoid structural trapping at symmetry-constrained Jahn-Teller (JT) instabilities. The resulting electronic structure of the interstitial TMs was qualitatively similar to earlier first-principles results for the 3d-row [17, 19] and 4d-row metals [18], respectively. Regarding the effect of structural distortions away from the perfect tetrahedral symmetry, significant energy lowering was obtained for specific JT distortions mainly within DFT+$U$. In this case, the most prominent energy gains took place for the following metals (magnitude of energy lowering in meV and corresponding symmetry of the distortion given inside parentheses): $^{1}\mathrm{Ti}^{++}$ (262, $C_{3v}$), $^{1/2}\mathrm{V}^{0}$ (351, $C_{2v}$), $^{1}\mathrm{V}^{+}$ (87, $C_{3v}$), $^{1}\mathrm{Zr}^{++}$ (85, $C_{2v}$), $^{1/2}\mathrm{Nb}^{0}$ (98, $C_{3v}$), $^{1}\mathrm{Nb}^{+}$ (104, $C_{3v}$) and $^{1/2}\mathrm{Mo}^{+}$(196, $C_{3v}$), where spin and charge states are left- and right-superscripted to each species, respectively. In contrast, distortions from the ideal tetrahedral symmetry had a much smaller impact within DFT with the largest energy lowering found for $^{1/2}\mathrm{V}^{0}$ (67, $C_{3v}$) and $^{1}\mathrm{V}^{+}$ (67, $C_{3v}$). We point out that Born-Oppenheimer approximated DFT (which overlooks electron-phonon interactions) is fundamentally unsuitable to the treatment of the Jahn-Teller effect. In that respect, the above values should be considered with due caution.

In agreement with Ludwig and Woodbury [31] we found that the $d$-electron atomic levels split into triplet ($t_2$) and doublet ($e$) states when the TM atom is inside the solid. While the atomic configurations of 3d (4d)-row elements have fully occupied 4s (5s) states, in silicon

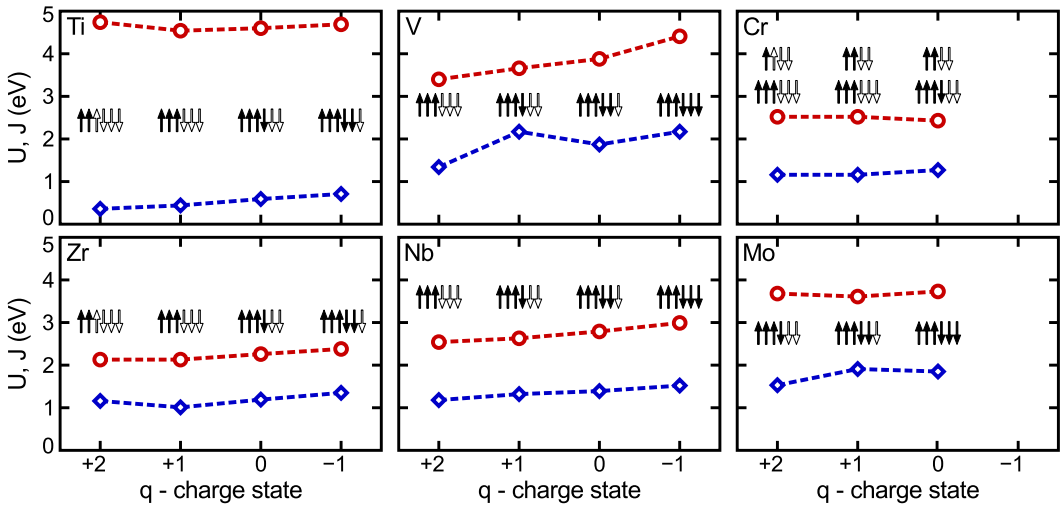


Figure 3.3.2: Magnitude of the on-site Hubbard $U$ and Hund $J$ parameters of single interstitial TMs in silicon obtained as a function of their charge/spin state. The electron occupancies from DFT calculations for both spin channels of the triplet ($t_2$) are depicted as arrows with filled (empty) symbols denoting the occupied (unoccupied) electron states. The doublet state is always empty, except for Cr, where the occupancies of the doublet ($e$) are also shown explicitly.

these states resonate with the conduction band (CB) and, therefore, their electrons drop to the lowest unoccupied $t_2 + e$ manifold in the gap. For instance, Ti with a [Ar] $3d^2$ $4s^2$ atomic configuration, when inserted at the tetrahedral interstitial site of silicon shows a $3d^4 4s^0$ electron configuration, or more precisely $(t_2^4 + e^0)\, a_1^0$ using a representation within the $T_d$ symmetry point group. For all six TMs, the $t_2$ state was always found lower in energy with respect to $e$ and therefore it is preferentially occupied. Furthermore, while $t_2$ was always calculated inside the gap (see Fig. 3.3.1), with the exception of V and Cr species, the $e$ state appeared as a resonance within the CB.

As expected, we found that DFT+$U$ tends to increase the gap between occupied and unoccupied states in the defective supercells. For the sake of example, Figure 3.3.1 compares band structures obtained from DFT (on the left) and from DFT+$U$ calculations (on the right) for a 512-Si atom supercell with a neutral Ti impurity at the tetrahedral interstitial site. Within DFT the triplet state $t_2$ is seen to lie deep in the gap with a small (although noticeable) dispersion along the chosen Brillouin zone (BZ) path. The $t_2$ spin-up channel has an occupation of three electrons, whereas the corresponding spin-down channel accommodates one electron to make a net $S = 1$ state. The highest degeneracy (symmetry) of the electronic structure holds at $\Gamma$ and $L$ points of the Brillouin zone. Within DFT+$U$ the splitting of the two $t_2$ spin channels is amplified and close to the center of the zone they mix considerably with the bulk crystalline density of states. We found that this effect is smaller at $\mathbf{k} = L$, *i.e.*, where the direct Kohn-Sham gap is wider (1.21 eV). We also note that this is the $\mathbf{k}$-point used to build the electron density, $n(\mathbf{r}) = \sum_{\lambda,\sigma} f^{\sigma}_{\mathbf{k}=L,\lambda} |\psi^{\sigma}_{\mathbf{k}=L,\lambda}(\mathbf{r})|^2$, and respective potential and total energy.

Figure 3.3.2 depicts the calculated ground state occupancy of the $t_2$ level ($t_2 + e$ levels for Cr) for all TMs considered for several charge states. These results were obtained after inspection of the Kohn-Sham states at $\mathbf{k} = L$. Triplets and doublets are represented by six-fold and four-fold sets of arrows, respectively, where the occupancy of each component is indicated by filling in the respective arrow. In general the resulting ground state for each TM impurity was

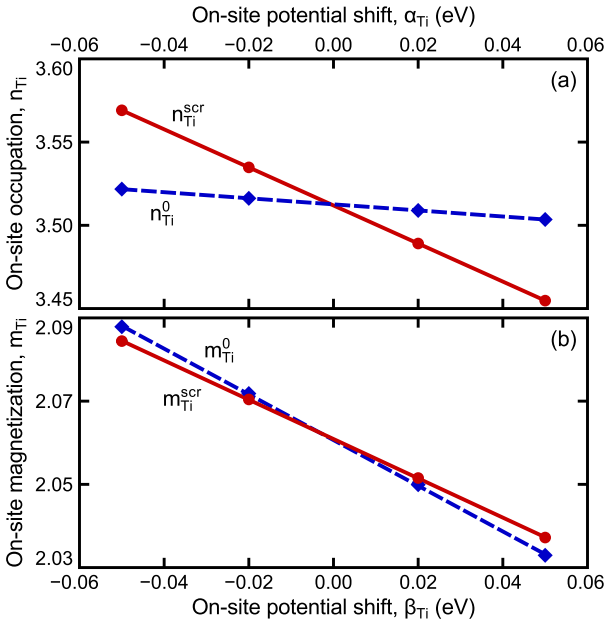


Figure 3.3.3: Non-interacting (diamonds) and screened (circles) on-site occupation (a) and magnetization (b) as a function of a local perturbation to the potential on $d$-electrons of a neutral Ti interstitial impurity in silicon. Dashed and solid lines represent the best linear fit to the data, from which $\chi^{0}_{\mathrm{Ti}}$ and $\chi^{\mathrm{scr}}_{\mathrm{Ti}}$ were obtained, respectively.

obtained from the sole occupation of the $t_2$ state. For V and Cr, where the doublet falls into the gap, we also considered configurations that resulted from the occupation of the $t_2$+$e$ manifold. Cr in particular is a borderline case within DFT as also evidenced in previous first-principles calculations [17]. Accordingly the $^{2}\mathrm{Cr}^{0}$ high-spin (HS) state (shown in Fig. 3.3.2) was nearly degenerate to the $^{0}\mathrm{Cr}^{0}$ LS state. The latter has electron occupancies analogous to Mo (see Fig. 3.3.2). The present DFT results show that the neutral HS configuration of Cr is favored with respect to the neutral LS one by 0.06 eV. Similarly, HS Cr is energetically more favorable for the other charge states as well, with the largest energy difference attained for the singly-positive charge, $\mathrm{Cr}^{+}$ (0.43 eV). V is also a borderline case. Within DFT, the neutral low-spin $^{1/2}\mathrm{V}^{0}$ ground state is slightly more stable (by 0.19 eV) when compared to the high-spin $^{5/2}\mathrm{V}^{0}$ state. Analogously, $\mathrm{V}^{+}$ preferably adopts a LS $S = 1$ state, as depicted in Fig. 3.3.2. Within DFT+$U$ the LS state $^{1/2}\mathrm{V}^{0}$ of $\mathrm{V}^{0}$ is also favored. However, now the HS state ($S = 2$) of $\mathrm{V}^{+}$ is lower in energy with respect to the LS $S = 1$ state (by 0.14 eV). The existing observations of the EPR-active charge states of the 3d-row metals are in agreement with the present findings. In particular, EPR experiments [10, 11, 52] established the following charge/spin states: $\mathrm{Ti}^{+}$, $\mathrm{V}^{++}$ and $\mathrm{Cr}^{+}$ with electron spin $S$ equal to 3/2, 3/2 and 5/2, respectively, matching the results reported in Fig. 3.3.2.

The calculations of the Hubbard $U$ and $J$ parameters were carried out using the fully relaxed TM configurations from DFT as previously outlined. As an example, Figure 3.3.3 shows the calculated d-state occupation and magnetization of a neutral Ti impurity in Si as a function of local perturbations to the on-site potential. Response functions $\chi^{0}_{I}$ and $\chi^{\mathrm{scr}}_{I}$ were obtained from the slopes of the non-interacting and screened response lines, respectively (shown up in Fig. 3.3.3 as dashed and solid lines, respectively).

The obtained values of the $U$ and $J$ parameters for the six TMs in their respective ground states are shown as circles and diamonds in Fig. 3.3.2, respectively. The same figure also

Table 3.1: Calculated $U$ and $J$ values of the six early 3d and 4d TMs in silicon (all values in eV). The results refer to the neutral DFT ground state of each metal (with corresponding spin values $S$ shown as left-superscripts on the species symbol). The electron occupancies of the spin-up and spin-down channels are also shown as arrows.

| TM | State | $U$ | $J$ |
|---|---|---|---|
| ${}^{1}\mathrm{Ti}^{0}$ | $t_2^{\uparrow\uparrow\uparrow\downarrow}e^{0}$ | 4.6 | 0.6 |
| ${}^{1/2}\mathrm{V}^{0}$ | $t_2^{\uparrow\uparrow\uparrow\downarrow\downarrow}e^{0}$ | 3.9 | 1.9 |
| ${}^{2}\mathrm{Cr}^{0}$ | $t_2^{\uparrow\uparrow\uparrow\downarrow}e^{\uparrow\uparrow}$ | 2.4 | 1.3 |
| ${}^{1}\mathrm{Zr}^{0}$ | $t_2^{\uparrow\uparrow\uparrow\downarrow}e^{0}$ | 2.3 | 1.2 |
| ${}^{1/2}\mathrm{Nb}^{0}$ | $t_2^{\uparrow\uparrow\uparrow\downarrow\downarrow}e^{0}$ | 2.8 | 1.4 |
| ${}^{0}\mathrm{Mo}^{0}$ | $t_2^{\uparrow\uparrow\uparrow\downarrow\downarrow\downarrow}e^{0}$ | 3.7 | 1.9 |

depicts the resulting spin configurations and the detailed spin-up and spin-down electron occupancies for each charge state. The magnitude of the $U$ parameters is seen to be in the 2-5 eV range whereas $J$ attains values of up to about 2 eV (the larger $J$ values are found for certain charge states of V and Mo). It is difficult to draw conclusive statements about the calculated trends of $U$ and $J$ since several factors beyond the electronic and spin occupation ordering affect the final results. These include structural relaxation effects, the position of the $t_2$ levels within the gap and mixing degree with the host density of states. In general, our calculations show that $U$ and $J$ increase slightly as electrons are added to the d-like states of the TM impurities. For the Ti/Zr and V/Nb groups the half-filled configuration of $t_2$ (three electrons of parallel spin) leads to the lowest values of $U$. On the other hand, $J$ takes its largest values for the negatively-charged state of each metal. This is consistent with earlier interpretations [33] where the positive $J$-term in the effective interaction penalizes configurations with anti-parallel spins on the same site. The magnitude of $U$ is generally higher for the 3d TMs than for their 4d counterparts, reflecting a weaker screening and the more delocalized character of the 4d orbitals. This, however, does not hold for Cr, where unlike for Mo the $e$-state drops into the gap, and shares the available d-like electrons with the $t_2$ state. To appraise the effect of eventual Jahn-Teller distortions to the final values of $U$ and $J$, further test calculations using unrelaxed supercells with the TMs occupying the interstitial tetrahedral sites were also carried out. The results showed rather small changes of both $U$ and $J$, with deviations of up to 0.15 eV and 0.25 eV, respectively.

Table 3.1 lists the $U$ and $J$ parameters for all six metals in their respective neutral ground states. These parameters were subsequently used to determine the electrical levels of the six TMs within DFT+$U$. Both $U$ and $J$ are not variational with respect to the density. Hence, $E(q/q+1)$ becomes ill-defined when obtained using different Hubbard and Hund parameters (for instance if calculated for their respective $q$ and $q+1$ charge states). This poses a difficulty in the determination of electrical levels within DFT+$U$. In the present work we assumed fixed $U$ and $J$'s, being equal to the ones for the neutral states of the respective metals. We further performed a number of test calculations of the levels, $E(q/q+1)$, in particular by averaging the $U$ and $J$ parameters over the two charge states $q$ and $q+1$ involved in the transition. The results turned out to be very similar with the largest discrepancy amounting to 0.03 eV.

### 3.3.1 Electrical levels

The calculated electrical levels for the six metals, obtained by both DFT and DFT+$U$, are listed in Table 3.2 together with the corresponding experimental results. Additionally, a graphical representation of the levels is depicted in Fig. 3.3.4, where their positioning with

respect to the band edges of bulk silicon is reproduced from the calculations. In Fig. 3.3.4 we assume that the band gap $E_C - E_V$ is the experimental value, 1.17 eV. This is actually very close to the theoretical one, if we consider the quasi-particle gap as $A - I = E(+) + E(-) - 2E(0) = 1.21$ eV, obtained using 512-Si atom supercells with the BZ sampled at $\mathbf{k} = L$. We note that this assumption is not related to a scissors-like operation — all donor (acceptor) levels are calculated with respect to $E_V$ ($E_C$). Similarly in Table 3.2, all levels are referred with respect to the band edges without involving the band gap. We started by determining the levels taking bulk Si as the marker. These are reported outside parentheses in Table 3.2 and depicted in Fig. 3.3.4.

It can be seen that in most cases, the agreement between the experimental data and both DFT and DFT+$U$ calculations is very good, with differences between theory and experiment not exceeding $\sim 0.1$ eV. A comparison between the DFT and DFT+$U$ results shows that the effect of on-site correlation is considerably more pronounced for the 3d metals, in particular for Ti and V. These are the species with the larger on-site $U$ parameters, suggesting that Coulomb effects are more important for these species. By examining the position of the electrical levels in the gap (see Fig. 3.3.4) it can be inferred that DFT+$U$ tends to shift the DFT levels towards higher energies. This effect arises from the accumulated correlation energy (underestimated in standard DFT) as we add electrons to the TM $d$ shell. This is particularly noticeable for the acceptor and single-donor levels of the 3d-row metals. For Ti, the shift in all its three levels improves the overall agreement with the reported experimental data (see Table 3.2 and Fig. 3.3.4). The most dramatic manifestation is for V where its acceptor level, V$(-/0)$, becomes almost resonant with the conduction band. This result represents the largest discrepancy of the present calculations with the existing experimental data: the experimental evidence points out to a stable and deeper V$(-/0)$ level around $E_C - 0.2$ eV [9, 53]. The acceptor level determined by DFT is even deeper ($E_C - 0.34$ eV), placing the experimental data about midway between the DFT and DFT+$U$ results.

For the case of Cr the well established Cr$(0/+)$ donor level is well reproduced by both DFT and DFT+$U$ in the upper part of the gap (see Fig. 3.3.4). Also, we did not obtain a double-donor level, Cr$(+/++)$, inside the gap by either DFT or DFT+$U$. This finding agrees with the work of Feichtinger and Szaputa [54], who combined EPR with Hall-effect measurements. While some measurements [55] did not confirm the presence of a stable double-donor level for Cr, other experimental studies [56–58] have reported a Cr$(+/++)$ level within a range from $E_V + 0.11$ eV to $E_V + 0.31$ eV. These particular observations seem to be in line with previous calculations [16, 17] that predict rather deep Cr$(+/++)$ levels either at $E_V + 0.35$ eV or at $E_V + 0.55$ eV. Our results suggest that the origin of these levels is probably due to other defect complexes involving Cr. In particular, Cr-B pair complexes in p-type silicon may give rise to such levels in the lower part of the gap [55]. Finally, our DFT and DFT+$U$ calculations for Cr predict an acceptor level inside the gap, which to our knowledge has not been observed experimentally.

For the 4d metals, the differences among DFT and DFT+$U$ results are modest and appear to scale with the magnitude of the effective Hubbard Coulomb interaction which is commonly defined as $U - J$ (see Fig. 3.3.4) [61]. For Zr (which possesses the smallest $U - J$ value of about 1 eV), the largest deviation between DFT and DFT+$U$ takes place for its acceptor level, which shifts slightly (only by 0.06 eV) closer to the CB edge. For Zr and Nb, which introduce three deep levels inside the gap, the theoretical results reproduce with very good accuracy the experimental data. For Mo, on the other hand, both DFT and DFT+$U$ predict only one deep level of single-donor character. DFT+$U$ places this level at $E_V + 0.45$ eV, a bit deeper in the gap (by about 0.14 eV) with respect to the DFT prediction. This shift is consistent with the larger $U - J$ value (of about 2 eV) for Mo. Experimentally for this metal, most existing studies

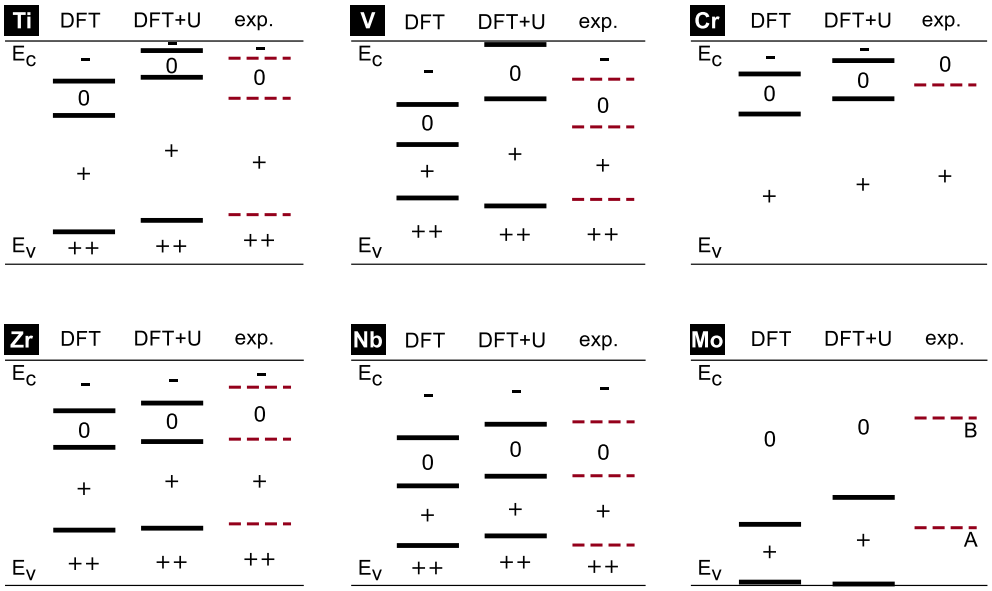


Figure 3.3.4: Graphical representation of the electrical levels of the six early 3d and 4d TMs in silicon from DFT and DFT+$U$ calculations. The results were obtained by taking as marker the bulk Si crystal. The valence-band and conduction-band edges of silicon are denoted by $E_V$ and $E_C$, respectively. The experimental levels are taken from the following works: Ref. [59]53 for Ti, Ref. 26 for V, Refs. 55, 58 for Cr, Ref. 12for Zr, Ref. 13 for Nb and Ref. 60 for Mo. Charge states of Mo levels are still a matter of debate and they are denoted by $A$ and $B$ transitions (see text).

[9, 60, 62] report a donor-like level at about $E_V + 0.30$ eV (denoted as A in Fig. 3.3.4), without however specifying whether it is the double-donor or the single-donor level of Mo. Our results clearly suggest that this level is the Mo(0/+) level rather than a double-donor transition. The latter, instead, is found to be virtually resonant with the VB top by either DFT or DFT+$U$. Furthermore, the present results show that no acceptor level can be expected inside the gap for interstitial Mo in silicon. Experimentally, the existence of additional deep levels for Mo (above the Mo(0/+) level at $E_V + 0.30$ eV) was reported in two studies which, however, place them closer to the CB edge with some further controversy regarding their nature and origin. Hamaguchi and Hayamizu [63] connected at least two prominent deep levels to Mo defects at $E_C - 0.34$ eV and $E_C - 0.27$ eV. Finally, Cox[64] reported an acceptor-like level at $E_C - 0.269$ eV (denoted as B in Fig. 3.3.4) which was ascribed to substitutional rather than interstitial Mo. Given that both our DFT and DFT+$U$ results do not predict a stable acceptor level for interstitial Mo inside the gap our view is that the acceptor level reported by Cox [64] could indeed originate from substitutional Mo, or perhaps from the interaction between interstitial Mo with an unavoidable impurity such as hydrogen. Further calculations, however, are needed to fully clarify this point.

It is clear from the discussion above that certain theoretical results require further confirmation. In particular: a) For V, the position of the acceptor level, V(−/0), determined from DFT+$U$ is found extremely close to the CB edge ($E_C - 0.01$ eV),either suggesting an unstable acceptor state, or the overestimation of correlation within the d-electrons. Most of the existing experimental studies [53, 55] report an acceptor level for interstitial V at $E_C - 0.16$ eV [9] or at $E_C - 0.20$ eV. [53] b) For Cr: the existence of a double-donor level, Cr(+/++), inside the gap. c) Confirmation that indeed the widely-observed level assigned to Mo at $E_V + 0.30$ eV is of single-donor type. In order to appraise the above issues and introduce a better level

of confidence we further determined the electrical levels using a different marker. To this end, the Ti interstitial defect was chosen as an alternative marker, for which the calculated levels (by considering as marker the bulk Si crystal) are in very good agreement with the experiments for both DFT and DFT+$U$ (see Fig. 3.3.4). The calculated levels with the Ti marker are also listed in Table 3.2, inside parentheses. The DFT+$U$ results for V($-$/0) are now slightly improved with the level lying deeper in the gap ($E_C - 0.06$ eV), a bit closer to the experimentally observed level [9]. Additionally, considerable improvement is obtained for V(0/+) and V(+/++). Concerning Cr the calculations with the Ti marker confirm the previous results – no double-donor level was found in the gap. For Mo, the Ti-marked calculations again show that it is the single-donor level, Mo(0/+), that matches well the widely-reported level at $E_V + 0.30$ eV. In fact the DFT+$U$ result at $E_V + 0.34$ eV for Mo(0/+) agrees now much better with the experimental data. Similarly to the results using the bulk-Si marker, we did not obtain further deep levels in the gap for Mo.

### 3.3.2 Migration barriers

The vast majority of experimental studies of TM diffusion in silicon has been devoted to the 3d row elements. Most of these species are believed to migrate through the lattice via a direct interstitial mechanism with reported energy barriers in the 0.4-1.0 eV range [9]. Although several 3d metals are fast diffusers in Si, diffusion data display strong differences in diffusivity across the 3d row with an increase in diffusivity by almost five orders of magnitude from Ti towards the rightmost TMs, Ni and Cu. Whereas, Cu possesses the largest diffusion coefficients observed in silicon, Ti and V on the other hand are well known slow diffusers and difficult to remove by standard gettering techniques [23, 66]. Previous calculations [9, 67, 68] based on empirical models of interatomic interactions have provided migration energies of the order of 1 eV and less. Nonetheless, the empirical nature of these models means that their predictions should be viewed as qualitative estimates. A comprehensive first-principles study of migration barriers of transition metals in silicon was presented by Kamon *et al.*[20] These authors determined the migration barriers for interstitial diffusion for all 3d-row metals within DFT in the LDA. They did not consider, however, spin polarization and made use of rather small-size silicon supercells with sixteen atoms. The obtained barriers overestimated the experimentally reported ones by a factor of two. In contrast, the recent DFT calculations of Backlund and Estreicher [23] for Ti made use of considerably larger supercells and provided migration barriers (in both its neutral and positively-charged states) in much better agreement with the experimental data.

In the present study we report both DFT and DFT+$U$ calculations of the migration barriers for diffusion of the early 3d- and 4d-row TMs in silicon. It is assumed that a direct interstitial diffusion is the dominant mechanism for these TMs. Accordingly, the metal performs consecutive atomic jumps between adjacent tetrahedral interstitial sites (T) through the hexagonal (H) site of the Si lattice, which is assumed to be the saddle-point along the migration configurational space. We checked this assumption by marginally displacing the TM away from the H site and verified that the impurity attained the T site after full relaxation. The magnitude of the migration barrier was then determined as the difference between the total energies of fully-relaxed defects at the T and H interstitial sites. In these calculations we also assumed that the total spin of the TM is conserved during the migration step, remaining equal to its value obtained in the ground state (at or near the tetrahedral site). Two charge states, the neutral and singly positive were considered for each species, a choice which covers a wide range of doping conditions. Within DFT+$U$, the corresponding on-site Hubbard and Hund parameters were then taken specifically for the charge/spin states considered (see Fig. 3.3.2).

Table 3.2: Calculated (DFT and DFT+$U$) and experimental (Exp.) electrical levels of the early 3d and 4d TMs in silicon (values in eV). The theoretical results were obtained by taking two different marker choices: the bulk Si crystal and the Ti interstitial defect (the results from the latter method are shown within parentheses).

| 3d row | Ti | | | V | | | Cr | | |
|---|---|---|---|---|---|---|---|---|---|
| | DFT | DFT+$U$ | Exp.[a] | DFT | DFT+$U$ | Exp.[b] | DFT | DFT+$U$ | Exp.[c] |
| $E_C - E(-/0)$ | 0.21 | 0.05 | 0.09 | 0.34 | 0.01 | 0.20 | 0.18 | 0.11 | - |
| | | | | (0.22) | (0.06) | | (0.06) | (0.16) | |
| $E_V + E(0/+)$ | 0.78 | 0.98 | 0.87 | 0.62 | 0.86 | 0.72 | 0.78 | 0.86 | 0.94 |
| | | | | (0.71) | (0.75) | | (0.87) | (0.75) | |
| $E_V + E(+/++)$ | 0.17 | 0.23 | 0.26 | 0.34 | 0.30 | 0.34 | - (-) | - (-) | - |
| | | | | (0.43) | (0.33) | | | | |
| 4d row | | Zr | | | Nb | | | Mo | |
| | DFT | DFT+$U$ | Exp.[d] | DFT | DFT+$U$ | Exp.[e],[f] | DFT | DFT+$U$ | Exp. |
| $E_C - E(-/0)$ | 0.27 | 0.23 | 0.14 | 0.41 | 0.34 | 0.32, 0.293 | - (-) | - (-) | 0.27[g] |
| | (0.14) | (0.28) | | (0.29) | (0.39) | | | | |
| $E_V + E(0/+)$ | 0.71 | 0.74 | 0.76 | 0.51 | 0.56 | 0.57, 0.59 | 0.31 | 0.45 | 0.30[h] |
| | (0.80) | (0.63) | | (0.60) | (0.45) | | (0.40) | (0.34) | |
| $E_V + E(+/++)$ | 0.28 | 0.29 | 0.32 | 0.20 | 0.25 | 0.21, 0.163 | 0.01 | 0.00 | - |
| | (0.37) | (0.32) | | (0.29) | (0.28) | | (0.10) | (0.03) | |

[a] Ref.59
[b] Ref. 53
[c] Ref. 55
[d] Ref. 12
[e] Ref. 13
[f] Ref. 65
[g] Refs. 63, 64
[h] Refs. 60, 62, 63

Table 3.3: Migration barriers of the early 3d and 4d TMs in silicon obtained by DFT and DFT+$U$ (values in eV). For each TM the corresponding spin values $S$ and charge states q are shown as left- and right-superscripts on the species symbol. For the positively-charged V, the DFT and DFT+$U$ results correspond to its LS and HS states, respectively. Experimental (Exp.) values are also shown for comparison.

| 3d row | $^{1}Ti^{0}$ / $^{3/2}Ti^{+}$ | $^{1/2}V^{0}$ / $^{S}V^{+}$ | $^{2}Cr^{0}$ / $^{5/2}Cr^{+}$ |
|---|---|---|---|
| DFT | 1.98 / 1.94 | 1.30 / 1.41 (S=1) | 0.77 / 0.74 |
| DFT+$U$ | 1.74 / 1.81 | 1.52 / 1.19 (S=2) | 0.72 / 0.72 |
| Exp. | 1.79[69] | 1.55[70] | 1.0[71], 0.85 [71] |
| **4d row** | $^{1}Zr^{0}$ / $^{3/2}Zr^{+}$ | $^{1/2}Nb^{0}$ / $^{1}Nb^{+}$ | $^{0}Mo^{0}$ / $^{1/2}Mo^{+}$ |
| DFT | 2.29 / 2.30 | 2.52 / 2.23 | 2.31 / 2.01 |
| DFT+$U$ | 2.48 / 2.42 | 2.44 / 2.42 | 1.70 / 2.08 |
| Exp. | - | - | 2.2[72] |

The only exception was for the positively-charged state of vanadium, $V^{+}$, which adopts a HS ($S = 2$) configuration within DFT+$U$. In this case, the corresponding $U$ and $J$ parameters were again generated for this specific state. The obtained $U$ and $J$ values were equal to 3.7 eV and 0.9 eV, respectively. These are to be compared to $U = 3.7$ eV and $J = 2.2$ eV obtained for the LS $^{1}V^{+}$ state.

The results for all positively-charged and neutral metals are listed in Table 3.3. For some of them (Ti, Cr and Zr) the magnitude of the barriers exhibits a weak dependence on the charge state. V, Nb and Mo, on the other hand, show considerable charge-state effects in their migration barriers (V only within DFT+$U$ and Nb within DFT). For Nb and Mo the DFT barrier for the neutral state exceeds that of the positively-charged state by 0.3 eV. This also holds for the DFT+$U$ barriers of V. For Mo this finding is reversed within DFT+$U$ with the barrier for its positively-charged state being larger by about 0.4 eV. Correlation effects are also moderate in most cases. For the metals with the smaller effective interaction, $U - J$, (namely Cr, Zr and Nb) the differences among DFT and DFT+$U$ values do not exceed 0.20 eV. For the other metals the differences between DFT and DFT+$U$ barriers are a bit higher than 0.20 eV (Ti and V) and attain their largest magnitude for the case of the neutral state of Mo (about 0.6 eV).

Among the 3d-row TMs it can be seen that Ti possesses the largest migration barriers (by either DFT and DFT+$U$) something that confirms its observed behavior as a slow diffusing impurity in silicon [8]. The DFT+$U$ values in this case match better the reported experimental barrier [69]. These measurements were carried out at high temperatures ($\sim 1000\,^{\circ}$C), with the Fermi level being effectively at mid-gap. Hence, they should be compared to the calculated barrier of $^{3/2}Ti^{+}$. The present DFT results for Ti also agree reasonably well with previous DFT-GGA calculations [23], which reported barriers of 1.75 eV and 1.66 eV for the neutral and positively-charged states of Ti, respectively. The calculated barriers for V are lower from those of Ti but still they are above of 1 eV. The barrier of $V^{0}$ exhibits some small dependence on the on-site correlation, with the DFT+$U$ result (1.52 eV) agreeing better to the experimental value [70] (1.55 eV). Regarding $V^{+}$, correlation effects are also observed, with the DFT+$U$ barrier of the HS $^{2}V^{+}$ state lower by about 0.2 eV with respect to the DFT one. Here however it is important to note that the DFT+$U$ result refers to the HS $S = 2$ state, which is the ground state of $V^{+}$ within this method (see Section 3.3.1). The calculated barrier for the LS $^{1}V^{+}$ within DFT+$U$ was found equal to 1.24 eV, very close to the magnitude of its HS counterpart. Cr possesses the smallest migration barriers among the metals studied. In an

early report, the barrier for Cr diffusion in silicon was measured as 1 eV [73]. However, more recent experiments performed on p-type material for an extended temperature range (down to room temperature), resulted in a migration barrier of 0.85 eV [71] .This value should represent the migration barrier of $Cr^+$, and matches well our calculations.

The 4d-row TMs also possess high migration barriers, surpassing those of their 3d-row counterparts due to their larger size. The calculations suggest that the early 4d TMs examined here should also be slow diffusers, something that is known from experimental reports for Mo [60, 72]. Furthermore, the migration barrier of 2.2 eV extracted for Mo from depth profiling measurements on Mo-implanted silicon [72], matches well the present results (see Table 3.3).

## 3.4 Concluding Remarks

We carried out a systematic study of the electrical levels and migration barriers of six early 3d-row and 4d-row TMs in silicon. By employing both a semi-local DFT functional and a rotationally-invariant DFT+$U$ approach, our analysis includes the effects of on-site correlation within the d-electron shell of each TM. The on-site Hubbard $U$ and $J$ parameters were determined self-consistently from linear response theory taking full account of the screening of the host and local bonding around the impurity. This procedure avoids ambiguities originating from alternative approaches that rely on fittings to experimental data. It also provides a physically intuitive picture of the relative importance of on-site Coulomb and exchange effects. Although the present methodology is shown to work reasonably well for the early TMs in Si, there are still insufficiencies to be addressed. Perhaps the most severe one is the well-known underestimation of the gap inherent to (semi-)local DFT functionals — in the present case, the on-site $U$ and $J$ corrections have a local effect on the TM, and not on the host. In this respect, a combination of the present approach with a more accurate hybrid-type functional could be promising [9].

Strong correlation effects were observed for the calculated levels of the 3d TMs, mainly Ti and V, which possess the largest $U$ parameters. For V in particular, inclusion of on-site correlation changed the spin ordering for the positively-charged state, leading to a high-spin $^2V^+$ ground state. The single-donor and acceptor levels were far more affected owing to the accumulated correlation which increases with the addition of electrons to the TM $d$-shell. In contrast, for the 4d metals on-site correlation effects were relatively small and scaled with the magnitude of the effective interaction $U - J$, whose range was between 1 eV (for Zr) and 2 eV (for Mo). For all TMs the agreement with the experiments is deemed satisfactory, confirming the presence of three deep levels in the gap for the metals of the two leftmost columns, Ti/Zr and V/Nb. For Cr both DFT and DFT+$U$ results reproduce well the experimentally established single-donor level in the upper part of the gap. Furthermore, no stable double-donor level is predicted for Cr by either functional, thus resolving a long-standing controversy in a number of experimental studies. For Mo the present calculations identify the well-established donor-like level at $E_V + 0.30$ eV as a single-donor type, Mo(0/+), rather than a double-donor one, Mo(+/++). The latter, instead, is found to edge the VB top.

The present study also provides first-principles calculations of migration barriers of the early TMs in silicon. Charge-state effects were found to be rather small with the exception of Nb (only within DFT), V and Mo. Correlation effects were moderate in most cases, with the larger differences observed for those metals showing larger on-site Coulomb $U$ parameters, namely Ti, V and Mo. Among the 3d-row metals, high barriers were obtained for Ti and V in very good agreement with the experiments. Cr on the other hand was found to possess considerably smaller migration barriers in the 0.72-0.77 eV range (depending on its charge

state), also matching quite well the experimentally reported value (0.85 eV). Finally, all metals from the 4d row, Zr, Nb and Mo, possess larger migration barriers than their 3d counterparts, indicating a higher difficulty in passing through the hexagonal ring of the Si lattice. The existing experimental evidence that Mo is a slow-diffusing species supports these results.

**Acknowledgements**

This work was funded by FEDER funds through the COMPETE 2020 Programme and by National Funds through FCT - Portuguese Foundation for Science and Technology under the projects UID/CTM/50025/2013 and PTDC/CTM-ENE/1973/2012.

# Bibliography


[1] B. Himmetoglu, A. Floris, S. de Gironcoli, and M. Cococcioni, International Journal of Quantum Chemistry **114**, 14 (2014).

[2] J. Heyd, G. E. Scuseria, and M. Ernzerhof, The Journal of Chemical Physics **118**, 8207 (2003).

[3] J. Heyd and G. E. Scuseria, The Journal of Chemical Physics **121**, 1187 (2004).

[4] J. Paier, M. Marsman, K. Hummer, G. Kresse, I. C. Gerber, and J. G. Ángyán, The Journal of Chemical Physics **124**, 154709 (2006).

[5] A. Alkauskas, P. Broqvist, and A. Pasquarello, physica status solidi (b) **248**, 775 (2011).

[6] P. Deák, B. Aradi, T. Frauenheim, E. Janzén, and A. Gali, Physical Review B **81**, 153203 (2010).

[7] V. Ivády, I. A. Abrikosov, E. Janzén, and A. Gali, Physical Review B **87**, 205201 (2013).

[8] A. R. Peaker, V. P. Markevich, B. Hamilton, G. Parada, A. Dudas, A. Pap, E. Don, B. Lim, J. Schmidt, L. Yu, Y. Yoon, and G. Rozgonyi, physica status solidi (a) **209**, 1884 (2012).

[9] E. R. Weber, Applied Physics A **30**, 1 (1983).

[10] H. H. Woodbury and G. W. Ludwig, Physical Review **117**, 102 (1960).

[11] G. Ludwig and H. Woodbury (Academic Press, 1962) pp. 223 – 304.

[12] H. Lemke, physica status solidi (a) **122**, 617 (1990).

[13] M. L. Polignano, D. Codegoni, G. Borionetti, F. Bonoli, J. Brivio, S. Greco, A. Marino, P. Monge, I. Patoprsta, V. Privitera, and C. Riva, ECS Transactions **33**, 133 (2010).

[14] D. E. Woon, D. S. Marynick, and S. K. Estreicher, Physical Review B **45**, 13383 (1992).

[15] G. G. DeLeo, G. D. Watkins, and W. B. Fowler, Physical Review B **25**, 4972 (1982).

[16] H. Katayama-Yoshida and A. Zunger, Physical Review B **31**, 8317 (1985).

[17] F. Beeler, O. K. Andersen, and M. Scheffler, Physical Review Letters **55**, 1498 (1985).

[18] M. Scheffler and F. Beeler, in *Defects in Semiconductors 15*, Materials Science Forum, Vol. 38 (Trans Tech Publications, 1991) pp. 257–262.

[19] F. Beeler, O. K. Andersen, and M. Scheffler, Physical Review B **41**, 1603 (1990).

[20] Y. Kamon, H. Harima, A. Yanase, and H. Katayama-Yoshida, Physica B: Condensed Matter **308**, 391 (2001), international Conference on Defects in Semiconductors.

[21] Z. Z. Zhang, B. Partoens, K. Chang, and F. M. Peeters, Physical Review B **77**, 155201 (2008).

[22] K. Sánchez, I. Aguilera, P. Palacios, and P. Wahnón, Physical Review B **79**, 165203 (2009).

[23] D. J. Backlund and S. K. Estreicher, Physical Review B **81**, 235213 (2010).

[24] V. P. Markevich, S. Leonard, A. R. Peaker, B. Hamilton, A. G. Marinopoulos, and J. Coutinho, Applied Physics Letters **104**, 152105 (2014).

[25] S. K. Estreicher, D. J. Backlund, C. Carbogno, and M. Scheffler, Angewandte Chemie International Edition **50**, 10221 (2011).

[26] M. Cococcioni and S. de Gironcoli, Physical Review B **71**, 035105 (2005).

[27] S. Lany and A. Zunger, Physical Review B **80**, 085202 (2009).

[28] V. I. Anisimov, J. Zaanen, and O. K. Andersen, Physical Review B **44**, 943 (1991).

[29] B. J. Morgan and G. W. Watson, The Journal of Physical Chemistry C **113**, 7322 (2009).

[30] A. I. Liechtenstein, V. I. Anisimov, and J. Zaanen, Physical Review B **52**, R5467 (1995).

[31] G. W. Ludwig and H. H. Woodbury, Physical Review Letters **5**, 98 (1960).

[32] E. Bousquet and N. Spaldin, Physical Review B **82**, 220402 (2010).

[33] B. Himmetoglu, R. M. Wentzcovitch, and M. Cococcioni, Physical Review B **84**, 115108 (2011).

[34] M. Wierzbowska and A. Fleszar, Physical Review B **83**, 184418 (2011).

[35] G. Kresse and J. Hafner, Physical Review B **47**, 558 (1993).

[36] G. Kresse and J. Hafner, Physical Review B **49**, 14251 (1994).

[37] G. Kresse and J. Furthmüller, Physical Review B **54**, 11169 (1996).

[38] P. E. Blöchl, Physical Review B **50**, 17953 (1994).

[39] G. Kresse and D. Joubert, Physical Review B **59**, 1758 (1999).

[40] J. P. Perdew, K. Burke, and M. Ernzerhof, Physical Review Letters **77**, 3865 (1996).

[41] P. Giannozzi, S. Baroni, N. Bonini, M. Calandra, R. Car, C. Cavazzoni, D. Ceresoli, G. L. Chiarotti, M. Cococcioni, I. Dabo, A. D. Corso, S. de Gironcoli, S. Fabris, G. Fratesi, R. Gebauer, U. Gerstmann, C. Gougoussis, A. Kokalj, M. Lazzeri, L. Martin-Samos, N. Marzari, F. Mauri, R. Mazzarello, S. Paolini, A. Pasquarello, L. Paulatto, C. Sbraccia, S. Scandolo, G. Sclauzero, A. P. Seitsonen, A. Smogunov, P. Umari, and R. M. Wentzcovitch, Journal of Physics: Condensed Matter **21**, 395502 (2009).

[42] D. Vanderbilt, Physical Review B **41**, 7892 (1990).

[43] J. G. M. Shaw and P. Briddon, "Marker-method calculations for electrical levels using gaussian-orbital basis sets," in *Theory of Defects in Semiconductors*, edited by D. A. Drabold and S. K. Estreicher (Springer Berlin Heidelberg, Berlin, Heidelberg, 2007) pp. 69–94.

[44] J.-W. Jeong and A. Oshiyama, Physical Review B **64**, 235204 (2001).

[45] J. Coutinho, V. J. B. Torres, R. Jones, and P. R. Briddon, Physical Review B **67**, 035205 (2003).

[46] J. Goss, P. Briddon, R. Jones, and S. Sque, Diamond and Related Materials **13**, 684 (2004), 14th European Conference on Diamond, Diamond-Like Materials, Carbon Nanotubes, Nitrides and Silicon Carbide.

[47] J. Coutinho, S. Öberg, V. J. B. Torres, M. Barroso, R. Jones, and P. R. Briddon, Physical Review B **73**, 235213 (2006).

[48] S. K. Estreicher, M. Sanati, and N. Gonzalez Szwacki, Physical Review B **77**, 125214 (2008).

[49] G. Makov and M. C. Payne, Physical Review B **51**, 4014 (1995).

[50] C. Freysoldt, J. Neugebauer, and C. G. Van de Walle, Physical Review Letters **102**, 016402 (2009).

[51] E. K. U. Gross, E. Runge, and O. Heinonen, *Many-particle theory / E.K.U. Gross, E. Runge, O. Heinonen* (A. Hilger Bristol ; Philadelphia, 1991) pp. ix, 433 p. :.

[52] D. A. van Wezep and C. A. J. Ammerlaan, Journal of Electronic Materials **14A**, 863 (1985).

[53] T. Sadoh, H. Nakashima, and T. Tsurushima, Journal of Applied Physics **72**, 520 (1992).

[54] H. Feichtinger and R. Czaputa, Applied Physics Letters **39**, 706 (1981).

[55] H. Conzelmann, K. Graff, and E. R. Weber, Applied Physics A **30**, 169 (1983).

[56] A. A. Zolotukhin and L. S. Milevskii, Sovietic Physics: Semiconductors **10**, 914 (1976).

[57] J. R. Davis, A. Rohatgi, R. H. Hopkins, P. D. Blais, P. Rai-Choudhury, J. R. McCormick, and H. C. Mollenkopf, IEEE Transactions on Electron Devices **27**, 677 (1980).

[58] T. Kunio, T. Yamazaki, E. Ohta, and M. Sakata, Solid-State Electronics **26**, 155 (1983).

[59] D. Mathiot and S. Hocine, Journal of Applied Physics **66**, 5862 (1989).

[60] A. Rohatgi, R. Hopkins, J. Davis, R. Campbell, and H. Mollenkopf, Solid-State Electronics **23**, 1185 (1980).

[61] S. L. Dudarev, G. A. Botton, S. Y. Savrasov, C. J. Humphreys, and A. P. Sutton, Physical Review B **57**, 1505 (1998).

[62] B. B. Paudyal, K. R. McIntosh, D. H. Macdonald, and G. Coletti, Journal of Applied Physics **107**, 054511 (2010).

[63] T. Hamaguchi and Y. Hayamizu, Japanese Journal of Applied Physics **30**, L1837 (1991).

[64] S. M. Cox, ECS Journal of Solid State Science and Technology **3**, P397 (2014).

[65] H. Pettersson, H. G. Grimmeiss, L. Tilly, K. Schmalz, and H. Kerkow, Semiconductor Science and Technology **8**, 1247 (1993).

[66] R. Singh, S. J. Fonash, and A. Rohatgi, Applied Physics Letters **49**, 800 (1986).

[67] R. Swalin, Journal of Physics and Chemistry of Solids **23**, 154 (1962).

[68] J. Utzig, Journal of Applied Physics **65**, 3868 (1989).

[69] S. Hocine and D. Mathiot, Applied Physics Letters **53**, 1269 (1988).

[70] T. Sadoh and H. Nakashima, Applied Physics Letters **58**, 1653 (1991).

[71] J. Zhu, J. Diz, D. Barbier, and A. Laugier, Materials Science and Engineering: B **4**, 185 (1989).

[72] J. L. Benton, D. C. Jacobson, B. Jackson, J. A. Johnson, T. Boone, D. J. Eaglesham, F. A. Stevie, and J. Becerro, Journal of The Electrochemical Society **146**, 1929 (1999).

[73] L. S. M. N. T. Bendik, V. S. Garnyk, Sovietic Physics: Solid State **12**, 150 (1971).

# Chapter 4

# Hydrogen passivation of titanium impurities in silicon: effect of doping conditions

**Adapted from:** P. Santos, J. Coutinho, V. J. B. Torres, M. J. Rayson, and P. R. Briddon, *Hydrogen passivation of titanium impurities in silicon: Effect of doping conditions*, Applied Physics Letters, **105**, 032108 (2014)

**Author's contribution:** Calculation of all the theoretical results presented in the paper, writing of all the sections, and contribution to the overall revision process.

## Abstract

While the contamination of solar silicon by fast diffusing transition metals can be now limited through gettering, much attention has been drawn to the slow diffusing species, especially the early 3d and 4d elements. To some extent, hydrogen passivation has been successful in healing many deep centers, including transition metals in Si. Recent deep-level transient spectroscopy (DLTS) measurements concerning hydrogen passivation of Ti revealed the existence of at least four electrical levels related to $Ti_iH_n$ in the upper-half of the gap. These findings challenge the existing models regarding both the current level assignment as well as the structure/species involved in the defects. We revisit this problem by means of density functional calculations and find that progressive hydrogenation of interstitial Ti is thermodynamically stable in intrinsic and n-doped Si. Full passivation may not be possible to attain in p-type Si as $Ti_iH_3$ and $Ti_iH_4$ are metastable against dissociation and release of bond-centered protons. All DLTS electron traps are assigned, namely E40' to $Ti_iH(-/0)$, E170' to $Ti_iH_3(0/+)$, E(270) to $Ti_iH_2(0/+)$ and E170 to $Ti_iH(0/+)$ transitions. $Ti_iH_4$ is confirmed to be electrically inert.

## 4.1 Introduction

Stringent control of contamination levels and the electrical activity of transition metals (TM) in solar-grade Si (SG-Si) have been among the major concerns of Si manufacturers [1]. The reason is simply that tolerance of SG-Si to TMs, in particular to powerful recombination centers such as Ti or V, can be as low as $10^{12}\,\mathrm{cm}^{-3}$ [2]. Such control has also been a matter of interest due to recent developments in purification methods to upgrade metallurgical Si directly to solar-Si. Besides avoiding chlorosilanes and the hydrochloric acid of the *standard* Siemens process, the production of such an upgraded SG-Si is less energy hungry, although at the expense of a resulting dirtier material [3, 4]. This means that effective routes towards limiting TM contamination and related recombination events, for instance through gettering or defect passivation, are critical and highly desirable.

TMs in Si are found in a variety of forms, ranging from isolated point-like defects to large precipitates (often located at the core of dislocations, grain boundaries or surfaces) [1, 5] While heavier 3d elements like Cu and Ni diffuse so quickly that they mostly precipitate during cooling after crystal growth, slow diffusers like Ti, V or Mo remain frozen-in and dispersed in concentrations close to their solubility limit at the melting point. These species are particularly worrying since it is reasonable to expect that a certain amount of TMs in the form of isolated atoms will have a far more detrimental impact to cell performance than a large metal-disilicide inclusion. In the latter case, electronic coupling to Si host states mostly relies on a relatively small fraction of atoms at the precipitate/Si interface.

Ti is among the most feared recombination centers in Si. Although being isovalent to Si and electrically inert when replacing a Si atom, substitutional titanium ($\mathrm{Ti_s}$) is metastable and accounts only for an insignificant fraction of all dissolved Ti impurities [6]. The ground state at the tetrahedral interstitial site [7] ($\mathrm{Ti_i}$) can adopt up to four charge states with transitions at two deep donor levels at $E(0/+) = E_\mathrm{c} - 0.27\,\mathrm{eV}$ and $E(+/++) = E_\mathrm{v} + 0.26\,\mathrm{eV}$, and an acceptor level at $E(-/0) = E_\mathrm{c} - 0.09\,\mathrm{eV}$ [8–13] . Of special relevance is the $\mathrm{Ti_i}(0/+)$ level, that showing a large capture cross section for minority carriers in p-type Si, can cause more than 60% loss to the power conversion efficiency in poly-crystalline Si solar cells for a Ti concentration of $10^{14}\,\mathrm{cm}^{-3}$ [14] .This picture has been recently questioned by Kolkovsky *et al.* [15] who report an electric field enhanced emission of electrons from the $E_\mathrm{c} - 0.09\,\mathrm{eV}$ trap. This was interpreted as a Poole-Frenkel effect and the trap was ascribed to a donor transition. On the other hand, the $E_\mathrm{c} - 0.27\,\mathrm{eV}$ trap was attributed to an acceptor level of substitutional Ti as suggested by first-principles calculations [16] .We do not share this view. It is against similar experiments carried out before [10] and calculations show that the previous prediction of a $\mathrm{Ti_s}(-/0)$ resulted from an insufficient description of correlation effects on Ti 3d orbitals when using local or semi-local functionals [6].

Hydrogen passivation offers a route for deactivation of recombination active defects. In a sense it is complementary to internal and external gettering as it allows passivation of defects that are *stuck* in the lattice [17]. This is much owed to the fact that (i) hydrogen can be conveniently introduced in Si (usually by depositing a hydrogen-soaked silicon nitride antireflection front coating), (ii) atomic H is able to diffuse long distances with low thermal budgets and driven by internal and external fields, and (iii) H binds strongly to Si radicals and TMs, often storing more than 1 eV per bond. Early attempts to passivate Ti levels with H treatments were monitored by means of deep level transient spectroscopy (DLTS) and the reports were somehow contradictory. While low-energy proton implants did not alter the Ti-related peaks [18], subsequent work on wet- and plasma-etched Ti doped material found a decrease of both Ti DLTS donor peaks and connected two levels at $E_\mathrm{c} - 0.31\,\mathrm{eV}$ and $E_\mathrm{c} - 0.57\,\mathrm{eV}$ to the formation of complexes made of $\mathrm{Ti_i}$ bound to hydrogen [12]. It was also found that $\mathrm{Ti_i}$ could

be fully passivated since the concentration of these electron traps could not account for the total decrease in concentration of the $Ti_i$ levels. Now, whether the new levels were related to transitions from a unique defect or from two distinct defects (possibly with different number of H atoms) could not be established. This problem was addressed by Backlund and Estreicher [19] by means of first-principles studies. Here, two nearly degenerate Ti-H structures were found with (0/+) levels that could be assigned to the aforementioned DLTS levels. In the most stable form, labeled $Ti_iH$, hydrogen was directly bound to the titanium ion along the $\langle 111 \rangle$ direction opposite to a Ti-Si bond. In the other structure, labeled $Ti_iH_{bc}$, H laid on a bond-center site within a distorted Si-Si bond neighboring the $Ti_i$ ion. Accordingly, first donor levels were calculated at $Ti_iH(0/+) = E_c - 0.38\,eV$ and $Ti_iH_{bc}(0/+) = E_c - 0.62\,eV$, while second donor levels were anticipated at $Ti_iH(+/++) = E_v + 0.13\,eV$ and $Ti_iH_{bc}(+/++) = E_v + 0.42\,eV$. The formation of $Ti_iH_2$ and $Ti_iH_3$ complexes was ruled out, being energetically unfavorable against release of molecular hydrogen (leaving behind $Ti_i$ and $Ti_iH$, respectively), whereas the reaction $Ti_i + 2H_2 \rightarrow Ti_iH_4$ was found to be marginally exothermic by about 0.2 eV.

The passivation of Ti by H has been revisited recently by Kolkovsky *et al.* [15, 20] by means of high-resolution Laplace DLTS. A total of four levels ascribed to Ti-H defects were reported, namely E40' at $E_c - 0.80\,meV$, E170 at $E_c - 0.34\,eV$, E170' at $E_c - 0.38\,eV$ and a deeper level at $E_c - 0.57\,eV$ detected by conventional DLTS and previously labeled E(260) [12] .The superposition of E170 and E170' peaks were related to the E(175) band of Jost and Weber [12] . From depth profile data there was a clear indication that E170' involved more H atoms than both E170 and E40' which showed similar decay profile slopes. Lately, Leonard *et al.* [13] employed conventional DLTS and capacitance-voltage (C-V) profiling measurements in n-type Si. They reported three bands related to the formation of $TiH_n$ complexes. Two of the bands, labeled $E(175)$ and $E(270)$, were consistent with the measurements of Jost and Weber [12], and correspond to electron traps with activations energies of 0.34 eV and 0.56 eV, respectively. The third level, labeled $E(45)$, was located at $E_c - 75\,meV$ and it is consistent with the E40' peak [15].By inspecting concentration depth profile data, the authors concluded that all three levels should be related to different $TiH_n$ complexes. Analogously to Ref. 12, the total concentration of $TiH_n$ electron traps did not add up to the concentration of $Ti_i$ impurities present before the H treatment, again demonstrating that complete passivation of Ti could be attained.

The above measurements present two important challenges that call for a reconciliation with theory. Firstly, they question the assignment of $Ti_iH$ and $Ti_iH_{bc}$ complexes of Ref. 19 to $E(175)$ (*i.e.* E170+E170') and $E(270)$ electron traps. E170+E170' and $E(270)$ should involve complexes with unequal number of H atoms. Secondly, the observations raised to four the number of (L)DLTS levels related to Ti-H complexes in the upper half of the gap, while the existing models can only account for two.

## 4.2 Method

We carried out first-principles calculations using a spin-density functional code, [21] within the generalized gradient approximation (GGA)[22] to the exchange correlation potential. Core states were accounted for with help of fully-separable pseudopotentials [23], leaving out the Si ($3s^2 3p^2$) and Ti ($3s^2 3p^6 3d^2 4s^2$) valence shells to be treated explicitly. The Kohn-Sham states were expanded on a basis set of atom-centered Cartesian-Gaussian functions combining 16 sp-, 28 spd- and 40 spd-like functions for H, Si and Ti species, respectively. The electron density and potential terms were Fourier transformed, using a plane-wave basis set with a cut-off energy of 200 Hr. The Si crystal was accounted for by employing 512-Si atom periodic

supercells with cubic shape and crystalline lattice parameter $a_0 = 5.498$ Å. The Brillouin Zone sampling was done at $\mathbf{k} = \Gamma$. The spin-density and atomic positions were relaxed iteratively until the self-consistent band-structure energy changed by less than $2.5\times10^{-5}$ eV and between atomic relaxation steps the total energy and atom positions changed by less than $2.5\times10^{-5}$ eV and $5.3 \times 10^{-5}$ Å, respectively.

Electrical levels of defects were estimated by using the marker method [24, 25]. This is a perturbative approach that relies on error cancelation when comparing the electron affinity (EA) or the ionization potential (IP) of a reference problem (in our case a pristine supercell) to that of a perturbed problem (defective supercell under scrutiny). Among the errors avoided we have the ill defined average potential in the cells, spurious electrostatic interactions in charged calculations or band-structure dispersion effects (see Ref. 25 for further details). For instance, a neutral Ti impurity at the tetrahedral interstitial site has a $t_2^{\uparrow\uparrow\uparrow\downarrow}$ gap state partially occupied with 4 electrons in a spin-1 configuration. By varying the occupancy of this multiplet we obtain EA $= E(-) - E(0) = 5.79$ eV and first and second ionization potentials $\mathrm{IP}_1 = E(0) - E(+) = 5.74$ eV and $\mathrm{IP}_2 = E(+) - E(++) = 5.24$ eV, respectively, where $E(q)$ is the total energy of the defective supercell and $q$ the net charge added to the defect band. Now, carrying out the same calculations for a bulk cell with 512 Si atoms we have got EA $= E(-) - E(0) = 5.89$ eV, $\mathrm{IP}_1 = E(0) - E(+) = 5.03$ eV and $\mathrm{IP}_2 = E(+) - E(++) = 5.02$ eV, noting that here EA is by definition the energy of the crystal with a free-electron on the conduction band minimum, whereas IP energies represent a state with one or two free holes on the valence band top. From these results we infer that $E_\mathrm{c}-\mathrm{Ti}(-/0) = 5.89-5.79$ eV $= 0.10$ eV, while $\mathrm{Ti}(0/+)-E_\mathrm{v} = 5.74-5.03$ eV $= 0.71$ eV and $\mathrm{Ti}(+/++)-E_\mathrm{v} = 5.24-5.02$ eV $= 0.22$ eV.

## 4.3 Results

Among the several configurations that were considered for $\mathrm{Ti_iH}_n$ complexes ($1 \le n \le 4$), the most stable had H atoms at 'ab' sites, *i.e.* at anti-bonding sites forming up to four H-Ti-Si units along $\langle 111\rangle$ directions. Figure 4.3.1(a) represents some of relevant H sites, while Figure 4.3.1(c) depicts the ground state structure for the case of $\mathrm{Ti_iH_{ab}}$, hereafter simply referred as $\mathrm{Ti_iH}$ if not specified otherwise. The $\mathrm{Ti_iH_{bc}}$ structure from Ref. 19 where H is located close to the 'bc' site (with a subsequent distortion of the Ti impurity from its tetrahedral site) was metastable by at least 0.65 eV. Other structures were even less stable. The resulting electronic structure (within the gap) of neutral $\mathrm{Ti_iH}_n$ complexes for $0 \le n \le 3$ was $\mathrm{Ti_i}\colon t_2^4$, $\mathrm{Ti_iH}\colon e^3$, $\mathrm{Ti_iH_2}\colon b_1^2$ and $\mathrm{Ti_iH_3}\colon a_1^1$, where level occupancy is superscripted. Here, level representations ($t_2$, $e$, $b_1$ and $a_1$) follow from their $T_d$, $C_{3v}$, $C_{2v}$, $C_{3v}$ symmetry point groups, respectively. The $\mathrm{Ti_iH_4}$ complex showed a clean band-gap. Despite $\mathrm{Ti_i}$ and $\mathrm{Ti_iH}$ having partially occupied multiplets, symmetry lowering accompanied by level splitting led only to tiny (few meV) energy gains.

From IP and EA calculations we arrived at the electrical levels reported in Table 4.1. The $\mathrm{Ti_iH}\colon e^3$ state is responsible for an acceptor level at $E_\mathrm{c} - 0.13$ eV along with first and second donor levels at $E_\mathrm{v} + 0.69$ eV and $E_\mathrm{v} + 0.30$ eV, respectively. Further hydrogenation effectively deactivates the acceptor level ($\mathrm{Ti_iH_2}\colon b_1^2$ is a fully occupied singlet), although two donor levels remain, now at $\mathrm{Ti_iH_2}(0/+) = E_\mathrm{v} + 0.67$ eV and $\mathrm{Ti_iH_2}(+/++) = E_\mathrm{v} + 0.36$ eV. For $\mathrm{Ti_iH_3}$ we predict a single donor level at $\mathrm{Ti_iH_3}(0/+) = E_\mathrm{v} + 0.77$ eV, while $\mathrm{Ti_iH_4}$ is confirmed to be electrically inert.

Clearly, gradual hydrogenation of Ti leads to a progressive removal of electronic states from the $\mathrm{Ti_i}$ ion and to the creation of Ti-H bonding states within the valence band. However, before moving on to the assignment of levels, let us look at the stability of neutral $\mathrm{Ti_iH}_n$

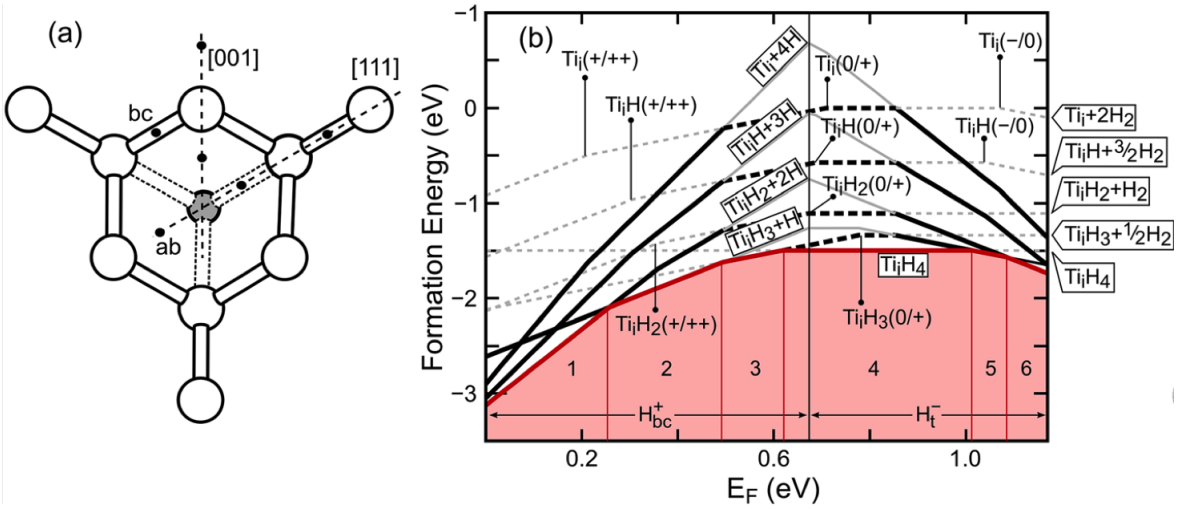


Figure 4.3.1: (a) Schematic representation of some sites (black dots) neighboring a $Ti_i$ impurity (gray atom at the center) which can be occupied by H to form $Ti_iH_n$ complexes. Particularly stable 'ab' and 'bc' sites are labeled accordingly. (b) Formation energies of $Ti_iH_n + (4-n)H$ (solid lines) and $Ti_iH_n + 1/2(4-n)H_2$ (dashed lines) as a function of the Fermi energy with $0 \leq n \leq 4$. H and $H_2$ stand for dissolved atomic (either $H_{bc}^+$ or $H_t^-$) and molecular hydrogen in Si, respectively. Thick lines represent phase diagrams of individual $Ti_iH_n$ complexes. The lowest energy set of thick (red) lines represent the combined ground state for different regions of the Fermi energy, namely: 1 - $Ti_iH_2^{++} + 2H_{bc}^+$, 2 - $Ti_iH_3^+ + H_{bc}^+$, 3 - $Ti_iH_3^+ + 1/2H_2$, 4 - $Ti_iH_4$, 5 - $Ti_iH_3 + H_t^-$ and 6 - $Ti_iH_2 + 2H_t^-$.

complexes against $Ti_iH_{n-2}$ accompanied with the release of $H_2$ molecules. Unlike in Ref. 19, $E_{b,mol}$ values from Table 4.1 are all positive and considerably large. Hence, in addition to $Ti_iH$, also $Ti_iH_2$ and $Ti_iH_3$ are stable and should be made accountable for the DLTS observations as well. We also know that only a fraction of the hydrogen in Si is found in the molecular form, so that atomic H should also be part of the equation [26]. In that regard, we calculated formation energies of $Ti_iH_n + (4-n)H$ and $Ti_iH_n + 1/2(4-n)H_2$ as a function of the Fermi energy ($E_F$) [24, 25]. In the first case hydrogen is atomically dissolved and considered as protons at bond center sites ($H_{bc}^+$) or as tetrahedral interstitial hydride anions ($H_t^-$), when $E_F$ is below or above the calculated $H(-/+) = E_v + 0.67\,eV$, respectively. In the second case it was considered as neutral $H_2$ molecules at $T_d$ sites. Chemical potentials of Si, H and Ti species were taken from energies of bulk Si, an $H_2$ molecule in Si, and $Ti_i$ in Si. Zero-point motion effects were approximated by adding $-\hbar\omega/2$ to the calculated formation energies, where the characteristic frequencies $\omega$ for $H_2$ and $H_{bc}^+$ were $3618\,cm^{-1}$ and $1998\,cm^{-1}$ [26, 27], while for $Ti_iH_n$ we considered $n$ oscillators vibrating at $1158\,cm^{-1}$, which is the calculated Ti-H stretch mode in $Ti_iH$ [19]. We should say that zero-point energy had a rather small effect (few meV) to the relative formation energies, and hence to binding energies between the reactants of interest.

Figure 4.3.1(b) summarizes the formation energy calculations from which we draw two main conclusions. (1) Reactions like $Ti_iH_n + 1/2H_2 \rightarrow Ti_iH_{n+1}$ (downward transitions between dashed lines) and $Ti_iH_n + H \rightarrow Ti_iH_{n+1}$ (downward transitions between solid lines) are exothermic under intrinsic and moderately doped n-type conditions. (2) The maximum number of H atoms that can decorate a Ti ion depends on the Fermi level. In p-type material and probably in heavily n-doped Si these reactions are endothermic when involving complexes with larger number of H atoms. This effect is evident from the bottom thick line segments

Table 4.1: Calculated electrical levels of $Ti_iH_n$ complexes in Si along with binding energies $E_{b,mol}$ for progressive hydrogenation of $Ti_i$ with molecular hydrogen ($Ti_iH_n + H_2 \rightarrow Ti_iH_{n+2} + E_{b,mol}$, with $0 \leq n \leq 2$). Experimental levels are shown within braces and were taken from Refs. 15 and 13. Electrical levels are divided into electron traps (data rows 1 and 2) and hole traps (data rows 3 and 4). Donor levels calculated with respect to the conduction band bottom, $E_c - E(0/+)$, were obtained from $E(0/+) - E_v$ values considering a band gap of 1.17 eV. All values are in eV.

| | $Ti_i$ | $Ti_iH$ | $Ti_iH_2$ | $Ti_iH_3$ |
|---|---|---|---|---|
| $E_c - E(-/0)$ | 0.10(0.07) | 0.13(0.080) | | |
| $E_c - E(0/+)$ | 0.46(0.27) | 0.48(0.34) | 0.50(0.56) | 0.39(0.38) |
| $E(0/+) - E_v$ | 0.71 | 0.69 | 0.67 | 0.77 |
| $E(+/++) - E_v$ | 0.22(0.26) | 0.30 | 0.36 | |
| $E_{b,mol}$ | 1.05 | 0.76 | 0.40 | |

limiting the graph at lower energies. While (1) suggests a *driving force* for H attachment to Ti, (2) tells us that especially in p-type material (regions 1, 2 and 3 in the graph) $Ti_iH_4$ is not thermodynamically stable against the release of bond-centered $H^+$, where only $Ti_iH_2^{++}$ and $Ti_iH_3^+$ may actually form. This agrees with the observations of a more pronounced complexing of Ti with H in n-type Si, [12] although in p-type Si Coulomb repulsion between positively charged Ti and H could further hinder the hydrogenation process.

For intrinsic conditions and lightly n-doped Si the binding energies of progressive Ti-H bonding varies from about 0.6 eV for the first Ti-H bond, to about 0.2 eV for the fourth Ti-H bond. If to these figures we add a dissociation barrier that is at least the migration barrier of H, we can end up with values compatible with the observed full recovery of the $Ti_i$ levels after anneals at 200-250°C [13] .The Si-H bond is mostly ionic where a d-like electron is donated from the $Ti^+$ cation to the $H^-$ hydride anion.

We proceed now to the assignment of the three DLTS levels reported in Ref. 13, bearing in mind that (i) E40', E170' and E(270) traps should be related to transitions from distinct complexes, [13, 20] and that (ii) E40' and E170 should be related to transitions from defects with identical number of H atoms [20]. The E40' level is the shallowest among the three electron traps, lying only 80 meV below the conduction band. From Table 4.1, $Ti_iH(-/0)$ is the obvious candidate. Further, the concentration profile of E40' indicates that this trap is the one that penetrates deeper from the surface, suggesting that it is related to a complex with a low number of hydrogen atoms. Concentration profiles of $E(270)$ at $E_c - 0.56\,eV$ and E170' at $E_c - 0.38\,eV$ decrease faster, suggesting that they involve a larger number of hydrogen atoms. Their relative positioning in the gap suggest that they are related to (0/+) transitions of $Ti_iH_2$ and $Ti_iH_3$ calculated at $E_c - 0.50\,eV$ and $E_c - 0.39\,eV$, respectively. The assignment of $Ti_iH(0/+)$ calculated at $E_c - 0.48\,eV$ is not straightforward. We tentatively assign it to E170 at $E_c - 0.34\,eV$ noting that Ref. 20 indicates that it should involve the same number H atoms as E40'. However, it also seems that E40' penetrates slightly deeper into the sample and further studies are necessary to clarify this issue.

### 4.3.1 Conclusion

In conclusion, we employed first principles density functional calculations to unveil the relative stability, binding energies and electrical activity of complexes that result from progressive decoration of titanium interstitials by hydrogen. We show that $Ti_iH_n$ complexes can form up to four $\langle 111 \rangle$-aligned $H_{ab}$-Ti-Si units. We predict that $Ti_iH_n$ complexes give rise to a total

of four levels in the upper half of the gap. They all find correspondence to the four observed electron traps from (L)DLTS studies. We confirm that $Ti_i$ impurities can be fully passivated with four H atoms, although this may be only possible under intrinsic and n-type conditions. In p-type Si, $Ti_iH_3$ and $Ti_iH_4$ are metastable against release of bond centered protons. We find second donor levels for stable $Ti_iH$ and $Ti_iH_2$ at $E_v + 0.30\,eV$ and $E_v + 0.36\,eV$, respectively. These results, combined with the Coulomb repulsion between positively charged H and $Ti_iH_n$ complexes, anticipate severe difficulties in the H-passivation of Ti impurities in p-type Si.

## Acknowledgements

We would like to thank the FCT (Portugal) for financial support under grants PTDC/CTM-ENE/1973/2012 and PEst-C/CTM/LA0025/2013. We thank Dr. Vladimir Markevich and Prof. Anthony R. Peaker for many profitable discussions.

# Bibliography


[1] T. Buonassisi, A. A. Istratov, M. D. Pickett, M. Heuer, J. P. Kalejs, G. Hahn, M. A. Marcus, B. Lai, Z. Cai, S. M. Heald, T. F. Ciszek, R. F. Clark, D. W. Cunningham, A. M. Gabor, R. Jonczyk, S. Narayanan, E. Sauar, and E. R. Weber, Progress in Photovoltaics: Research and Applications **14**, 513 (2006).

[2] B. R. Bathey and M. C. Cretella, Journal of Material Science **17**, 3077 (1982).

[3] A. F. B. Braga, S. P. Moreira, P. R. Zampieri, J. M. G. Bacchin, and P. R. Mei, Solar Energy Materials and Solar Cells **92**, 418 (2008).

[4] J. Safarian, G. Tranell, and M. Tangstad, Energy Procedia **20**, 88 (2012).

[5] D. Macdonald and J. Tan, in *Proceedings SPIE*, Vol. 6800, edited by H. H. Tan, J.-C. Chiao, L. Faraone, C. Jagadish, J. Williams, and A. R. Wilson (Canberra, ACT, Australia, 2007) pp. 68000X–68000X–7.

[6] V. P. Markevich, S. Leonard, A. R. Peaker, B. Hamilton, A. G. Marinopoulos, and J. Coutinho, Applied Physics Letters **104**, 152105 (2014).

[7] D. A. van Wezep, R. van Kemp, E. G. Sieverts, and C. A. J. Ammerlaan, Physical Review B **32**, 7129 (1985).

[8] J.-W. Chen, A. G. Milnes, and A. Rohatgi, Solid-State Electronics **22**, 801 (1979).

[9] A. C. Wang and C. T. Sah, Journal of Applied Physics **56**, 1021 (1984).

[10] D. Mathiot and S. Hocine, Journal of Applied Physics **66**, 5862 (1989).

[11] L. Tilly, H. G. Grimmeiss, H. Pettersson, K. Schmalz, K. Tittelbach, and H. Kerkow, Physical Review B **43**, 9171 (1991).

[12] W. Jost and J. Weber, Physical Review B **54**, R11038 (1996).

[13] S. Leonard, V. P. Markevich, A. R. Peaker, and B. Hamilton, Applied Physics Letters **103**, 132103 (2013).

[14] A. Rohatgi, J. R. Davis, R. H. Hopkins, P. Rai-Choudhury, P. G. McMullin, and J. R. McCormick, Solid-State Electronics **23**, 415 (1980).

[15] V. Kolkovsky, L. Scheffler, and J. Weber, Physica status solidi (c) **9**, 1996 (2012).

[16] D. J. Backlund and S. K. Estreicher, Physical Review B **81**, 235213 (2010).

[17] S. Martinuzzi, I. Périchaud, and F. Warchol, Solar Energy Materials and Solar Cells **80**, 343 (2003).

[18] R. Singh, S. J. Fonash, and A. Rohatgi, Applied Physics Letters **49**, 800 (1986).

[19] D. J. Backlund and S. K. Estreicher, Physical Review B **82**, 155208 (2010).

[20] V. Kolkovsky, L. Scheffler, and J. Weber, Physica B **439**, 24 (2014).

[21] P. Briddon and R. Jones, physica status solidi (b) **217**, 131 (2000).

[22] J. P. Perdew, K. Burke, and M. Ernzerhof, Physical Review Letters **77**, 3865 (1996).

[23] C. Hartwigsen, S. Goedecker, and J. Hutter, Physical Review B **58**, 3641 (1998).

[24] J. Coutinho, V. J. B. Torres, R. Jones, and P. R. Briddon, Physical Review B **67**, 035205 (2003).

[25] J. P. Goss, M. J. Shaw, and P. R. Briddon, in *Theory of Defects in Semiconductors*, Topics in Applied Physics, Vol. 104, edited by D. A. Drabold and S. K. Estreicher (Springer Berlin Heidelberg, 2007) pp. 69–94.

[26] A. W. R. Leitch, J. Weber, and V. Alex, Materials Science and Engineering B **58**, 6 (1999).

[27] B. B. Nielsen, K. Tanderup, M. Budde, K. B. Nielsen, J. L. Lindström, R. Jones, S. Öberg, B. Hourahine, and P. Briddon, Material Science Forum **258–263**, 391 (1997).

# Chapter 5

# First-principles calculations of iron-hydrogen reactions in silicon

**Adapted from:** P. Santos, J. Coutinho, S. Öberg, *First-principles calculations of iron-hydrogen reactions in silicon*, Journal of Applied Physics **123,** 245703 (2018).

**Author's contribution:** Calculation of all the theoretical results presented in the paper, writing of all the sections, and contribution to the overall revision process.

## Abstract

Controlling the contamination of silicon materials by iron, especially dissolved interstitial iron ($Fe_i$), is a longstanding problem with recent developments and several open issues. Among these we have the question whether hydrogen can assist iron diffusion, or if significant amounts of substitutional iron ($Fe_s$) can be created. Using density functional calculations we explore the structure, formation energies, binding energies, migration, and electronic levels of several FeH complexes in Si. We find that a weakly bound $Fe_iH$ pair has a migration barrier close to that of isolated $Fe_i$ and a donor level at $E_v + 0.5$ eV. Conversely, $Fe_iH_2(0/+)$ is estimated at $E_v + 0.33$ eV. These findings suggest that the hole trap at $E_v + 0.32$ eV measured by capacitance measurements should be assigned to $Fe_iH_2$ . $Fe_s$H-related complexes show only deep acceptor activity and are expected to have little effect on minority carrier life-time in $p$-type Si. The opposite conclusion can be drawn for $n$-type Si. We find that while in H-free material $Fe_i$ defects have lower formation energy than $Fe_s$, in hydrogenated samples $Fe_s$-related defects become considerably more stable. This would explain the observation of an EPR signal attributed to a $Fe_s$H-related complex in hydrogenated Si, which was quenched from above 1000°C to iced-water temperature.

## 5.1 Introduction

Iron is a fundamental constituent of many tools and industrial equipment, it is present in silicon raw materials, and that makes Fe contamination of Si ingots virtually unavoidable [1, 2]. Stringent control of Fe impurities in Si is particularly critical in electronic- and solar-grade materials, as a donor level at $E_v + 0.38$ eV from interstitial iron ($Fe_i$) [3], leads to powerful minority carrier recombination activity in $p$-type Si, [4] most often the material of choice for the fabrication of Si solar cells.

Hydrogenation of Silicon wafers has been recurrently applied in order to passivate, or at least reduce, the recombination activity from several defects and contaminants, including iron and other transition metals [2, 5–10]. In Si photovoltaics this hydrogenation process is usually accomplished by means of depositing and firing a hydrogen-soaked $SiN_x$ layer on top of Si, which also works as an anti-reflection coating for the front surface of the cell [11, 12]

. Other types of hydrogen introduction for passivation treatments have also been considered, including proton implantation [13] or H-plasma exposure [14], but none is as convenient as the nitridation process.

The interaction between Fe and H in silicon has been addressed in the past. Early studies by Pearton and Tavendale [14] reported the passivation of iron- and silver-related centers in $p$-type samples exposed to Hydrogen plasma. Here, the introduction of the metallic impurities was accomplished by high-temperature evaporation, and from deep-level transient spectroscopy (DLTS), the suppression of an electrical level at $E_v + 0.32$ eV, by the time connected to a Fe-O complex [15], after the H-plasma treatment was announced as an interaction between H and Fe. No direct interaction between H and interstitial Fe ($Fe_i$) was reported on these studies. More than a decade later, thermally stimulated capacitance (TSCAP) measurements performed by Sadoh *et al.* [16] using iron doped floating-zone $n$-type Si that was subject to wet-etching, displayed the same level, which was then reassigned to a FeH complex. Annealing studies showed that after 30-minute treatments at 175°C, the level disappeared, suggesting a low binding energy between Fe and H species. Despite these conclusions, there was no direct evidence for the presence of either Fe or H in the '$E_v + 0.32$ eV' center.

More recently, further evidence for a Fe-H complex in $p$-type silicon was reported by Leonard and co-workers [17].The hydrogen was introduced into the samples from a silicon nitride layer grown by plasma enhanced chemical vapor deposition. After a reverse-bias annealing at about 100°C, a hole trap was observed in the DLTS spectrum from samples with high concentrations of Fe and H. This trap was only stable up to 125°C and it was related to a donor level at $E_v + 0.31$ eV. The electronic signature of this trap coincided with that reported in Ref. 16.

The interaction of hydrogen with iron-related defects such as the iron-boron (FeB) pair and $Fe_i$ itself was also addressed by Kouketsu and Isomae [13]. In this case, hydrogen was introduced by proton implantation, leading different observations when compared to those where hydrogen plasma was used. Accordingly, along with the disappearance of the DLTS signals related to $Fe_i$ and FeB, the emergence of two hole traps at $E_v + 0.23$ eV and $E_v + 0.38$ eV was observed. It was not clear though, whether these new traps arose from the reaction between H and $Fe_i$-related complexes, or on the other hand, from complexes involving H and intrinsic defects (resulting from the implantation damage), eventually combined with Fe.

The interaction of H with FeB pairs was also studied by Yakimov and Parakhonsky using wet-etching [18], therefore avoiding implantation damage effects. Their results suggested that at room-temperature, the introduction of hydrogen actually leads to dissociation of the FeB pairs in the near surface layer, thus increasing the concentration of interstitial iron. The process leading to such dissociation is not well understood, and therefore it is worth of further

investigation.

Electron paramagnetic resonance (EPR) was also employed in the study of H-passivation of Fe in Si. Accordingly, the existence of a FeH complex with a binding energy of $\sim 1.3$ eV and stable up to $T = 220°C$ was inferred after comparing EPR spectra from Fe-doped and (Fe,H)-co-doped $n$-type floating zone Si [19]. Interestingly, the EPR signal which was assigned to the FeH complex was isotropic ($T_d$ symmetry). Unfortunately, the authors could not unambiguously demonstrate the presence of H atoms in the center, either from the EPR data or from local vibrational mode absorption using deuterated samples.

Theoretical work by the Estreicher group proposed two stable structures for the FeH complex, namely $Fe_iH$ and $Fe_sH$, involving interstitial and substitutional Fe, respectively [20]. Although under equilibrium conditions iron impurities are located at interstitial sites, there is evidence for the existence of substantial concentrations of iron substitutional ($Fe_s$) provided by emission channeling [21, 22] and Mössbauer spectroscopy [23–28]. The $Fe_iH$ model consists on a Fe-H dimer with trigonal symmetry, with the Fe atom placed at the hexagonal interstitial site, while H is located close to a neighboring tetrahedral interstitial site. This structure was anticipated to produce two electrical levels, a donor at $E_v$+0.36 eV and an acceptor at $E_c$−0.26 eV [20]. The authors also estimated an energy gain of 0.82 eV for the reaction $Fe_i + H_{BC} \rightarrow Fe_iH$ (assuming a bond-centered configuration for hydrogen and neutral defects only), consistent with the thermal stability of the '$E_v + 0.32$ eV' trap (annealing temperature of about 175°C) as reported by Sadoh *et al.* [16]. This reaction is expected to be hindered in $p$-type Si due to electrostatic repulsion between $Fe_i^+$ and $H^+$ ions.

The second structure, $Fe_sH$, was found to comprise an iron atom locked at a substitutional site, with the hydrogen atom roaming almost freely around it. This model was assigned to the EPR spectra reported by Takakashi and co-workers [19], conforming to the observed isotropic symmetry. $Fe_sH$ was predicted to produce an acceptor level at $E_c$−0.62 eV. The estimated binding energy for this structure was approximately 1.4 eV, also in good agreement with the 1.3 eV binding energy estimated from the ESR measurements [19]. Despite the agreement, the EPR data was acquired in $n$-type material and for these conditions the proposed $Fe_sH$ complex would be in a diamagnetic negative charge state, raising doubts to the correctness of this assignment.

While the early literature indicates a relatively low thermal stability for Fe-H complexes — the measured binding energies and annealing experiments on one hand [16, 17, 19], and the first-principles calculations by Szwacki *et al.* [20] on the other hand, suggest that these complexes can only survive to temperatures of at most 125-200ºC — more recently, the solar-Si community has turned the attention to the effect of hydrogenation on Fe diffusivity and gettering at higher temperatures. For instance, Ref. 29 reports a prominent decrease in the concentration of $Fe_i$ after exposing multicrystalline Si wafers to a microwave-induced remote hydrogen plasma, followed by H-effusion during 300-500°C-anneals. This is a surprisingly stable process (when compared to H-passivation using etched samples), and it was tentatively explained as a consequence of an enhanced diffusion of $Fe_i$ caused by the introduction of H, thus leading to a faster gettering kinetics.

On the other hand, Liu *et al.* [8] questioned the picture of a H-enhanced diffusivity of $Fe_i$, arguing that if that was the case, any increase of the annealing temperatures should lead to the observation of further gettering of Fe. However, they report that at 700 °C, the amount of dissolved iron reaches a minimum of about 1% of the original content, and recovers at higher temperatures. It was then suggested that up to 700 °C, the formation of a Fe-H complex should account for the decrease of $Fe_i$, and above that temperature the dissociation of the complex becomes dominant. This view was later revised after secondary-ion mass spectroscopy (SIMS) measurements combined with DLTS, annealing and analysis of the iron-

decay kinetics [30]. From the observed accumulation of Fe at the $SiN_x$ capping layer, it was concluded that the iron reduction in the Si bulk takes place via gettering at the silicon nitride films. Hydrogenation of $Fe_i$ at high-temperatures was ruled out based on the lack of electrical activity in the Si as monitored by DLTS. Further, upon removal of the $SiN_x$, subsequent high-temperature anneals did not reveal any electrical activity either.

With these observations in mind, we endeavored to calculate the stability, electrical activity and migration ability of FeH-related complexes. After describing the methodology, we report on the atomistic structure and energetics of FeH defects, their electronic activity, thermal stability and hydrogen-assisted migration of interstitial iron. We end up with a discussion of the results and conclusions.

## 5.2 Method

We employed the *Vienna Ab-initio Simulation Package* (VASP) code [31–33] to perform density functional calculations concerning the relative stability, formation energies, electrical levels and migration barriers of FeH complexes in Si. These calculations were based on the projector-augmented wave (PAW) [34] method using the generalized gradient approximated exchange-correlation functional of Perdew, Burke and Ernzerhof [35]. The PAW potentials for Fe, Si and H species were generated in the $3s^2 3p^6 3d^7 4s^1$, $3s^2 3p^2$and $1s^1$ valence configurations, respectively. The Kohn-Sham states were expanded in plane-waves with a cut off energy of 450 eV.

Our atomistic models for the defects under scrutiny were inserted on 216 Si atom supercells with a theoretical lattice parameter of $a_0 = 5.456$ Å. We employed a $2 \times 2 \times 2$ Monkhorst and Pack **k**-point grid to sample the Brillouin zone [36]. The structural optimization of our defect models was done through a conjugate gradient method, with a convergence threshold of $2.5 \times 10^{-3}$ eV/Å for the maximum force acting on the nuclei. The self-consistent electronic relaxation cycles were computed with an accuracy of $10^{-7}$ eV.

We employed the marker method [37, 38] to assess the electrical activity of the FeH complexes. The markers for the double acceptor, acceptor and donor levels are, respectively: $Ni_s(=/-) = E_c - 0.08\,eV$, $Ni_s(-/0) = E_c - 0.31\,eV$ and $Fe_i(0/+) = E_v + 0.38\,eV$ [3, 39]. The respective electron affinities ($A$) and ionization potentials ($I$) calculated using the same 216-Si supercells are: $A\{Ni_s(=/-)\} = 6.06\,eV$, $A\{Ni_s(-/0)\} = 5.99\,eV$ and $I\{Fe_i(0/+)\} = 5.73\,eV$. The image-charge corrections for all the markers and defects under scrutiny were accounted for using the algorithm proposed by Freysoldt, Neugebauer and Van de Walle [40]. The marker method consists on a direct comparison between ionization potentials (or electron affinities) of the marker and that of the defect under scrutiny. While charge-corrections to the energies are of the order of hundreds of meV, these essentially cancel in the calculated electronic levels, becoming a few meV. The error bar of the calculated levels was estimated at about 0.1 eV. This figure was estimated by calculating the $Fe_i$ and $Fe_s$ levels, but instead of a defect marker, ionization energies and electron affinities of a bulk supercell were assumed as reference energies for the valence band top and conduction band bottom edges, respectively.

Formation energies of neutral defects, $E_f^0$, were determined using the following expression:

$$E_f^0 = E_{def}^0 - \sum_i n_i \mu_i, \tag{5.2.1}$$

where $E_{def}^0$ stands for the total energy of a neutral defective supercell made of $n_i$ atoms of species $i$ with chemical potential $\mu_i$. Chemical potentials $\mu_{Si} = -5.42$ eV, $\mu_{Fe} = -9.68$ eV and

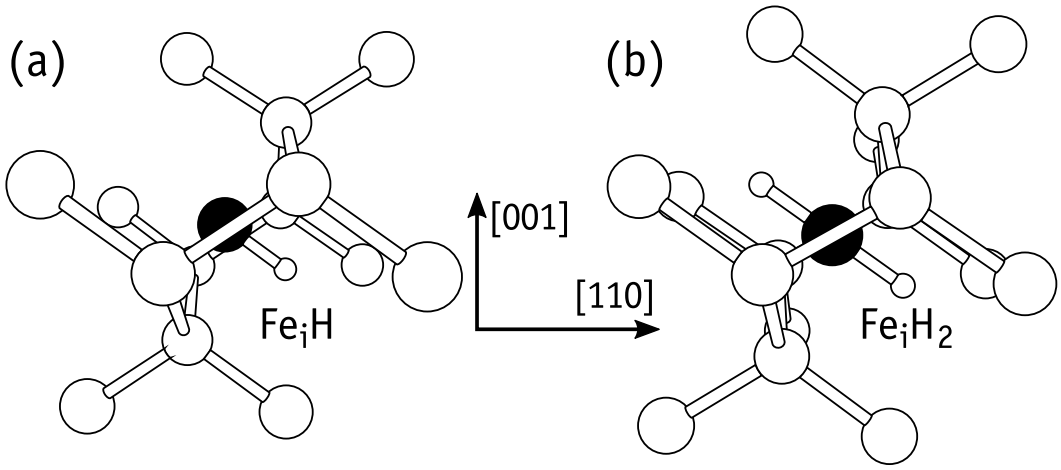


Figure 5.3.1: Ground state structure of (a) $Fe_iH$ and (b) $Fe_iH_2$ defects in silicon. The large white, black and small white spheres represent Si, Fe and H atoms, respectively. Fe-H bonds are 1.47 Å long on both defects.

$\mu_H = -3.39$ eV were obtained from bulk Si, iron disilicide ($\beta$-$FeSi_2$) and a $H_2$ molecule in a box, respectively. The formation energy of a defect in charge state $q$ has a $E_f^q \sim qE_F$ dependence, where $E_F$ is the Fermi energy with respect to the valence band top. The calculation of $E_f^q$ was carried out combining Eq. 5.2.1 and the results from the marker method described above. See Ref. 38 for further details.

Hydrogen-assisted migration of interstitial iron was also investigated. We employed a 7-image nudged elastic band (NEB) method [41] in order to estimate the migration/transformation barriers of FeH-related defects in the neutral and positive charge states. These are the relevant states to be considered in $p$-type material.

## 5.3 Results

### 5.3.1 Defect Structures

In order to determine the ground state structures of $Fe_iH$ and $Fe_sH$ defects, we started from the relaxed structures of $Fe_i$ and $Fe_s$, respectively, and introduced one or two hydrogen atoms at several possible sites, either bonding directly to the Fe atom along different directions, next to their silicon first neighbors, at second-neighboring Si-Si bond-center sites, or near the Fe-Si bond-center site.

In line with the calculations reported by Szwaki *et al.* [20], we predict that after trapping one hydrogen atom, the $Fe_i$ atom becomes more stable near the hexagonal site while connecting to H along the trigonal axis. The resulting $Fe_iH$ structure is depicted in Fig. 5.3.1(a). The defect is stable in the negative, neutral and positive charge states with spin 0, 1/2 and 1, respectively. The structure of the $Fe_iH_2$ complex is analogous, with both H atoms bonded to $Fe_i$ pointing towards opposite directions along a common $\langle 111 \rangle$ axis. This is shown in Fig. 5.3.1(b), and the defect is also stable in the $-$, 0, and + charge states with spin 1/2, 1 and 1/2, respectively.

In the case of $Fe_sH$, we found it to be bistable, with H connecting to $Fe_s$ along the $\langle 100 \rangle$ direction in the neutral charge state, or along $\langle 111 \rangle$ towards the tetrahedral interstitial site in the negative charge state. These structures are represented in the configuration coordinate

diagram of Fig. 5.3.2, and are labeled as $\{Fe_sH\}^0_A$ and $\{Fe_sH\}^-_B$ respectively. They show spin 1/2 and 0, respectively, and each of them has a unique minimum in the potential energy surface: for the negatively charged defect, structural optimization initiated in the $\{Fe_sH\}_A$ configuration relaxed into $\{Fe_sH\}_B$. Conversely, neutral $\{Fe_sH\}_B$ is unstable and spontaneously relaxes to $\{Fe_sH\}^0_A$. The energy barriers for conversion between $\{Fe_sH\}_A \leftrightarrow \{Fe_sH\}_B$ were calculated as 0.26 eV and 0.32 eV for neutral and negative charged defects. These figures are at variance with those obtained in Ref. 20 (0.08 eV) and we can only suggest that in that work the Brillouin-zone sampling that was employed ($\Gamma$-only) was not sufficiently dense considering the size of the supercells (64 atoms).

The capture of a second hydrogen atom by $Fe_s$ also leads to two stable $Fe_sH_2$ configurations in different charge states. For the neutral charge state we obtained a linear H-Fe-H configuration with both Fe-H bonds along the $\langle 100 \rangle$ crystallographic axis, pointing towards opposite directions. This structure has high symmetry ($D_{2d}$ point group) and from inspection of the Kohn-Sham band structure with identified an empty double degenerate state in the upper half of the gap. We label this structure $\{Fe_sH_2\}_A$.

In the negative charge state the doublet state becomes partially populated and the structure undergoes a Jahn-Teller distortion. This translates into a $E_{JT} \sim 0.3$ eV relaxation energy and to the formation of a slanted Fe-H bond about 10° away from the $\langle 100 \rangle$ axis. Several other low-energy distortions were found within 30 meV from the ground state. These consisted of pairs of Fe-H bonds oriented close to $\langle 100 \rangle$ and $\langle 111 \rangle$, like in $\{Fe_sH\}_A$ and $\{Fe_sH\}_B$, respectively. All non-linear H-Fe-H defects (including the ground state) were found with spin 1/2, and because they are all nearly degenerate, we refer to them as $\{Fe_sH_2\}_B$. Interestingly, the transformation barrier between these low-symmetry structures was found to be about 50 meV, indicating that the H atoms can roam almost freely around the $Fe_s$ impurity, even at cryogenic temperatures.

In the double negative charge state, the John-Teller distortion becomes stronger and both $Fe_s$-H bonds pointed approximately along orthogonal $\langle 100 \rangle$ directions. The resulting diamagnetic $\{Fe_sH_2\}^=_B$ state was found more stable than the paramagnetic $\{Fe_sH_2\}^=_A$ linear structure with spin-1 by 0.29 eV. The reorientation of a $Fe_s$-H bond now involves surmounting a barrier of 0.12 eV. All Fe-H bond lengths in $Fe_sH_n$ defects were in the range of 1.52-1.55 Å.

### 5.3.2 Electronic levels

The donor level of interstitial iron in silicon has been experimentally determined at $E_v$+0.38 eV [3]. We investigated the reaction of H with $Fe_i$ in terms of the resulting electronic activity. While $Fe_i$ is displaced from the tetrahedral site to the hexagonal site upon bonding with one or two H atoms, the electronic activity of $Fe_iH$ complexes is expected to differ significantly from that of isolated $Fe_i$. In fact, we found that besides donor activity, both $Fe_iH$ and $Fe_iH_2$ complexes are acceptors. For the $Fe_iH$ pair we obtain $(-/0)$ and $(0/+)$ levels at $E_c$−0.22 eV and $E_v$+0.50 eV. On the other hand, for $Fe_iH_2$ we calculated $(-/0)$ and $(0/+)$ levels at $E_c$−0.29 eV and $E_v$+0.33 eV, respectively. No further levels were found for $Fe_iH_n$ defects. Although our results for $Fe_iH$ are not far from previous theoretical reports [20], the $Fe_iH(0/+)$ level seems too deep to be connected to the '$E_v + 0.32$ eV' trap of Ref. 16. Alternatively, $Fe_iH_2$ shows a $(0/+)$ transition at $E_v$+0.33 eV, *i.e.* about the right placement within the gap, and therefore, must be considered as potentially accountable for the above trap as well. We will come back to this issue in Section 5.3.4.

Now we turn to the interactions between H and substitutional iron. For $\{Fe_sH\}_A$ and $\{Fe_sH\}_B$ we obtained *vertical* $(-/0)$ transitions at $E_c$−0.18 eV and $E_c$−0.76 eV. However, we note that $\{Fe_sH\}^-_A$ and $\{Fe_sH\}^0_B$ are unstable, and the relevant thermodynamic acceptor level of $Fe_sH$

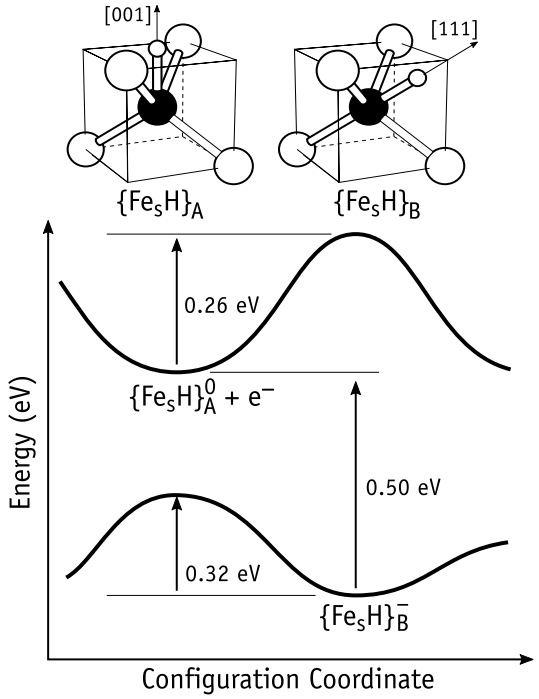


Figure 5.3.2: Configuration coordinate diagram of the $Fe_sH$ defect. The upper part of the figure includes the two ground-state configurations $\{Fe_sH\}_A$ and $\{Fe_sH\}_B$ for neutral and negative charge states, respectively. The black sphere represents Fe while the smaller and larger white spheres represent H and Si, respectively.

must be calculated from ground state energies. Hence, we obtain $Fe_sH(-/0)$ at $E_c - 0.50$ eV (see Fig. 5.3.2). Previous first-principles calculation [20] assigned $Fe_sH$ in the neutral charge state to an isotropic spin-1/2 EPR spectrum observed in $n$-type material at a temperature as low as 10 K [19]. The location of the $Fe_sH(-/0)$ level implies that under these conditions, the defect would be found in a diamagnetic negative charge state, and therefore undetectable by EPR. We could not find a second acceptor level for $Fe_sH$. Hence, the assignment of the EPR data should be revised and further work is needed to clarify this point.

For $Fe_sH_2$ we anticipate first and second acceptor levels at $E_c - 0.21$ eV and $E_c - 0.30$ eV, respectively. It is noteworthy that the second electron trap is deeper than the first, *i.e.* $Fe_sH_2$ shows an inverted ordering of the acceptor levels. This is commonly referred to as negative-$U$ and arises from a strong relaxation energy along the capture sequence, which surmounts the Coulomb repulsion between both captured electrons. Accordingly, in the neutral charge state $Fe_sH_2$ adopts structure A. This structure can capture a free-electron with a binding energy of 0.21 eV. After trapping the first electron, the structure quickly changes to $\{Fe_sH_2\}_B$, where some of the relaxation energy is effectively converted to an increase of the Coulomb attraction for the second electron, leading to a binding energy of 0.30 eV. The consequence of the negative-$U$ ordering of levels is that, under equilibrium conditions, it is energetically favorable to form a pair of $\{Fe_sH_2\}^0$ and $\{Fe_sH_2\}^=$ states than two $\{Fe_sH_2\}^-$ structures (irrespectively of the Fermi level position). Hence, $Fe_sH_2$ has an $(=/0)$ occupancy level that is located half-way between the first and second acceptor levels, *i.e.* $Fe_sH_2(=/0) = E_c - 0.26$ eV. All calculated electrical levels are shown in Table 5.1.

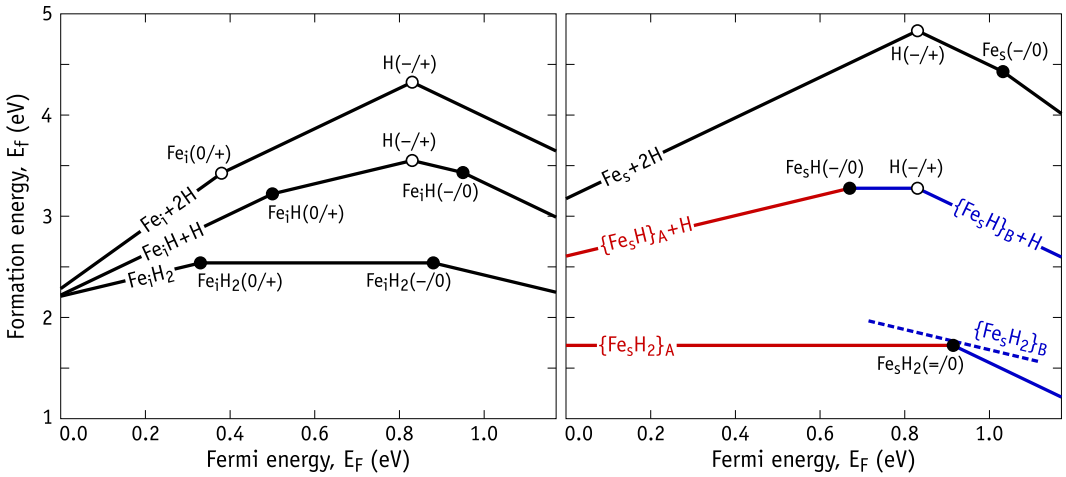


Figure 5.3.3: Diagrams with the formation energy ($E_f$) as a function of the Fermi energy ($E_F$) for different defect arrangements involving the hydrogenation of $Fe_i$ (left) and $Fe_s$ (right) defects. Open and closed circles highlight experimental and calculated electronic levels. Colors on the right diagram are used to clarify A (red) and B (blue) structures of $Fe_sH$ and $Fe_sH_2$ complexes. See text at the beginning of Section 5.3.3 for further details.

### 5.3.3 Binding energies and doping effects

The diagrams presented in Figure 5.3.3 show formation energies of several defect sets involving one $Fe_i$ impurity plus two interstitial H atoms (left), in comparison with one $Fe_s$ impurity plus two interstitial H atoms (right) as a function of the Fermi energy. On each diagram the stoichiometry is conserved. The formation energy (vertical) scales are identical for a convenient comparison. Each sequence of connected segments relates to a particular set involving a $Fe_iH_n$ or $Fe_sH_n$complex plus $2-n$ remote interstitial H atoms. The formation energy is proportional to $qE_F$, with $q$ and $E_F$ being the net charge of the whole defect set and Fermi level, respectively. Hence, positive-, zero- and negative-sloped segments refer to defect sets with net positive, neutral and negative charge, respectively. For instance, for $Fe_iH$ plus a remote H atom (on the left diagram), as the Fermi energy goes from the valence band top ($E_F = 0$) to the conduction band bottom ($E_F = 1.17$ eV), the sequence is: $\{Fe_iH\}^+ + H^+_{BC}$ (net charge $q = +2$); $\{Fe_iH\}^0 + H^+_{BC}$ (net charge $q = +1$); $\{Fe_iH\}^0 + H^-_T$ (net charge $q = -1$); $\{Fe_iH\}^- + H^-_T$ (net charge $q = -2$). Hence, each kink between adjacent segments corresponds to a particular transition level identified in the Figure. We note that transition levels of $Fe_i$ and interstitial H are measured. The latter is a negative-$U$ defect with donor and acceptor levels at $E_c - 0.18$ eV and $E_c - 0.5$ eV, leading to a $(-/+)$ occupancy level at $E_c - 0.34$ eV [42–45]. Positive and negatively charged H defects are more stable

Table 5.1: Calculated electrical levels for $Fe_iH_n$ and $Fe_sH_n$ complexes. All reported values are in eV. The inverted order of levels for $Fe_sH_2$ leads to a $(=/0)$ occupancy level at $E_c - 0.26$ eV (see text).

| | $E_c - E(=/-)$ | $E_c - E(-/0)$ | $E(0/+) - E_v$ |
|---|---|---|---|
| $Fe_iH$ | | 0.22 | 0.50 |
| $Fe_iH_2$ | | 0.29 | 0.33 |
| $Fe_sH$ | | 0.50 | |
| $Fe_sH_2$ | 0.30 | 0.21 | |

at the bond-center ($H^+_{BC}$) and tetrahedral interstitial sites ($H^-_T$), respectively. The neutral charge state (used to calculate the formation energy in Eq. 5.2.1) was found more stable in the bond-center site ($H^0_{BC}$). Experimental and calculated levels are highlighted by open and closed circles on both diagrams. Finally, on the diagram related to $Fe_sH_n$ defects, we made use of color to distinguish A and B structures of $Fe_sH$ and $Fe_sH_2$ complexes.

Looking at the diagram on the left-hand side of Figure 5.3.3 we conclude that the capture of atomic H by $Fe_i$ is an energetically favorable process regardless of the Fermi level position. The energy drop of the formation energy as we move from the upper segments ($Fe_i + 2H$) down to the lower segments ($Fe_iH_2$), represents the binding energy of the reaction $H + Fe_iH_n \rightarrow Fe_iH_{n+1}$, with $n = 0$ or 1. In intrinsic material (considering the Fermi level to be approximately at mid-gap), the capture of H by $Fe_i$ corresponds to an energy gain of $\sim 0.56$ eV. The capture of a second hydrogen atom corresponds to an energy gain of $\sim 0.80$ eV eV, leading to a total binding energy of $\sim 1.36$ eV to form a neutral $Fe_iH_2$ complex. In $p$-type materials these reactions become less exothermic and the formation of $Fe_iH_n$ complexes becomes less likely. Hydrogenation of $Fe_i$ is further hindered in $p$-type Si due to the fact that both H and $Fe_iH_n$ complexes are deep donors, implying a long-range Coulomb repulsion between reactants. On the other hand, in $n$-type Si there is no Coulomb barrier for the reaction $Fe^0_i + H^-_T \rightarrow Fe_iH^-$ and the energy drop is $\sim 0.6$ eV. The reaction with a second hydrogen atom has a binding energy of 0.75 eV, but it is likely to be inhibited by repulsion between $H^-_T$ and $\{Fe_sH\}^-$. In summary, hydrogenation of interstitial iron in Si leads to $Fe_iH_n$ complexes whose binding energies are low, and they are compatible with the annealing temperature of 125-175°C of the FeH-related complex reported in Refs. 16 and 17.

The diagram on the right-hand side of Figure 5.3.3 immediately suggests that H binds strongly to $Fe_s$, regardless of the doping type. In n-type Si the binding energies are $\sim 1.4$ eV, in excellent agreement with the measured binding energy of 1.3 eV for a FeH-related complex in $n$-type Si, where Fe was suggested to be at the substitutional site [19]. In the lower part of the right diagram we also represent the formation energy of the negatively charged $\{Fe_sH_2\}^-_B$, just above the $Fe_sH_2(=/0)$ negative-$U$ transition at $E_c - 0.26$ eV. This is show as a dashed line to stress its metastable character.

A more judicious inspection of Figure 5.3.3 allows us to conclude that, while in hydrogen-free material iron impurities have a lower formation energy at the interstitial site, in H-doped Si, the lower formation energy complexes are those involving substitutional iron. This suggests that even in $p$-type Si, high temperature anneals (maybe with optical excitation), can be used to convert highly mobile and recombination active $Fe_i$ impurities into stable and low-recombination active $Fe_s$ impurities, where H atoms act as catalysts. Although we are not the first to realize this possibility [20], it lacked theoretical support and it has been overlooked by the solar-Si community.

### 5.3.4 H-assisted diffusivity of iron

Bearing in mind the observation of the enhancement of Fe-gettering upon introduction of hydrogen (see for instance Refs. 29,8 and 30), and considering the high thermal stability of the species (or phase) holding the Fe (which survives to temperatures above 500°C), we investigated an eventual enhanced migration of $Fe_i$ assisted by H. This could lead to a faster formation of iron precipitates or out-diffusion from the Si. For the $Fe_i$ we considered a simple interstitial mechanism through the hexagonal site. In the case $Fe_iH$, the defect was found to travel as a molecule, also through neighboring hexagonal sites. As we mentioned before, a total of 7 NEB images were considered in order to determine the saddle point along the minimum energy path. The calculated migration barriers are 0.50 eV, 0.65 eV and 0.61 eV

for $Fe_i^+$, $\{Fe_iH\}^0$ and $\{Fe_iH\}^+$ respectively. The barrier for migration of $Fe_i^+$ is in very good agreement with the measurements, which is about 0.6 eV (see Ref. 4 and references therein). Both $\{Fe_iH\}^0$ and $\{Fe_iH\}^+$ have migration barriers comparable to that of interstitial iron, and in p-type Si they are considerably larger than the binding energy of H to $Fe_i$. These results suggest that hydrogen, if able to attach to $Fe_i$, does not enhance its diffusivity.

## 5.4 Discussion and conclusions

We calculated the structure, formation energies, binding energies, and electronic levels of several FeH complexes in Si. $Fe_iH$ and $Fe_iH_2$ defects consist on Fe-H and H-Fe-H pseudo-molecules, respectively, with the Fe and H atoms being located close to hexagonal and tetrahedral interstitial sites of the lattice. The modest binding energies of the H atoms to $Fe_i$ seem consistent with the annealing temperature in the range of 125-175°C reported for a hole trap at $E_v + 0.32$ eV and assigned to an iron-hydrogen complex .[16, 17, 20]. However, an assignment to $Fe_iH$ (with a single H atom) conflicts with its predicted migration barrier, which is close to that of $Fe_i$. Accordingly, both defects are expected to anneal out at close temperatures (just above room temperature). For the same reasons, $Fe_iH$ complexes are not able to account for the reduction of $Fe_i$ upon annealing hydrogenated multicrystalline wafers in the temperature range of 700-900ºC [8, 29, 30].

$Fe_iH$ and $Fe_iH_2$ complexes were predicted to be simultaneously deep donors and acceptors, and therefore are not expected to substantially decrease the recombination activity of Fe in Si. The calculated levels and binding energies suggest that the donor level measured at $E_v + 0.32$ eV from Refs. 16 and 17 is likely to arise from a $Fe_iH_n$ complex involving 2 or more H atoms. The $Fe_iH_2(0/+)$ transition is predicted at $E_v + 0.33$ eV, while $Fe_iH(0/+)$ is anticipated to occur close to mid-gap.

Substitutional iron and $Fe_sH_n$ complexes are acceptors. No donor levels were found for these defects. For the $Fe_sH$ pair we obtain a single acceptor level close to mid-gap. While this result is in line with Ref. 20, it is not regarding the calculated barrier for H motion around the $Fe_s$ impurity. In that work, the barrier was estimated to be as low as 0.08 eV, allowing the assignment of neutral $Fe_sH$ to an isotropic EPR center observed in $n$-type Si [19]. Our results do not corroborate this view. The calculated barrier for Fe-H bond reorientation is anticipated to be as high as 0.26 eV, which is not compatible with a *fast-orbiting* H atom and a motional-averaged tetrahedral symmetry at $T = 10$ K. Further, the near mid-gap location of the calculated $Fe_sH(-/0)$ deep acceptor means that in $n$-type material the stable state is diamagnetic $Fe_sH^-$ (undetectable by EPR).

Regarding $Fe_sH_2$, we found a $\langle 100 \rangle$-aligned H-Fe-H linear structure in the neutral charge state. The point symmetry of the defect is $D_{2d}$ and it has an empty doublet in the gap. Negative and double negative charge states are sensitive to Jahn-Teller distortions. The negatively charged defect is particularly interesting as it shows several possible low energy configurations with different angles between Fe-H bonds, differing by at most 30 meV in their relative energy and separated by reorientation barriers as shallow as 50 meV. Based on these findings, we suggest that the FeH-related EPR signal from Ref. 19 arises from $Fe_sH_2^-$ or other $Fe_sH_n$ complex with $n > 2$. The latter option is perhaps the most probable as $Fe_sH_2$ is a negative-$U$ complex with a metastable negative state (see dashed line segment on the right diagram of Figure 5.3.3).

Figure 5.3.3 shows that the formation energy of $Fe_i$ in non-hydrogenated Si is lower than that of $Fe_s$ by about 0.5 eV. This explains the preference of iron to occupy interstitial sites. However, in the presence of hydrogen the formation of $Fe_s$-related complexes becomes favorable. This could explain the formation of large amounts of $Fe_sH$-related defects in hydrogenated Si, as

detected by EPR after quenching the samples from 950-1250°C to 0°C [19].

**Acknowledgements**

This work was funded by the Fundação para a Ciência e a Tecnologia (FCT) under projects PTDC/CTM-ENE/1973/2012 and UID/CTM/50025/2013, and funded by FEDER funds through the COMPETE 2020 Program. Computer resources were provided by the Swedish National Infrastructure for Computing (SNIC) at PDC.

# Bibliography


[1] L. Jastrzebski, J.Lagowski, W. Henley, and P. Edelman, MRS Proceedings **354** (1994), 10.1557/PROC-354-405.

[2] A. A. Istratov, H. Hieslmair, and E. R. Weber, Applied Physics A **70**, 489 (2000).

[3] H. Feichtinger, J. Waltl, and A. Gschwandtner, Solid State Communications **27**, 867 (1978).

[4] A. A. Istratov, H. Hieslmair, and E. R. Weber, Applied Physics A **69**, 13 (1999).

[5] S. J. Pearton and A. J. Tavendale, Physical Review B **26**, 7105 (1982).

[6] R. Singh, S. J. Fonash, and A. Rohatgi, Applied Physics Letters **49**, 800 (1986).

[7] A. R. Peaker, V. P. Markevich, B. Hamilton, G. Parada, A. Dudas, A. Pap, E. Don, B. Lim, J. Schmidt, L. Yu, Y. Yoon, and G. Rozgonyi, physica status solidi (a) **209**, 1884 (2012).

[8] A. Liu, C. Sun, and D. Macdonald, Journal of Applied Physics **116**, 194902 (2014).

[9] L. Scheffler, V. Kolkovsky, and J. Weber, Journal of Applied Physics **117**, 085707 (2015).

[10] J. Mullins, S. Leonard, V. P. Markevich, I. D. Hawkins, P. Santos, J. Coutinho, A. G. Marinopoulos, J. D. Murphy, M. P. Halsall, and A. R. Peaker, physica status solidi (a) **214**, 1700304 (2017), 1700304.

[11] F. Jiang, M. Stavola, A. Rohatgi, D. Kim, J. Holt, H. Atwater, and J. Kalejs, Applied Physics Letters **83**, 931 (2003).

[12] J. K. Holt, D. G. Goodwin, A. M. Gabor, F. Jiang, M. Stavola, and H. A. Atwater, Thin Solid Films **430**, 37 (2003), proceedings of the Second International Conference on Cat-CVD (Hot Wire CVD) Process.

[13] M. Kouketsu and S. Isomae, Journal of Applied Physics **80**, 1485 (1996).

[14] S. J. Pearton and A. J. Tavendale, Journal of Physics C: Solid State Physics **17**, 6701 (1984).

[15] K. Wunstel and P. Wagner, Solid State Communications **40**, 797 (1981).

[16] T. Sadoh, K. Tsukamoto, A. Baba, D. Bai, A. Kenjo, T. Tsurushima, H. Mori, and H. Nakashima, Journal of Applied Physics **82**, 3828 (1997).

[17] S. Leonard, V. P. Markevich, A. R. Peaker, B. Hamilton, and J. D. Murphy, Applied Physics Letters **107**, 032103 (2015).

[18] E. B. Yakimov and A. L. Parakhonsky, Solid State Phenomena **57-58**, 383 (1997).

[19] T. Takahashi and M. Suezawa, Physica B: Condensed Matter **273–274**, 445 (1999).

[20] N. G. Szwacki, M. Sanati, and S. K. Estreicher, Physical Review B **78**, 113202 (2008).

[21] U. Wahl, J. G. Correia, E. Rita, J. P. Araújo, and J. C. Soares (The ISOLDE Collaboration), Physical Review B **72**, 014115 (2005).

[22] D. J. Silva, U. Wahl, J. G. Correia, and J. P. Araújo, Journal of Applied Physics **114**, 103503 (2013).

[23] D. Gilles, W. Schroter, and W. Bergholz, Physical Review B **41**, 5770 (1990).

[24] G. Langouche, Hyperfine Interactions **72**, 215 (1992).

[25] G. Weyer, S. Degroote, M. Fanciulli, V. N. Fedoseyev, G. Langouche, V. I. Mishin, A.-M. V. Bavel, A. Vantomme, and the ISOLDE Collaboration, in *Defects in Semiconductors 19*, Materials Science Forum, Vol. 258 (Trans Tech Publications, 1997) pp. 437–442.

[26] G. Weyer, A. Burchard, M. Fanciulli, V. N. Fedoseyev, H. P. Gunnlaugsson, V. I. Mishin, and R. Sielemann, Physica B: Condensed Matter **273**, 363 (1999).

[27] Y. Yoshida, Y. Kobayashi, A. Yoshida, X. Diao, S. Ogawa, K. Hayakawa, K. Yukihira, F. Shimura, and F. Ambe, Hyperfine Interactions **141**, 157 (2002).

[28] Y.Yoshida, S. Ogawa, and K. Arikawa, Physica B: Condensed Matter **340**, 605 (2003), proceedings of the 22nd International Conference on Defects in Semiconductors.

[29] P. Karzel, A. Frey, S. Fritz, and G.Hahn, Journal of Applied Physics **113**, 114903 (2013).

[30] A. Y. Liu, C. Sun, V. P. Markevich, A. R. Peaker, J. D. Murphy, and D. Macdonald, Journal of Applied Physics **120**, 193103 (2016).

[31] G. Kresse and J. Hafner, Physical Review B. **47**, 558 (1993).

[32] G. Kresse and J. Hafner, Physical Review B **49**, 14251 (1994).

[33] G. Kresse and J. Furthmüller, Physical Review B **54**, 11169 (1996).

[34] P. E. Blöchl, Physical Review B **50**, 17953 (1994).

[35] J. P. Perdew, K. Burke, and M. Ernzerhof, Physical Review Letters **77**, 3865 (1996).

[36] H. J. Monkhorst and J. D. Pack, Physical Review B **13**, 5188 (1976).

[37] A. Resende, R. Jones, S. Oberg, and P. R. Briddon, Physical Review Letters **82**, 2111 (1999).

[38] J. Coutinho, V. J. B. Torres, R. Jones, and P. R. Briddon, Physical Review B **67**, 035205 (2003).

[39] M. Shiraishi, J.-U. Sachse, H. Lemke, and J. Weber, Materials Science and Engineering: B **58**, 130 (1999).

[40] C. Freysoldt, J. Neugebauer, and C. G. V. de Walle, Physical Review Letters **102** (2009), 10.1103/physrevlett.102.016402.

[41] G. Henkelman, B. P. Uberuaga, and H. Jonsson, The Journal of Chemical Physics **113**, 9901 (2000).

[42] B. Holm, K. B. Nielsen, and B. B. Nielsen, Physical Review Letters **66**, 2360 (1991).

[43] N. Johnson, C. Herring, and C. V. de Walle, Physical Review Letters **74**, 1889 (1995).

[44] K. B. Nielsen, B. B. Nielsen, J. Hansen, E. Andersen, and J. U. Andersen, Physical Review B **60**, 1716 (1999).

[45] K. B. Nielsen, L. Dobaczewski, S. Sogard, and B. B. Nielsen, Physical Review B **65**, 075205 (2002).

# Chapter 6

# Theory of a carbon-oxygen-hydrogen recombination center in n-type Si

**Adapted from:** P. Santos, J. Coutinho, S. Öberg, M. Vaqueiro-Contreras, V. P. Markevich, M. P. Halsall, A. R. Peaker, *Theory of a carbon-oxygen-hydrogen recombination center in n-type Si,* Physica Status Solidi A, **214**, No. 7, 1700309 (2017)

**Author's contribution:** Calculation of all the theoretical results presented in the paper, writing of all the sections, and contribution to the overall revision process.

## Abstract

We have recently found that in-diffusion of hydrogen into n-type Si crystals containing oxygen and carbon impurities can result in the formation of powerful recombination centers [1]. Here we describe a combination of first-principles calculations and electrical measurements to investigate the composition, structure, electrical activity and recombination mechanism of a carbon-oxygen-hydrogen complex (COH) in Si. We found a defect comprising a carbon-oxygen complex connected to an H atom whose location depends on the charge state of the complex, and showing a calculated acceptor level at $E_{\mathrm{v}} + 0.3\,\mathrm{eV}$, a few meV away from the observations.

## 6.1 Introduction

Hydrogen, oxygen and carbon species are common contaminants in several kinds of silicon materials. Their origin is broad-based, ranging from the graphite components in the Czochralski (Cz) furnace (carbon), to the intrinsic composition of the $SiO_2$ crucible (oxygen), or simply they may be unavoidable (such as hydrogen) [2–4]. Their presence is not always unintentional though. For instance, during solar cell fabrication, specific impurities are deliberately introduced, one prominent example being the deposition of a front-facing silicon nitride antireflection layer, which introduces large quantities of fast-diffusing atomic hydrogen into the Si [5]. This process brings important benefits, such as the reduction of surface recombination, but the underlying mechanism and possible side-effects of H injection are far from clear. Isolated carbon and oxygen impurities in Si are electrically inert and have been subjected to extensive experimental and theoretical studies. In as-grown Cz-Si, they occur in large concentrations (usually in magnitudes of ppm atoms), normally occupying substitutional ($C_s$) and bond-centered interstitial ($O_i$) sites of the Si lattice, respectively. More than four decades ago, Newman, Willis and Bean assigned an infrared absorption band at 1104 $cm^{-1}$ to a vibrational mode localized on a substitutional-carbon-interstitial-oxygen (CO) complex in Si [6, 7]. Combined annealing and isotope frequency shift data led the authors to the interpretation that the band resulted from the capture of a diffusing $O_i$ impurity, which becomes mobile above $\sim 450\,^{\circ}C$, by a substitutional carbon atom. These results were later supported and translated into an atomistic model by Kaneta and co-workers [8], where the O atom was not directly connected to C. Instead, C and O atoms were separated by an intermediate Si atom forming a $C_s$-Si-$O_i$ unit, avoiding the formation of a C-O bond, in favor of stronger Si-O and C-Si bonds. The electronic activity of this center was not addressed at the time, but considering the coordination of the C, O and Si-ligand atoms, the complex is expected to be electrically inactive. Atomic hydrogen is an amphoteric impurity with negative-$U$ ordered donor and acceptor occupancy levels at $E_c - 0.18\,eV$ and $\sim E_c - 0.65$ eV [9–12], respectively. It is a bistable impurity – in the positive charge state it is most stable on the site of highest electron density, i.e. at the bond-center site ($H^+_{BC}$), while in the negative charge state it avoids high electron density regions due to Coulomb repulsion, preferring to be located at the tetrahedral interstitial site ($H^-_T$) [4]. The neutral defect is more stable at the BC site, meaning that the donor level involves essentially a direct transition between bond-centered states, hereafter referred to as a $H_{BC}(0/+)$ transition, where the final state includes a free electron in the conduction band. On the other hand, the acceptor is the energy difference between $H^-_T$ and $H^0_{BC} + e^-$ , therefore involving a considerable lattice relaxation energy. This indirect transition is referred to as $H_{T/BC}(-/0)$. Atomic H is known to interact effectively with both carbon and oxygen impurities in Si. For the case of carbon, theory and (Laplace) deep-level transient spectroscopy (DLTS) studies agree that the most stable form of a CH complex is the one in which the H sits between the C atom and its Si first neighbor [13]. Unlike isolated bond-centered H, it was reported that the C-H-Si defect (labelled $CH_{II}$) shows a positive-$U$ ordering of its donor and acceptor states at $E_v + 0.33\,eV$ and $E_c - 0.16\,eV$, respectively [13]. An additional donor level at $E_c - 0.22\,eV$ (labeled $CH_I$) was connected to a metastable precursor of $CH_{II}$, and was suggested to consist on a Si-H-Si unit neighboring the $C_s$ atom [13]. In a recent report by Stübner and co-workers [14], from the analysis of DLTS, field-induced change of emission-rates, annealing and depth-profile data, it was confirmed that the $E_c - 0.16\,eV$ level ($CH_{II}$ in Ref. 13 , but now referred to as $CH_A$) is an acceptor. However, they could not find any sign of $CH_I$. Instead, a shallower donor transition at $E_c - 0.14\,eV$ (labelled $CH_B$) was assigned to a $CH_n$ complex involving $n > 1$ hydrogen atoms [14]. With regards to the interaction of atomic H with $O_i$, we know from DLTS that the electrical levels

of OH are close to those of isolated H. Accordingly, donor and acceptor occupancy transitions at $E_c - 0.17\,\text{eV}$ eV and $E_c - 0.68\,\text{eV}$ were assigned to OH in Si [11, 12]. Although first-principles modeling predicts that hydrogen enhances oxygen diffusivity and that it does not bind directly to O [15–17], calculations of the electronic structure and electronic levels of OH in Si have not been reported so far. We have recently reported the formation of powerful recombination centers in n-type silicon as a result of the reaction between hydrogen, carbon and oxygen species [1]. Accordingly, hole traps $H_1$ and $H_2$ at 0.38 eV and 0.36 eV above $E_v$, respectively, were detected in Cz-Si subject to wet etching, remote plasma exposure and silicon nitride deposition, and they were assigned to COH complexes. We also demonstrated that the concentration of these COH defects is high enough to have a substantial impact on the minority carrier lifetime of Si-based solar cells. Below we report on our latest results on the search for the atomistic and electronic details of the COH-related recombination center in Si by combining first-principles calculations with DLTS and LVM infrared absorption measurements. The next section starts with a description of the methods employed, which is followed by a summary of the key observations related to the complex. We then report on the interaction of atomic H with C and O. These results are particularly instructive. They provide us with the fundamental physical-chemical guidelines behind the model that explains the formation and properties of COH. Among the calculated observables we report binding energies, vibrational mode frequencies and electronic transitions.

## 6.2 Methods

### 6.2.1 Experimental Details

For this work we selected a range of Cz and continuous Cz (CCz) n-type silicon slices with oxygen concentrations in the range $12 < [O_i] < 20$ ppma (1 ppma $= 5 \times 10^{16}\text{cm}^{-3}$) and substitutional carbon concentration of $0.01 < [C_s] < 9$ ppma. In addition, as reference we included silicon grown by the float zone (FZ) method which had $[O_i]$ and $[C_s] < 0.2$ ppma. All the material was phosphorus doped with resistivities in the range 1 to 8 $\Omega \cdot$ cm. The samples were hydrogenated in three different ways. Hydrogen was introduced into the samples, firstly, by wet etching with $HF/HNO_3$ solutions, secondly, by immersion in a 50 W remote H plasma for 30 minutes at temperatures between 25 and 250 °C, and, finally, in a way intended to simulate hydrogenation in a typical solar cell manufacturing process by in-diffusion of hydrogen from a H-rich silicon nitride film. Schottky diodes and Ohmic contacts were fabricated on the samples prior to capacitance-voltage and DLTS measurements. Minority carrier transient spectroscopy (MCTS) [18] using a 940 nm light emitting diode for optical excitation from the back of the slice was used to determine the electronic properties of hole traps including directly measured capture cross sections used to calculate the contribution of carrier recombination at the traps to the minority carrier lifetime. Local mode optical absorption measurements were undertaken at 30 K in the wavenumber range 500-1500 $\text{cm}^{-1}$ in order to observe the vibrational modes of $CO_n$ complexes in the samples. Minority carrier lifetime measurements were made using a Semilab WT-2000 PVN µ-PCD machine and iodine/ethanol surface passivation of the wafers.

### 6.2.2 Theoretical Details

First-principles density functional calculations were carried out using the VASP package [19], which uses the projector-augment wave (PAW) method [20] to deal with core-electrons and

plane-waves with a maximum kinetic energy $E_{\mathrm{cut}} = 370\,\mathrm{eV}$ for the valence. Exchange-correlation interactions were dealt within the generalized gradient approximation [21], and the electron density (potential) was assumed to be converged when the energy change between two consecutive self-consistent steps was less than 1 $\mu$eV. Substitutional C, interstitial O and interstitial H impurities were inserted into pristine 216-Si-atom supercells with cubic shape, optimized lattice constant $a = 5.4687\,\text{Å}$, and respective Brillouin zones sampled over a 2×2×2 grid of special k-points. All defect structures were optimized using a quasi-Newton algorithm, until the forces acting on the atoms were converged within 0.01 eV/Å. Electronic transitions were evaluated using the marker method [22]. Experimental levels from isolated interstitial H and from the vacancy-oxygen-hydrogen complex (VOH), were used as markers. When compared to bulk markers, these choices increase the accuracy of the calculated levels (often by about 0.1 eV) of complexes that incorporate bond-centered/tetrahedral H or a Si broken bond, respectively. The levels considered were $\mathrm{H_{BC}}(0/+) = \mathrm{E_c} - 0.175\,\mathrm{eV}$, $\mathrm{H_{T/BC}}(-/0) = E_c{-}0.5\,\mathrm{eV}$, $\mathrm{VOH}(0/+) = E_v + 0.27\,\mathrm{eV}$ and $\mathrm{VOH}(-/0) = E_c + 0.32\,\mathrm{eV}$ [9–12, 23].

LVM frequencies were obtained through diagonalization of a dynamical matrix composed of Hessian sub-matrices with respect to the displacement of impurity atoms plus their Si ligands. Hessian matrix elements were obtained numerically with explicit atomic displacements of 0.015 Å along all symmetry-independent directions.

## 6.3 Experimental Data

In MCTS and DLTS spectra of the hydrogenated oxygen and carbon rich Si samples, four electron and four hole emission peaks were detected. In the DLTS spectrum shown in Fig. 6.3.1, the peak labelled as $E_4$ is associated with the so-called thermal double donors originating from oxygen complexes [24], whereas the peaks E1 to E3 are related to hydrogen complexes [25, 26]. The $E_1$-$E_4$ traps are not significant in terms of lifetime degradation and will not be further considered in this work. The MCTS spectrum and the L-MCTS spectrum, presented as an inset in the same figure, show hole emission related signals $H_1$ to $H_4$. We have found that the dominant $H_1/H_2$ signals are dependent of carbon, oxygen and hydrogen content.

Firstly, we have compared the DLTS and MCTS spectra of a FZ sample with almost negligible $[O_i]$ and $[C_s]$ with the spectra for Cz and CCz samples after hydrogenation. In the FZ hydrogenated samples the $H_1$ and $H_2$ signals were not detected [27], while for the Cz and CCz samples the signals showed a proportional increase with $O_i$ and $C_s$ content in the crystals. Secondly, the concentration depth profiles of the $H_1$ and $H_2$ traps are found to be similar to that for the phosphorus-hydrogen complex formed in the hydrogenated samples. This provides an evidence of the involvement of a single hydrogen atom into the defects, which give rise to the $H_1$ and $H_2$ traps. Finally, a good correlation has been found between the intensity of the LVM band with its maximum at $1104\,\mathrm{cm^{-1}}$ observed in the infrared absorption spectra of carbon and oxygen rich samples subjected to different heat-treatments in the temperature range 550-700 °C and magnitudes of the MCTS signals due to the $H_1/H_2$ traps in similarly heat-treated neighboring samples, which were hydrogenated and prepared for MCTS measurements [1]. The band at $1104\,\mathrm{cm^{-1}}$ is related to an LVM of the CO complex [6, 7]. The results mentioned above give solid evidence of the carbon-oxygen-hydrogen composition of the complexes responsible for the $H_1/H_2$ traps.

With L-MCTS we have carried out direct measurements of electron and hole capture cross-sections and hole emission rates of the $H_1$ and $H_2$ traps. The details of the measurement technique can be found in Ref. 27. Capture cross-section measurements of minority and

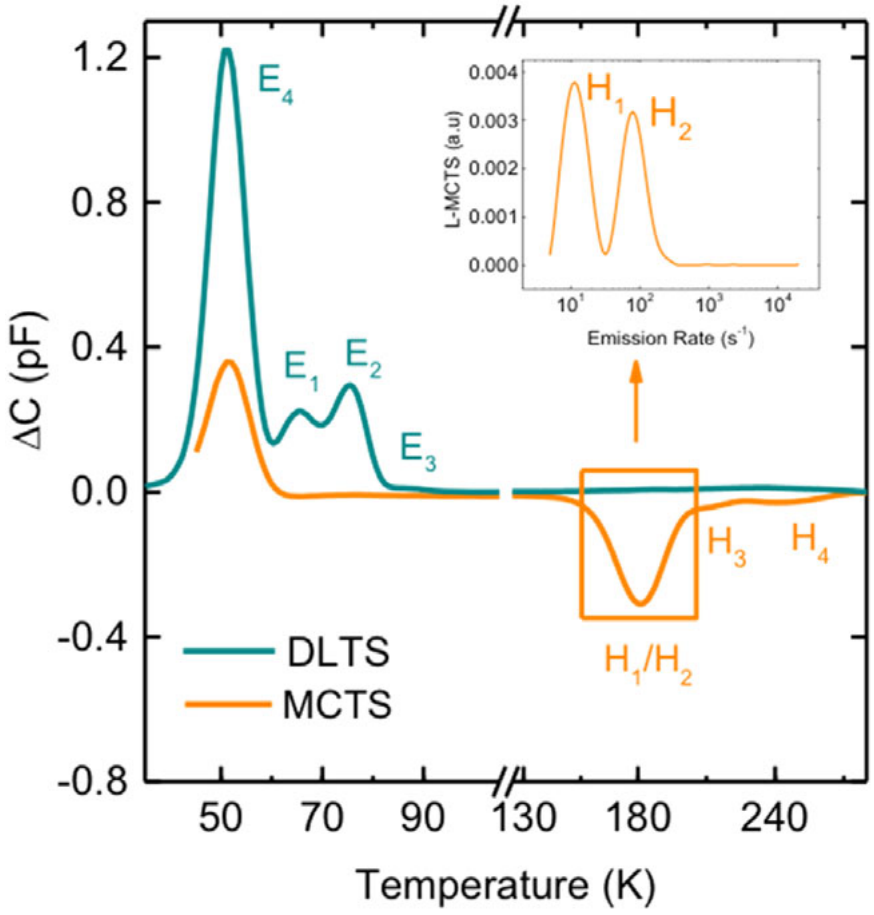


Figure 6.3.1: DLTS and MCTS spectra recorded on a sample from an n-type Cz-Si wafer, which was etched in $1HF/7HNO_3$solution for 2.5 min. We used $e_e = 50s^{-1}$, $U_b = -2V$, and $t_p = 10ms$ in all measurements and 940 nm LED pulses for the MCTS. The insert shows the separation of the $H_1$ and $H_2$ emission signals in the Laplace MCTS spectrum recorded at 190 K.

majority carriers resulted respectively in values of $9.8 \times 10^{-16}\,cm^2$ and $2.0 \times 10^{-17}\,cm^2$ for $H_1$, and of $7.9 \times 10^{-16}\,cm^2$ and $1.95 \times 10^{-17}\,cm^2$ for $H_2$. The defect levels obtained from the Arrhenius plots of $T^2$-corrected hole emission rates correspond to 0.38 ± 0.01 eV and 0.36 ± 0.01 eV from the valence band for the $H_1$ and $H_2$ centers, respectively. These characteristics indicate that the defects have an acceptor-like behavior and likely to be powerful recombination centers in n-type material. Furthermore, it has been found that the $H_1/H_2$ traps anneal out in the temperature range from 150 to 200 °C and their elimination resulted in significant improvement of lifetime in silicon wafers (see Refs. 1 and 27).

## 6.4 Theoretical results

### 6.4.1 Carbon-Hydrogen Interactions

Figure 2(a) shows a substitutional carbon atom in Si with several Si ligands. It also shows some sites (black dots) among many at which we placed a hydrogen atom to investigate the relative stability of CH complexes. In agreement with Andersen et al. [13], we found that for all charge states investigated (−, 0, and +), H prefers to connect directly to the carbon atom,

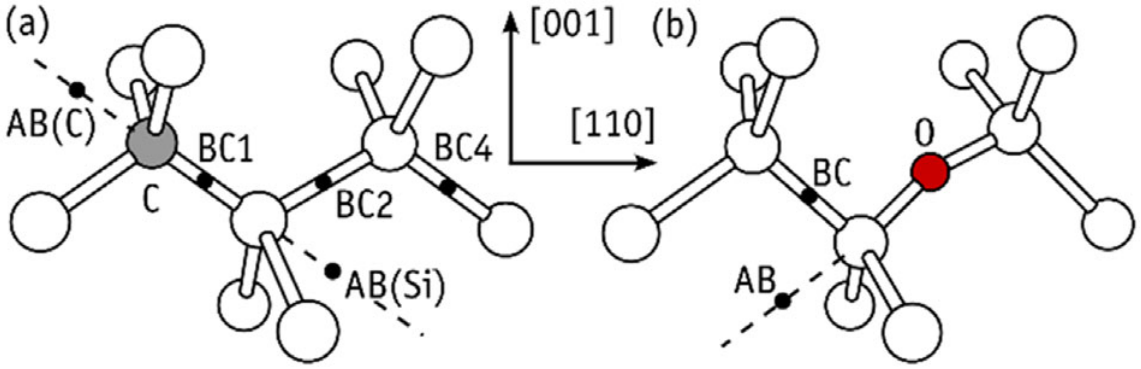


Figure 6.4.1: Low-energy sites (black dots), for hydrogen next to (a) substitutional carbon and (b) interstitial oxygen impurities. These diagrams are only schematic, representing approximate structures of defects obtained after atomic relaxation. C, O, and Si are represented in gray, red, and white, respectively.

close to site BC1. Other low-energy structures are BC2 and AB(C). In the neutral charge state, their energies are 0.51 and 0.64 eV above the BC1 ground state. The formation of a short C-H bond is an important stabilization factor for $CH_{BC1}$, in spite of the fact that it also leaves an unsaturated radical on the nearest Si atom. This dangling bond creates a semi-occupied one-electron state deep in the gap, making VOH an excellent marker to calculate its electronic levels. Comparing ionization energies and electron affinities of $CH_{BC1}$ with the same quantities from VOH we obtain donor and acceptor levels for $CH_{BC1}$ at $E_v + 0.28\,\text{eV}$ and $E_c - 0.17\,\text{eV}$, respectively, only $\sim 0.05\,\text{eV}$ away from the transitions observed at $E_v + 0.33\,\text{eV}$ and $E_c - 0.17\,\text{eV}$ (labeled $CH_{II}$) [13, 14].

Also in line with Ref. 13, we found that in the positive and negative charge states the BC2 and AB(C) structures are metastable by only 0.30 and 0.23 eV, respectively. The former configuration comprises a Si-$H^+_{BC}$-Si unit next to $C_s$, and therefore it is expected to show donor activity in close resemblance to that of isolated H in Si. Here, isolated $H_{BC}$ should be a good marker. Accordingly, we obtain a $CH_{BC2}(0/+)$ transition at $E_c - 0.24\,\text{eV}$, about 0.02 eV deeper than the measured additional CH-related donor reported in Ref. 13 and labeled $CH_I$. It is relevant to note that the calculated $CH_{BC2}(0/+)$ location is deeper than $CH_{BC1}(-/0)$ and also deeper than isolated $H_{BC}(0/+)$. This is in excellent agreement with the relative locations of the $CH_I$, $CH_{II}$ and E3′ DLTS signals [10, 12, 13]. We also found that $CH_{BC4}(0/+)$ (where H sits at the fourth neighboring BC-site to the C atom) has a donor level at 0.22 eV below $E_c$, i.e. closer but still deeper than $H_{BC}(0/+)$ and also still below $CH_{BC1}(-/0)$.

Following the suggestion of Ref. 14, that a $CH_n$ complex (with $n > 1$) could be responsible for a donor level at $E_c - 0.14\,\text{eV}$ (labeled $CH_B$), we actually investigated that possibility for $n = 2$. We found that $CH_2$ can adopt two nearly degenerate configurations (within 30 meV) similar to that $H_2^*$ of in Si, forming C-$H_{BC1}\cdots$Si-$H_{AB(Si)}$ and $H_{AB(C)}$-C$\cdots H_{BC1}$-Si trigonal structures. The configuration with both H atoms bound to the C atom is metastable by 0.6-1 eV (depending on the charge state). We also found that the two lowest-energy structures are electrically inert, and therefore, should the $E_c - 0.14\,\text{eV}$ level belong to a $CH_n$ complex, our results indicate that $n > 2$, most likely with one H atom located on a Si-Si bond.

### 6.4.2 Oxygen-Hydrogen Interactions

Among the oxygen-hydrogen complexes investigated, those obtained after placing H next to interstitial O, as depicted in Fig. 6.4.1(b), had the lowest energy. While $OH_{BC}$ is the

ground state in the positive charge state, $OH_{AB}$ was the most stable configuration in the negative charge state. The neutral defect is more stable with H at the BC-site (with $OH^0_{AB}$ being metastable by 0.23 eV only). We note that the H atom in $OH_{BC}$ adopts a puckered configuration, making a Si-H-Si angle of 136° after structural relaxation. This means that some of the compressive strain, which is present in isolated Si-$H^+_{BC}$-Si and Si-O-Si defects along their 111 bond directions, is released in $OH^+_{BC}$ and that corresponds to a calculated binding energy of 0.30 eV. The binding energy of atomic $H^-$ to interstitial O (with $OH^-_{AB}$ as a reaction product) is estimated as 0.47 eV after considering independent supercells with $H^-_T$ and $O_i$ defects. Here, the negatively charged hydride ion establishes an ionic bond with the oxidized (positively charged) silicon atom that is connected to oxygen. The above figures match the experimentally determined binding energies of 0.29 eV and $\sim 0.5\,$eV which give rise to the E3" [11] and AT" ($\sim 0.5\,$eV) [12], assigned to oxygen perturbed $(0/+)$ and $(-/0)$ transitions of bond-centered and tetrahedral hydrogen, respectively. Further confirmation of the above model comes from the calculated electrical levels. In this case, isolated atomic H is expected to do a good job as marker. Accordingly, we place $OH_{BC}(0/+)$ and $OH_{AB/BC}(-/0)$ transitions at $E_c - 0.16\,$eV and $E_c - 0.69\,$eV , respectively, in excellent agreement with the measured E3" and AT" signals with levels at $E_c - 0.17\,$eV and $E_c - 0.68\,$eV , respectively.

### 6.4.3 Carbon-Oxygen-Hydrogen Complex

In line with Ref. 8, we found that in the ground state of the CO complex, the O atom is located at the BC2-site with respect to carbon (see Fig. 6.4.1(a)). $COH_{BC1}$ and $COH_{BC4}$ configurations were metastable by 1.23 eV and 0.15 eV, respectively. The binding energy of $COH_{BC2}$ (against formation of uncorrelated substitutional carbon and interstitial oxygen impurities) was found to be 0.51 eV. Inspection of the band structure revealed a clean band gap and no electrical levels were found.

The CO complex gives rise to three C-related LVM absorption bands at 589, 640 and 690 $cm^{-1}$, respectively 18 $cm^{-1}$ below and 33 and 83 $cm^{-1}$ above the unperturbed Cs-related triplet mode at 607 $cm^{-1}$. It also produces an O-related band at 1104 $cm^{-1}$, 32 $cm^{-1}$ below the prominent 1136 $cm^{-1}$ band from interstitial O [6, 7]. LVM frequency calculations for the $COH_{BC2}$ model give C-modes at 557, 608 and 663 $cm^{-1}$ plus one O-mode at 1074 $cm^{-1}$. The C-modes are 18 $cm^{-1}$, below and 34, and 88 $cm^{-1}$, above the calculated 575 $cm^{-1}$, mode of isolated carbon. Analogously, we find the calculated O-mode frequency at 20 $cm^{-1}$,, below that of isolated O (calculated at 1094 $cm^{-1}$,). These figures improve previous modeling results [8], account very well for the observations, and provide indisputable evidence for the correctness of the atomistic model.

For the interaction of H with CO, we found several low-energy configurations, which differ on the defect charge state. For a negatively charged COH (which should be stable under equilibrium in n-type material) we found that the structure shown in Fig. 6.4.2(a) and labeled $COH_{AB}$, is distinctly stable. Analogously to $OH^-_{AB}$ , the $H^-$ anion is attached to the electron-depleted Si atom, which in this case is further oxidized due to the bond with an electronegative C atom.

For the neutral defect, we found the $COH_{BC1}$ configuration shown in Fig. 3(b) to be the ground state. $COH^0_{AB}$ is now metastable by 0.18 eV. The BC1 structure is made of a $CH_{BC1}$ defect perturbed by a nearby interstitial O atom, so it is expected to show rather similar electronic properties to $CH_{BC1}$. Another low energy configuration was $COH^0_{BC2}$ (0.05 eV above the ground state), which is depicted in Fig. 3(c).

Finally, for positively charged COH, the ground state configuration is now $COH_{BC2}$ (Fig. 3(c)), which resembles an $OH^+_{BC}$ complex stabilized by a nearby tensile $C_s$ defect. Another stable

Table 6.1: Calculated (calc) and experimental (exp) electronic levels of the defects investigated in this work. All values are given in eV.

| electronic level | calc. | exp. |
|---|---|---|
| $E_c$−$CH_{BC1}(-/0)$ | 0.17 | 0.16[13] |
| $CH_{BC1}(0/+) - E_v$ | 0.28 | 0.33[13] |
| $E_c - CH_{BC2}(0/+)$ | 0.24 | 0.22[13] |
| $E_c - OH_{AB/BC}(-/0)$ | 0.69 | 0.68[12] |
| $E_c - OH_{BC}(0/+)$ | 0.16 | 0.17[11] |
| $E_c - COH_{AB}(-/0)$ | 0.80 | |
| $E_c - COH_{AB/BC1}(-/0)$ | 0.81 | |
| $E_c - COH_{AB/BC2}(-/0)$ | 0.76 | |

structure is $COH^{+}_{BC1}$ (0.08 eV above the BC2 ground state).

Now we proceed to the calculation of the electrical levels of COH. Here we will focus on the acceptor activity only. Accordingly, the relevant acceptor transitions are $COH_{AB}(-/0)$, $COH_{AB/BC1}(-/0)$ and $COH_{AB/BC2}(-/0)$. While the last two involve electronic states similar to that of the $H_{T/BC}(-/0)$ marker, the $COH_{AB}(-/0)$ direct transition finds no resemblance with either $H_{T/BC}(-/0)$ or $VOH(-/0)$. Conversely, the $COH_{AB}(-/0)$ transition (observed at $E_c - 0.79\,eV$ [12]) should closely describe the $COH_{AB}(-/0)$level. Hence, we obtain indirect $COH_{AB/BC1}(-/0)$ and $COH_{AB/BC2}(-/0)$ levels at $E_c - 0.81\,eV$ and $E_c - 0.76\,eV$, respectively, i.e., $E_v + 0.31\,eV$ and $E_v + 0.36\,eV$ if we consider 1.12 eV for the band gap of Si. We also find a direct $COH_{AB}(-/0)$ at $E_c - 0.80\,eV$. Although all three calculated levels agree very well with the location of the $H_1/H_2$ hole traps, we note that we have two rather different mechanisms that could explain the recombination activity. These are (1) a direct $COH_{AB}(-/0)$ transition, or (2) a mechanism involving indirect $COH_{AB/BC1}(-/0)$ and $COH_{AB/BC2}(-/0)$ levels which imply a structural change in the neutral charge state. A deeper understanding of the above processes will involve the calculation of the potential energy surface between the AB, BC1 and BC2 configurations. We leave this for a future report to be published elsewhere. The structural distinction between the $H_1$ and $H_2$ traps is also an open question. Until now, we have considered the interactions between single C, O and H species. It is possible that one of these traps involves two O or H atoms, and we intend to look at this problem in the near future.

### 6.4.4 Conclusions

We presented a joint theoretical and experimental study of the interaction of H with carbon- and oxygen-related defects in silicon. For convenience we summarize all calculated levels and experimental assignments in Tab. 1.

We started by reporting on the interaction of H with a $C_s$ impurity, where based on the total energies and calculated levels, we confirm the support from first-principles theory to the assignment of $CH_{II}$ and $CH_I$ DLTS signals in Ref. 13 to carbon-hydrogen defects with the H atom on the first- and second-neighboring BC sites with respect to a $C_s$ impurity, respectively. We did not find any CH defect with two or less H atoms, which could give rise to a donor transition above $H_{BC}(0/+)$. This suggests that the CHB level at Ec—0.14 eV reported in Ref. 14could be related to a $CH_n$ complex involving $n > 2$ hydrogen atoms. The calculations support the interpretation of earlier experimental work [12] according to which H can bind to interstitial oxygen to from either $OH^+$ or $OH^-$ with negative-U ordering of the donor and acceptor levels. We found that for the positive charge state H is nearly bond-

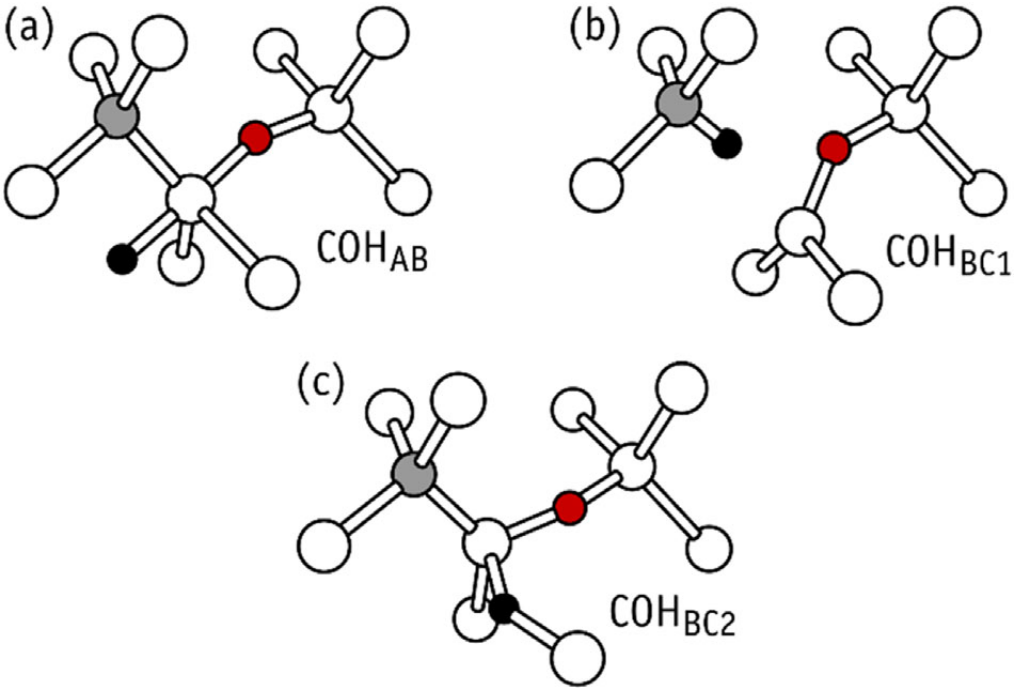


Figure 6.4.2: Ground state structures for COH in the negative (a), neutral (b), and positive (c) charge states. Si, C, O, and H atoms are shown in white.

centered forming a Si-$H^{+}_{BC}$-Si-$O_i$-Si zig-zag chain (like the O-dimer in Si), while the negative defect adopts an anti-bonding configuration that results in a nearly trigonal $H^{+}_{BC}$-Si-$O_i$-Si linear defect. The calculated binding energies and electrical levels are in excellent agreement with the observations. We finally investigated the CO complex and its interaction with H. We confirm that C and O atoms in CO are bound to a common Si atom – no direct C-O bond is established. The calculated local vibrational mode frequencies for this complex account very well for all four bands observed by infra-red absorption measurements.

The COH complex is predicted to adopt different configurations in all three charge states that were investigated (−, 0 and +). In the negative charge state, and particularly in n-type material, the complex takes the form of an $OH^{-}_{AB}$ defect perturbed by a nearby $C_s$ impurity, being therefore referred to as $COH^{-}_{AB}$. We suggest that this structure, shown in Fig. 6.4.2(a), corresponds to the observed hole-trapping center reported in Section 3. The neutral charge state was found to have several virtually degenerate configurations with the H atom either connected to the C atom, or at a nearby BC site (see Figs. 3(b) and 3(c)). Several calculated electrical levels are close to the observed $H_1/H_2$ traps, although further work is needed in order to understand eventual defect transformations upon carrier trapping/emission events.

## Acknowledgements

This work was supported by the FCT under projects PTDC/CTM-ENE/1973/2012 and UID/CTM/50025/2013, funded by FEDER funds through the COMPETE 2020 Program. Computer resources were partially provided by the Swedish National Infrastructure for Computing (SNIC) at PDC. In the UK this work was funded by EPSRC contract EP/M024911/1.

# Bibliography


[1] M. Vaqueiro-Contreras, V. P. Markevich, M. P. Halsall, A. R. Peaker, P. Santos, J. Coutinho, S. Öberg, L. I. Murin, R. Falster, J. Binns, E. V. Monakhov, and B. G. Svensson, physica status solidi (RRL) – Rapid Research Letters **11**, 1770342 (2017).

[2] R. Jones, R. Jones, and N. A. T. O. S. A. Division, *Early stages of oxygen precipitation in silicon*, NATO Asi Series. Partnership Sub-Series 3, High Technology, Vol. 17 (Kluwer Academic Pub, 1996).

[3] R. C. Newman and R. Jones, Current Opinion in Solid State and Materials Science **2**, 40 (1997).

[4] M. S. S. K. Estreicher and J. Weber, in *Silicon, Germanium, and Their Alloys: Growth, Defects, Impurities, and Nanocrystals (Hardback)*, edited by G. Kissinger and S. Pizzini (CRC Press, 2014) Chap. 7.

[5] F. Duerinckx and J. Szlufcik, Solar Energy Materials and Solar Cells **72**, 231 (2002), eMRS 2001 Symposium E: Crystalline Silicon for Solar Cells.

[6] R. Newman and J. Willis, Journal of Physics and Chemistry of Solids **26**, 373 (1965).

[7] A. Bean and R. Newman, Journal of Physics and Chemistry of Solids **33**, 255 (1972).

[8] C. Kaneta, T. Sasaki, and H. Katayama-Yoshida, Physical Review B **46**, 13179 (1992).

[9] B. Holm, K. Bonde Nielsen, and B. Bech Nielsen, Physical Review Letters **66**, 2360 (1991).

[10] N. M. Johnson, C. Herring, and C. G. Van de Walle, Physical Review Lett. **74**, 1889 (1995).

[11] K. Bonde Nielsen, B. B. Nielsen, J. Hansen, E. Andersen, and J. U. Andersen, Physical Review B **60**, 1716 (1999).

[12] K. B. Nielsen, L. Dobaczewski, S. Søgård, and B. B. Nielsen, Physical Review B **65**, 075205 (2002).

[13] O. Andersen, A. R. Peaker, L. Dobaczewski, K. B. Nielsen, B. Hourahine, R. Jones, P. R. Briddon, and S. Öberg, Physical Review B **66**, 235205 (2002).

[14] R. Stübner, V. Kolkovsky, and J. Weber, Journal of Applied Physics **118**, 055704 (2015).

[15] S. K. Estreicher, Physical Review B **41**, 9886 (1990).

[16] R. Jones, S. Öberg, and A. Umerski, in *Defects in Semiconductors 16*, Materials Science Forum, Vol. 83 (Trans Tech Publications, 1992) pp. 551–562.

[17] S. K. Estreicher, Y. K. Park, and P. A. Fedders, "Hydrogen - oxygen interactions in silicon," in *Early Stages of Oxygen Precipitation in Silicon*, edited by R. Jones (Springer Netherlands, Dordrecht, 1996) pp. 179–195.

[18] R. Brunwin, B. Hamilton, P. Jordan, and A. R. Peaker, Electronics Letters **15**, 349 (1979).

[19] G. Kresse and J. Furthmüller, Computational Materials Science **6**, 15 (1996).

[20] P. E. Blöchl, Physical Review B **50**, 17953 (1994).

[21] J. P. Perdew, K. Burke, and M. Ernzerhof, Physical Review Letters **77**, 3865 (1996).

[22] A. Resende, R. Jones, S. Öberg, and P. R. Briddon, Physical Review Lett. **82**, 2111 (1999).

[23] J. Coutinho, O. Andersen, L. Dobaczewski, K. Bonde Nielsen, A. R. Peaker, R. Jones, S. Öberg, and P. R. Briddon, Physical Review B **68**, 184106 (2003).

[24] L. C. Kimerling and J. L. Benton, Applied Physics Letters **39**, 410 (1981).

[25] M. Yoneta, Y. Kamiura, and F. Hashimoto, Journal of Applied Physics **70**, 1295 (1991).

[26] Y. Tokuda, I. Katoh, H. Ohshima, and T. Hattori, Semiconductor Science and Technology **9**, 1733 (1994).

[27] V. P. Markevich, M. V. Contreras, J. Mullins, M. Halsall, B. Hamilton, L. I. Murin, R. Falster, J. Binns, E. Good, J. Coutinho, J. Medford, C. L. Reynolds, and A. R. Peaker, in *2016 IEEE 43rd Photovoltaic Specialists Conference (PVSC)* (2016) pp. 0688–0693.

Chapter 7

# Summary of the results and conclusions

## 7.1 Summary of the results

In this section the results from the previous Chapters are compiled and summarized. A few unpublished results within the scope of the thesis are also provided in this section.

### 7.1.1 Early 3d and 4d transition metals and iron

In Chapter 3 we presented DFT and DFT+$U$ calculations concerning the electronic structure and migration barriers of interstitial 3d and 4d metallic impurities from the groups IV, V and VI. These results are summarized in Table 7.1. To these we append the results concerning iron interstitial and substitutional.

### 7.1.2 Interaction between transition metals and hydrogen

Chapter 4 presents a description of the interaction of titanium interstitial impurities with hydrogen in silicon bulk and its dependence with the doping of the material. In Chapter 5 the $Fe_iH$ and $Fe_sH$ were discussed. Concerning the interaction of vanadium interstitial with hydrogen, the trend is similar to the one of titanium, with the formation of vanadium-hydrogen bonds along the trigonal axis, in the opposite direction from the nearest silicon neighbor. There is also a diminishing of the electrical activity following the formation of vanadium-hydrogen bonds, with the disappearance of the vanadium acceptor level for any of the $V_iH_n, 1 \leq n \leq 3$ complexes, and removal of the double donor level for $V_iH_4$. However, unlike titanium, the addition of up to 4 hydrogen atoms does not lead to full passivation: the deep (0/+) transition is present in any of the considered vanadium-hydrogen complexes, and the addition of a fourth hydrogen atom leads to the appearance of a $(-/0)$ acceptor level at $E_c - 0.26$. Our calculated donor level $V_iH(0/+)$ at $E_v + 0.53$ is in good agreement with previous calculations [1], and is the most likely assignment for the donor-like level measured by Sadoh and co-workers at $E_v + 0.49$ [2]. We also obtained a single donor level for $V_iH_2$, $V_iH_3$ and $V_iH_4$ at $E_v$+0.77, $E_v$+0.63 and $E_v$+0.61 eV respectively. Concerning double donors we predict the following levels: $V_iH(+/++) = E_v + 0.46\,\text{eV}$, $V_iH_2(+/++) = E_v + 0.38\,\text{eV}$ and $V_iH_3(+/++) = E_v + 0.53\,\text{eV}$. In the case of chromium-hydrogen complexes we obtained the same trigonal structure for the $Cr_iH$ complexes. However, the second hydrogen atom can either bond to chromium, or to a neighboring silicon atom, depending on the charge state: in the neutral charge state, both hydrogen atoms will be located close to the chromium interstitial, similarly to what happens with $Ti_iH_2$ and $V_iH_2$. On the other hand, when the defect is positively charged, the second hydrogen atom can either bond to the Cr atom or one of the nearest Si neighbors. These two configurations are stable and nearly degenerate (energy difference below 0.01 eV). For complexes with a larger number of hydrogen atoms, the number of stable configurations increases. We predict a donor level $Cr_iH(0/+)$ at $E_v$+0.74 eV. The calculations for the vanadium-hydrogen and chromium-hydrogen complexes follow the same calculation parameters and method of Chapter 5. All the results concerning metal-hydrogen complexes are presented in Table 7.2

### 7.1.3 COH complexes

In Chapter 6, the interaction of hydrogen with carbon and oxygen was discussed. Several stable configurations for the COH complex were predicted. The main objective was to find a model that could explain the H1/H2 DLTS signals that correspond to two transition levels

Table 7.1: Ground-state configurations, calculated electrical levels and migration barriers of the transition metal impurities addressed in this thesis. The results presented were obtained with the use of the PBE functional. All values in eV

| Defect | Ground-state charge ($q$) and spin ($S$) configurations. | Electrical levels | Migration barriers ($q = 0/q = +1$) | Notes |
|---|---|---|---|---|
| Ti | $q = 0; S = 1$<br>$q = +1; S = 3/2$<br>$q = +2; S = 1$<br>$q = -1; S = 1/2$ | $E_c$−0.21 (−/0)<br>$E_v$+0.78(0/+)<br>$E_v$+0.17(+/++) | 1.98 / 1.94 | |
| V | $q = 0; S = 1/2$<br>$q = +1; S = 1$<br>$q = +2; S = 3/2$<br>$q = -1; S = 0$ | $E_c$−0.22 (−/0)<br>$E_v$+0.62 (0/+)<br>$E_v$+0.34 (+/++) | 1.30 / 1.41 | |
| Cr | $q = 0; S = 2$<br>$q = +1; S = 5/2$<br>$q = -1; S = 1/2$ | $E_c$−0.18 (−/0)<br>$E_v$+0.78 (0/+) | 0.77 / 0.74 | (−/0) level has no experimental assignment |
| Zr | $q = 0; S = 1$<br>$q = +1; S = 3/2$<br>$q = +2; S = 1$<br>$q = -1; S = 3/2$ | $E_c$−0.27 (−/0)<br>$E_v$+0.71 (0/+)<br>$E_v$+0.28 (+/++) | 2.29 / 2.30 | |
| Nb | $q = 0; S = 1/2$<br>$q = +1; S = 1$<br>$q = +2; S = 3/2$<br>$q = -1; S = 0$ | $E_c$−0.23 (−/0)<br>$E_v$+0.74 (0/+)<br>$E_v$+0.29 (+/++) | 2.52 / 2.23 | |
| Mo | $q = 0; S = 0$<br>$q = +1; S = 1/2$ | $E_v$+0.31 (0/+) | 2.31 / 2.01 | |
| $Fe_i$ | $q = 0; S = 1$<br>$q = +1; S = 3/2$ | $E_v$+0.39 (0/+) | | Calculted with Chapter 5 conditions |
| $Fe_s$ | $q = 0; S = 0$<br>$q = -1; S = 1/2$ | $E_v - 0.28$(−/0) | | Calculted with Chapter 5 conditions |

in the band gap at $E_v$+0.36 eV and $E_v$+0.31 eV, respectively. Our model is based on a hole-trap configuration, $COH_{ab}$, which corresponds to the lowest-energy structure for the negative charge state, with a direct $(-/0)$ transition at $E_v + 0.37$ eV. Upon capture of an hole, this configuration becomes unstable and the hydrogen atom swaps to one of the nearest bond-center sites, similarly to what happens to the OH defect, resulting in a new configuration such as $COH_{bc1}$ or $COH_{bc2}$. We predict two $(-/0)$ transition levels associated to the transformation of $\{COH_{ab}\}^-$ into $\{COH_{bc1}\}^0$ or $\{COH_{bc2}\}^0$ at $E_v + 0.36$ eV and $E_v + 0.41$ eV respectively. These two alternative paths for the reconfiguration of the COH defect upon capture of a hole are our best candidates to explain the aforementioned DLTS signals.

## 7.2 Discussion and concluding remarks

### 7.2.1 Conclusions

The first goal of the thesis was to perform a study of the electrical properties of early transition metal impurities in silicon by means of first principles electronic structure calculations. Our predictions concerning the magnetic moment of interstitial metallic impurities are in agreement with the models proposed in the 1960s by Ludwig and Woodbury [3, 4]: in most cases, the 3d and 4d orbitals are filled so as to maximize the magnetic moment of the defect. Our predictions of the electrical levels and migration barriers of the defects under scrutiny are in good agreement with the experimental observations (when available), validating our model and our choices of the approximations used.

Another goal of the thesis was to study the interaction between hydrogen and metallic impurities. The initial hydrogen reaction with a certain defect or impurity is predominantly driven by a Coulomb long-range interaction, causing the occurrence of that reaction to severely depend on the charge state of the defects involved in the reaction. As mentioned in Section 1.3, isolated atomic hydrogen should be found either in the positive or in the negative charge states, for intrinsic and $p$-type Si or $n$-type Si, respectively. Neutral hydrogen is metastable and should not be found in thermal equilibrium. The fact that hydrogen is positively charged in p-type Si explains why there are many reports of TM-H complexes in n-type Si, contrasting with the absence of reports in $p$-type. The interstitial TMs tend to be positively charged in $p$-type silicon and hence there will be Coulomb repulsion between the metal and the hydrogen. Under these conditions the metal-hydrogen complex will not form in equilibrium. Concerning the defect structure, titanium- and vanadium-hydrogen complexes form trigonal structures with the metallic ion remaining close to the tetrahedral site and hydrogen located near the hexagonal site along the $\langle 111 \rangle$ axis. When moving to the right side of the periodic table, to elements such as chromium or iron this pattern does not hold: in the case of $Cr_iH_2$ there is more than one stable configuration and in the cases of $Fe_iH$ and $Fe_iH_2$ the iron interstitial does not even remain at tetrahedral interstitial site. For the specific case of Ti, we predicted that further H attachment at equivalent sites can be energetically favorable, depending on the position of the Fermi level: the closer the position of the fermi level is to the bottom of the conduction band, the more hydrogen atoms can be attached to the impurity. In the particular case of iron we found that, in a hydrogen-rich environment, the formation of iron-substitutional type defects becomes likely in equilibrium, which could explain the mitigation of the levels related to iron interstitial.

In Chapter 6 we discussed the interaction of hydrogen with carbon-oxygen complexes. Carbon substitutional and Oxygen interstitial are common defects in silicon bulk material for solar applications and do not display any kind of recombination activity. There is also evidence [5] that carbon substitutional can trap oxygen interstitials to form CO complexes. These

Table 7.2: Calculated levels for metal-hydrogen complexes. The levels calculated for Ti-H complexes were calculated with the AIMPRO code, following the methodology presented in Chapter 4. The levels for the V-H and Fe-H complexes follow the methodology of Chapter 5, using the levels of the respective isolated metallic species as markers. All values in eV

| Defect | Electrical levels (eV) | Notes |
|---|---|---|
| $Ti_iH$ | $E_c$+0.13 (−/0) | |
| | $E_v$+0.69 (0/+) | |
| | $E_v$+0.30 (+/++) | |
| $Ti_iH_2$ | $E_c$−0.67 (0/+) | |
| | $E_v$+0.36 (+/++) | |
| $Ti_iH_3$ | $E_v$+0.77 (0/+) | |
| $Ti_iH_4$ | - | full passivation |
| $V_iH$ | $E_v$+0.53(0/+) | |
| | $E_v$ + 0.46 (+/++) | |
| $V_iH_2$ | $E_v$+0.77(0/+) | |
| | $E_v$ + 0.38 (+/++) | |
| $V_iH_3$ | $E_v$+0.63 (0/+) | |
| | $E_v$+0.53(+/++) | |
| $V_iH_4$ | $E_c$−0.26 (−/0) | |
| | $E_v$+0.61 (0/+) | |
| $Cr_iH$ | $E_v$+0.74 (0/+) | |
| $Fe_iH$ | $E_c$−0.22 (−/0) | |
| | $E_v$+0.50 (0/+) | |
| $Fe_iH_2$ | $E_c$−0.29 (−/0) | |
| | $E_v$+0.33 (0/+) | |
| $Fe_sH$ | $E_c$−0.50 (−/0) | |
| $Fe_sH_2$ | $E_c$−0.21 (−/0) | |
| | $E_c$−0.30 (=/−) | |

complexes are also electrically inert. However, from the interaction of hydrogen with these defects arises the formation of powerful recombination centers that are detrimental to the solar energy conversion efficiency. The COH complex is a strong recombination center that can work both as an electron and as a hole trap depending on its configuration.

In summary, the introduction of hydrogen in metal contaminated samples should be more effective at passivating TM-related defects in n-type or intrinsic material than in p-type material. While hydrogenation has been shown to be beneficial for the improvement of the performance of silicon-based solar cells, the use of gettering techniques for the treatment metallic impurities is still vital to the overall cell performance when UGM-Si based materials are applied.

### 7.2.2 Future Work

Following the thesis work, I have been revisiting the Light Induced Degradation (LID) problem in silicon, a problem that I worked on previously [6, 7] (publications 1. and 2. in the list of publications) and that is closely related to the issues reported in this thesis. This issue happens in p-$n^+$junction, Si based solar cells, which lose up to 10% efficiency, relative to its original value when illuminated. There are two stages of LID: fast (time scale of minutes) and slow (time scale of hours). This degradation should be due to a recombination center able to draw

in minority and majority carriers and recombine them. It is known that the appearance of the defect responsible for the slow LID depends linearly on boron concentration and quadratically on oxygen concentration: this indicates that the defect should be a $B_sO_{2i}$ complex. However, the process of how it becomes an active recombination center that can lead to LID is still under debate: the ground-state structure $B_sO_{2i}$ is a shallow acceptor just like boron, which, at first glance, should not be able to explain the recombination process associated to LID. Alternative defects such as $B_iO_{2i}$ have been ruled out [7]. Another particularity of this problem is its relatively large time scale, and how the transformation of a recombination-inactive $B_sO_{2i}$ into a recombination-active configuration can be compatible with it. Currently we are working on a model which we hope to be able to address these issues.

# Bibliography


[1] D. J. Backlund, T. M. Gibbons, and S. K. Estreicher, Physical Review B **94**, 195210 (2016).

[2] T. Sadoh, H. Nakashima, and T. Tsurushima, Journal of Applied Physics **72**, 520 (1992).

[3] H. H. Woodbury and G. W. Ludwig, Physical Review **117**, 102 (1960).

[4] G. W. Ludwig and H. H. Woodbury, Physical Review Lett. **5**, 98 (1960).

[5] Y. Shirakawa and H. Yamada-Kaneta, Journal of Applied Physics **80**, 4199 (1996).

[6] L. I. Murin, E. A. Tolkacheva, V. P. Markevich, A. R. Peaker, B. Hamilton, E. Monakhov, B. G. Svensson, J. L. Lindström, P. Santos, J. Coutinho, and A. Carvalho, Applied Physics Letters **98**, 182101 (2011).

[7] A. Carvalho, P. Santos, J. Coutinho, R. Jones, M. J. Rayson, and P. R. Briddon, physica status solidi (a) **209**, 1894.